UNIVERSITY OF
LIVERPOOL

Multimodal imaging to evaluate the distribution and fate of a mesenchymal stromal cell therapy

Thesis submitted in accordance with the requirements of the University of Liverpool for the degree of Doctor in Philosophy

By

Alejandra Hernandez Pichardo

October 2022

Declaration

This thesis is the outcome of work completed while enrolled as a Doctor of Philosophy candidate at the University of Liverpool. I confirm that no part of the work mentioned in this thesis has been submitted in support of an application for another degree or qualification at this or any other university or institute of learning. I, Alejandra Hernandez Pichardo, declare that the work in this thesis is all my own. Wherever appropriate, any contributions of colleagues who assisted in the study is indicated accordingly.

Candidate

Alejandra Hernandez Pichardo, October 2022

Supervisors

Professor Patricia Murray, Professor Raphaël Lévy, Professor Violaine Sée, Dr Bettina Wilm.

This research was carried out in the Department of Molecular Physiology and Cell Signalling, Institute of Systems, Molecular and Integrative Biology, University of Liverpool.

Contents

List of tables

List of figures

List of abbreviations

α-MEM: Minimum essential medium eagle – alpha modification

AKI: Acute kidney injury

BLI: Bioluminescence imaging

BP: Bandpass filter

BSA: Bovine Serum Albumin

CKD: Chronic kidney disease

CUBIC: Clear unobstructed brain/body Imaging cocktails and computational analysis

DAMPs: Damage associated molecular patterns

DAPI: 4′,6-diamidino-2-phenylin-dole

DBE: Dibenzyl ether

DC: Dendritic cell

DCM: Dicloromethane

s-DISCO: stabilized Three-dimensional imaging of solvent cleared organs.

DMEM: Dulbecco's modified eagle medium

EB: Evans Blue

ECi: Ethyl cinnamate

EMCCD: Electron multiplying charge coupled device

EVs: Extracellular vesicles

FBS: Fetal Bovine Serum

FLuc: Firefly Luciferase

GNPs: Gold nanoparticles

GNRs: Gold nanorods

GvHD: Graft-versus-host disease

HDAC2: Histone deacetylase 2

HEK: Human Embryonic Kidney

H-Mito: Human mitochondria

hUC-MSCs: human umbilical cord mesenchymal stromal cells

IBMIR: instant blood-mediated inflammatory reaction

IP: Intraperitoneal

IRI: Ischemia reperfusion injury

IV: Intravenous

LP: Long pass filter

mRNA: messenger ribonucleic acid

micro-CT: micro-computed tomography

miRNA: micro ribonucleic acid

MIP: Maximum intensity projection

MPI: Magnetic particle imaging

MPO: Myeloperoxidase

MRI: Magnetic resonance imaging

NETs: Neutrophil Extracellular traps

NK: Natural killer

OTC: Optical tissue clearing

PAI: Photoacoustic imaging

PAMPs: Pathogen associated molecular patterns

PEI: Polyethylenimine

PET: Positron emission tomography

PFA: Paraformaldehyde

SPECT: Single photon emission tomography

TBI: Traumatic brain injury

TEM: Transmission electron microscope

tdTomato: Tandem tomato

THF: Tetrahydrofuran

MSCs: Mesenchymal stromal cells

ZTE: zero-echo time

3D: Three dimensional

Supporting papers

Publications in the Appendix

1. **Hernandez Pichardo A.,** Littlewood J., Taylor A., *et al*. Computed Tomography lacks sensitivity to image gold-labelled MSCs as evidenced by Multispectral Optoacoustic Tomography. BioRXiv. 2022. https://doi.org/10.1101/2022.06.15.495483 (1).

2. **Hernandez Pichardo A.,** Amadeo F., Lévy R., *et al*. Comparison between optical tissue clearing methods for detecting administered mesenchymal stromal cells in mouse lungs. BioRXiv. 2022. https://doi.org/10.1101/2022.07.23.501233 (2).

3. **Hernandez Pichardo A.,** Wilm, B., Liptrott, N., Murray, P. Intravenous administration of human umbilical cord mesenchymal stromal cells leads to an inflammatory response in the lung. BioRXiv. 2022. https://doi.org/10.1101/2022.09.26.509547 (3).

Conference presentations

1. Hernandez Pichardo A, Levy R, Murray P, Wilm B, Taylor A. Optimizing conditions for Mesenchymal Stromal Cell (MSC) tracking in mouse models of kidney disease (2020, June). Poster presentation at HLS Faculty Poster Day, online, Liverpool, UK.

2. Hernandez Pichardo A, Lévy R, Sée, V, Wilm B, Ressel L, Murray P. Imaging modalities to evaluate safety and distribution of cell therapies (2021, November). Oral pitch and poster presentation at Stem Cell Community Day. Cologne, Germany.

3. Hernandez Pichardo A, Lévy R, Sée, V, Wilm B, Ressel L, Murray P. Bioluminescence and optical tissue clearing to evaluate distribution and safety of administered cells. (2022, March). Poster presentation at the European Molecular Imaging Meeting. Thessaloniki, Greece.

4. Hernandez Pichardo A, Lévy R, Sée, V, Wilm B, Taylor, A, Ressel L, Murray P. Multi-modal imaging to evaluate distribution and fate of administered cells (2022, April). Oral presentation at RenalToolBox International Conference. Liverpool, UK.

Acknowledgements

input and collaborations throughout my studies. Also, thanks to all the colleagues who lend a hand in the lab.

Finally, I am most appreciative to my friends and family. Dr Ana and Soham, your friendship made all the difference in the day to day. Steffi and Fabi, I could not have asked for better friends. Thanks for being my support system. Marcel, I could not have done this without you. Thank you for being the best and giving me something to look forward to. Mamá, papá, tía Susana, Jessy, there are no words to describe how grateful I am of everything you have done for me. Thank you for being my greatest supporters and for always believing in me.

Abstract

Mesenchymal stromal cell (MSC) treatments have shown beneficial outcomes in preclinical models of various diseases but limited therapeutic effects in clinical trials. This disparity in translation reflects the need to understand the mechanisms involved in the host's response to therapy. Intravenous injection is the preferred delivery method in the clinics, but it has been observed that using this route leads to MSCs becoming entrapped in the lungs, making this organ an interesting study target.

In this thesis, different imaging modalities to study the distribution and fate of administered MSCs in the lung were used. The first aim was to combine the sensitivity of bioluminescence imaging (BLI) with the ability of micro-computed tomography (micro-CT) to image lung tissue to track the cells *in vivo.* Then, to study the biodistribution of the MSCs in the lung microenvironment at single cell resolution, an optical tissue clearing protocol was established. Finally, the effect of the MSCs on innate immune cells in the lung and their potential interactions were investigated.

Human umbilical cord MSCs (hUC-MSCs) that had been labelled with the genetic reporter Firefly luciferase (FLuc), the fluorescent reporter tandem Tomato (tdTomato), or with gold nanorods were used. The hUC-MSCs were injected into the tail vein of mice, which were then imaged *in vivo* using BLI and micro-CT. After MSC injection, animals were culled, and the lungs collected and processed for confocal microscopy or flow cytometry.

BLI revealed that following intravenous injection, the MSCs localized to the lungs hampering the ability of MSOT to image the MSCs within this organ. Using micro-CT, it was not possible to detect the MSCs, indicating that this method might lack sensitivity to image gold-labelled cells. Next, the CUBIC, a modified stabilized DISCO (s-DISCO) and ethyl cinnamate (ECi) optical tissue clearing protocols were compared to find a suitable method for studying the biodistribution of hUC-MSCs and their interactions with the mouse lung microenvironment. CUBIC was the only method that enabled direct imaging of tdTomato-expressing hUC-MSCs as the other methods quenched the fluorescence of the reporter. Moreover, CUBIC in combination with

immunofluorescence allowed the interaction of the hUC-MSCs with cells in the host lung to be investigated. Particularly, it was observed that the hUC-MSCs appeared to be retained in the pulmonary microvasculature as they were not found in large blood vessels. Flow cytometric analysis showed that shortly after hUC-MSC IV injection, neutrophils, monocytes, and macrophages mobilized to the lung and participated in an inflammatory response. Twenty-four hours post cell infusion, the number of innate immune cells in the lungs decreased but a polarization toward an anti-inflammatory phenotype was observed. Moreover, immunofluorescent staining revealed that neutrophils were preferentially distributed in close vicinity to the hUC-MSCs, suggesting that their clearance within 24 h might involve efferocytosis.

In summary, using a range of *in vivo* and *ex vivo* imaging techniques, it was shown that following intravenous injection into mice, hUC-MSCs appeared to accumulate in the pulmonary vessels and mostly died within 24 h. Within 2 h following administration, the hUC-MSCs caused an inflammatory response in the lung, leading to an increase in neutrophils and pro-inflammatory macrophages. However, by 24 h, neutrophils were at basal levels and there was an increase in anti-inflammatory macrophages. Although there are numerous reports indicating that MSCs polarise macrophage towards an anti-inflammatory phenotype, an interesting finding of this study was that the initial effect of hUC-MSCs on host immune cells was actually pro-inflammatory. This may provide some insight into the potential therapeutic mechanisms of MSCs.

Chapter 1. Introduction

1.1   Mesenchymal Stromal cells

The 1970s saw the isolation of mesenchymal stromal cells (MSCs) from the bone marrow for the first time (4). These cells were defined as a subset of fibroblast-like cells that could generate fat cells, bone, cartilage and reticular cells *in vitro* (4). Since then, several studies have reported that MSCs can be isolated from the stromal fraction of a variety of additional tissues such as umbilical cord, tooth pulp, adipose tissue, synovial membrane, placenta and more (5–9).

Regardless of tissue of origin, the International Society for Cell Therapy established minimum criteria to characterize MSCs: plastic adherence, trilineage *in vitro* differentiation (adipogenic, osteogenic, chondrogenic), and expression of CD73, CD90, and CD105, as well as the lack of expression of the CD45, CD34, CD19, CD14, CD79a, CD11b, MHC II and HLA-DR surface markers (10).

MSCs vary greatly based on the tissue and donor from which they were derived (11,12). For example, varying degrees of *in vitro* multi-differentiation and proliferative capacities can be observed in single-cell derived clones of human bone marrow MSCs (13,14). Moreover, isolating them in large numbers is challenging, and long term culture affects their properties and makes them susceptible to malignant transformation (15).

Despite the above-mentioned limitations, there is a great deal of interest in using MSCs as therapies; which is related to their immunomodulatory effects and ability to promote tissue repair (16). Currently, according to ClinicalTrials.gov, over 5,500 MSC-based clinical trials are active or in recruitment world-wide. These span a broad range of clinical applications, including musculoskeletal, neurological, cardiovascular, gastroenterological, haematological, dermatological, pulmonary, renal, ophthalmological, gerontological, and psychiatric conditions (17,18).

Most clinical studies focus on safety and have generated promising results, demonstrating that MSC treatments are relatively safe (19). Fewer studies

address efficacy and the minority of these have been able to meet primary efficacy endpoints (20). Conversely, efficacy in preclinical studies has been thoroughly assessed (21) with beneficial effects reported in bone diseases and cartilage repair (22–24), neurodegeneration (25), heart conditions (26,27), liver regeneration (28), skin regeneration (29), kidney diseases (30–32) etc.

Several factors, such as variability in the potency of the MSC products, differential biodistribution and pharmacokinetics influenced by the administration route selected, and a limited understanding of the host's response to the MSCs, are likely to contribute to their unsatisfactory clinical outcomes (20). The discrepancy between preclinical and clinical data reflect the challenges of translating MSC therapies and highlight the need to better understand the mechanisms of action of MSCs as therapeutic agents.

1.2 Lung first-pass effect

The preferred delivery route for cell therapies in the clinics is intravenous. Several studies to date have shown that administering MSCs via this method leads to the cells becoming trapped in the lung's microvasculature (33–37), a phenomenon known as the first-pass effect (38). A possible reason for the MSCs becoming trapped is because their diameter is larger than that of the pulmonary capillaries (39). Moreover, the cell surface structure and adhesion molecules of MSCs influence their clearance rate in the lungs (40,41). MSCs culture and expansion increases the levels of integrins such as $\beta1$, $\alpha5$, and $\alpha V\beta3$ (42). These integrins can directly interact with lung endothelial cells, as they express integrin ligands such as fibronectin and vitronectin in their surface (42). Nevertheless, despite MSCs being entrapped in the lungs, efficacy of MSC therapies has been observed in several preclinical models of disease.

1.3 Immune system

The immune system is comprised of haematopoietic stem cell-derived cells (Figure 1) which function is to defend against infection and disease. The immune system's reaction to invasive pathogens and other foreign substances is known as the immune response and, depending on the specificity and speed of the reaction, it can be subdivided into innate and adaptive immunity (43).
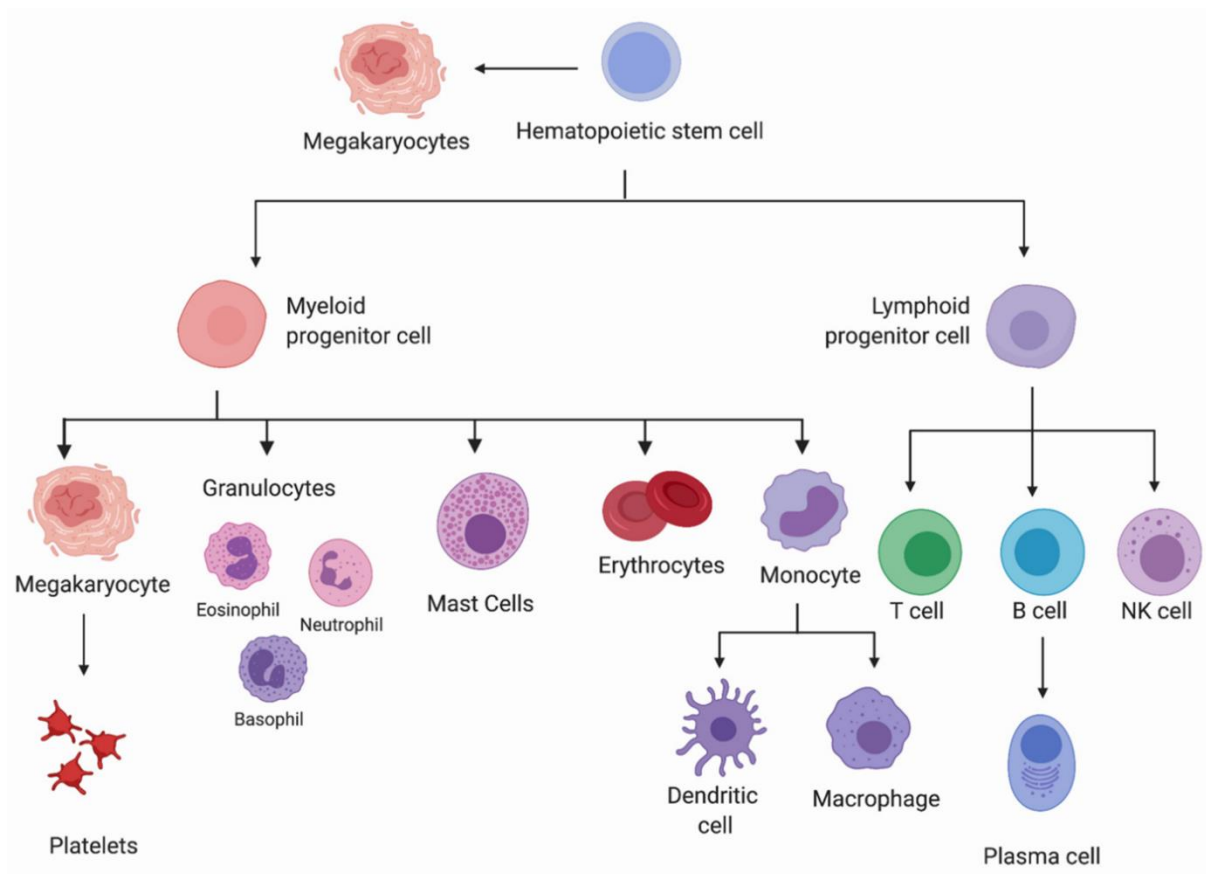
Figure 1. Haematopoiesis. Diagram showing the lineage development of different blood cells derived from a common myeloid progenitor or a common lymphoid progenitor. By Raza, Y, Salman, H, and Luberto, C. Cells 2021, 10(10), 2507.

1.4   Innate immunity

The innate immune system is the first line of defence against pathogens, and includes physical and chemical barriers, as well as cells and molecules. This system's main tasks are to rapidly prevent, control and eliminate infections, to repair damage, and to enhance the immune response by activating adaptive immunological responses (44).

Innate immune responses rely on the recognition of pathogen associated molecular patterns (PAMPs) shared by large groups of microorganisms (45). The cellular component of the innate immunity includes antigen presenting cells (APCs) such as granulocytes (neutrophils, basophils and eosinophils), and dendritic cells and macrophages, which are derived from monocytes (Figure 1). The aforementioned cells, which are derived from a myeloid

progenitor, are professional phagocytes that remove apoptotic cells and clear pathogens (46).

Macrophages can specialize based on their anatomical location. In the lung, alveolar macrophages constitute the main immune cell type (47). Alveolar macrophages are long-lived tissue resident macrophages that populate the lung during early embryogenesis. They play a crucial role in preserving lung homeostasis by removing particles, microorganisms and allergens from the lung's alveolar surfaces, without causing inflammation (48). In contrast, interstitial macrophages are short-lived cells that are recruited to the lung in response to injury and contribute to the inflammatory response (49). Moreover, the macrophage's phenotype varies depending on the tissue microenvironment. M1 or classically-activated macrophages are considered pro-inflammatory while M2 or alternatively-activated macrophages are anti-inflammatory (50).

1.5   Adaptive immunity

The adaptive immunity is characterised by a two-stage targeted response driven by antigen-specific receptors on T and B lymphocytes. First, APCs of the innate immune system present the antigen to specific T or B cells which leads to these cells becoming activated. Second, an effector response occurs as a result of the activated T cells migrating to the disease site, or activated B cells secreting antibodies into the blood and tissue fluids (43). Although the innate and adaptive immunity are closely related, the main advantage of the adaptive immunity is memory formation, which provides protection against recurrent infections (44).

1.6   MSCs mechanism of action

It was first thought that upon intravenous administration, MSCs migrated to injury sites, where they engrafted and differentiated into functional cells, leading to the regeneration of injured or diseased tissues (51). This hypothesis has been disproven and over the last decade, there has been a surge in studying the processes by which MSCs might be involved in the repair of damaged organs and tissues despite becoming entrapped in the lung and

dying rapidly following intravenous administration (51–53). The field has made significant progress in characterising numerous mechanisms by which administered MSCs can promote tissue regeneration that will be discussed below.

1.6.1 Paracrine effects

MSCs secrete multifunctional molecules such as cytokines, chemokines and growth factors, which are involved in regeneration and immune modulation. The MSC secretome and MSC-derived plasma membrane particles, through membrane fusion and internalization mediated via cell-surface receptors, act on the innate (54,55) as well as the adaptive immune system (52).

Innate responses include inhibition of natural killer (NK) cell proliferation and prevention of NK cytotoxic activity (56,57), augmented neutrophil viability and function as well as protection against apoptosis (58,59), suppression of dendritic cell (DC) maturation (60), prevention and decrease of monocyte pro-inflammatory polarization (54,61), contribution to macrophage anti-inflammatory polarization (62), and attenuation of the secretion of inflammatory factors by activated macrophages (63). Adaptive immune responses include reducing the activation, proliferation and differentiation of B- and T-cells (64–68).

An important consideration is that MSCs may exert variable immunomodulatory responses depending on the local microenvironment (53). For example, inflammation has been shown to alter the morphology and proliferation of adipose tissue-derived MSCs. Moreover, their immunosuppressive capacity was enhanced when exposed to proinflammatory cytokines (69). *In vivo*, the microenvironment might result in the MSCs having a detrimental impact on the disease state as shown by fibrotic worsening in a lung injury model (70). On the contrary, a different lung microenvironment might aid in stimulating the immunomodulatory benefits of the MSCs (71). These results show that MSCs switch their effects based on the disease status.

Additionally, the components of the MSC secretome have the potential to rescue injured cells, decrease tissue damage and enhance repair. These effects are mediated via trophic factors that can promote angiogenesis, reduce inflammation and fibrosis, and induce progenitor cell renewal (72–74). Although the mechanisms by which these paracrine processes promote cell survival and repair remain to be elucidated, the utility of MSCs and their released products has been demonstrated in a variety of disease models (75–77).

1.6.2 Extracellular vesicle transfer

Extracellular vesicles (EVs) are lipid bound vesicles released into the extracellular space by most types of cells (78). EVs contain lipids, nucleic acids, proteins, mRNAs, and miRNAs that mediate the therapeutic effects of MSCs by participating in cell-to-cell communication, as well as communication with the microenvironment (79).

The administration of EVs generated from various MSC sources has been shown to be beneficial in a variety of conditions such as lung (79), inflammatory (80), retinal (81), kidney (82), neural (83), and heart diseases (84), as well as cancer (85).

EVs interact with recipient cells through a variety of mechanisms such as endocytic internalization, fusion with plasma membranes, and plasma membrane receptors (86). Upon internalization, they exert therapeutic effects by the release of their cargo, which might inhibit or activate particular signalling pathways that trigger immunomodulatory responses, promote cell proliferation/survival, modulate differentiation, mediate cell communication, etc (79,87).

After EV administration, various studies have found an increase in cell proliferation and angiogenesis, and a decrease in apoptosis and inflammation (88,89). Moreover, a subset of mRNAs and miRNAs within the EVs may affect gene expression, resulting in regulation of biological activity and therapeutic effects (90). The miRNA profile of EVs derived from adipose, umbilical cord and bone marrow MSCs varies greatly (91), with little overlap between

sources. Adipose and bone marrow exosomes contain miR-486-5p and miR-10b-5p in high abundance, while no miRNA expressed by umbilical cord exosomes overlaps with the former sources (92).

Although the research on the effects of specific miRNAs on therapeutic outcomes remains scarce, it has been shown that EVs that include miR-21-5p promote microglial M2 polarisation and alleviate neuroinflammation after traumatic brain injury (TBI) (93). Moreover, miR-873a-5p decreased neuroinflammation after TBI by blocking the NF-κB signalling pathway (94).

These discoveries have shifted the field toward a cell-free approach to therapy, as EVs derived from MSCs display immunomodulatory and regenerative properties similar to the parent cells (95).

1.6.3 Mitochondrial transfer

Evidence suggests that the ability of MSCs to transfer their mitochondria to injured cells and modulate their cellular metabolism, can also help restore the biological fitness of the recipient cells (96). This phenomenon occurs in the context of injury and inflammation as a response to damage-associated molecular patterns and reactive oxygen species (97).

Mitochondrial donation from MSCs resulting in improved outcomes has been described in different *in vivo* disease models such as acute lung injury (98), spinal cord injury (99), asthma (100), neurotoxicity (101), and nephropathy (102,103). This evidence suggests that MSC mitochondrial transfer contributes to their therapeutic efficacy.

Transfer of mitochondria affects immune cell behaviour. Examples of this are macrophages that become more phagocytic by promoting an anti-inflammatory phenotype after receiving MSC mitochondria (104), and the improvement of T-cell immunosuppressive activity (105,106).

Different mitochondrial transfer mechanisms have been described. Tunnelling nanotubes (TNTs) are long-distance (<100 μm) cytoplasmic extensions that form cell-to-cell connections that facilitate the exchange of components, including mitochondria, between cells (107–110). In addition, cell fusion and gap junctions have also been shown to be involved in this process (111,112).

Finally EVs have also been shown to contain mitochondrial DNA and whole mitochondria in their cargos (113).

Mitochondrial transfer has been linked to a variety of physiological and pathological processes, as well as to the therapeutic effects of MSC therapies. When compared to mitochondrial biogenesis, replacement of damaged mitochondria through donation from MSCs is a quicker and physiologically more practical for the recipient cell (114). For instance, the symptoms of Parkinson's disease were improved by IV injection of exogenous mitochondria into a mouse model of this disease (115).

1.6.4 MSCs apoptosis and phagocytosis

Recognizing and clearing apoptotic cells by phagocytosis is an essential mechanism to preserve tissue homeostasis. Recently, MSC apoptosis and phagocytosis have been suggested as processes involved in MSC-mediated immunomodulation following IV administration (116–119).

Rapid caspase activation has been observed following IV MSC delivery and lung entrapment, indicating that infused MSCs undergo apoptosis shortly after delivery but retain their immunomodulatory potential (119). Importantly, MSCs resistant to apoptosis did not exert immunosuppressive effects in a murine model of asthma, indicating that apoptosis is necessary for the therapeutic effect of the MSCs in this setting (118).

Moreover, efferocytosis by monocytes and macrophages resulted in alterations in the polarization status, immunometabolism and function of these cells, impacting their effects (116–118,120). Neutrophils have been shown to be involved in the clearance of exogenously administered MSCs *in vivo* by means of phagocytosis (116). These findings imply that the immune system is directly involved in the clearance of infused MSCs and in mediating their effects.

1.6.5 Immunomodulation

MSCs are often referred to as "immune privileged" given that they do not express major histocompatibility complex (MHC) Class II, and express very low levels of MHC Class I (121). This statement is debatable given that MSCs have been reported to trigger the production of antibodies resulting in the rejection of allogeneic cells (18). Moreover, they interact with cells of the innate and adaptive immune system triggering immunomodulatory responses (122). As previously discussed, the fundamental mechanisms of these interactions are now being thoroughly investigated. Overall, the immunomodulation mediated by MSCs is a redundant system, in which the molecules involved (growth factors, chemokines, cytokines, membrane particles, EVs miRNAs) play inter-related roles (123). Thus, more research in this area is necessary to fully explore MSC-mediated therapeutic immunomodulation in clinical application and implementation.

1.7   MSCs labelling and tracking

Determining MSC fate after infusion is essential to advance cell therapies (124). This requires that cells are labelled to monitor them *in vivo* and *ex vivo*. The label is necessary to distinguish the administered cells from their tissue environment within the host. In some circumstances, for example when human stem cells or their derivatives are applied in rodent models, they can be identified *ex vivo* via immunohistochemistry for cell-endogenous markers, e.g. human-specific nuclear antigen (125). However, in many cases and especially when administered cells are to be tracked via *in vivo* imaging, a label needs to be introduced prior to administration. Such a label should allow easy identification of infused cells in host tissue without inducing morphological and physiological changes. The ideal label should be harmless to the cells, facilitate detection at high-resolution, be reliable and stable to avoid false positives, give a strong signal, permit repeated, longitudinal imaging and be introduced using minimally invasive protocols (126,127).

Chemical probes and nanoparticles, which are typically taken up by endocytosis, can provide an easy-to-apply and robust label for cell tracking via computed tomography (CT) and photoacoustic imaging (PAI), among other

imaging *in vivo* strategies. However, when used to label proliferating cells, they usually only allow short-term cell tracking as the label becomes diluted during cell divisions. Furthermore, the risk of false positive signals needs to be considered as probes can be taken up by endogenous host cells following death of the originally labelled and administered cells. Also, some probes, e.g. iron oxide nanoparticles and gold nanorods, can generate a signal after the labelled cell dies (128).

Labelling cells with genetically encoded reporters allows for *in vivo* monitoring and longitudinal tracking of viable cells after infusion in animal models (129). Suitable reporter genes are available for imaging modalities such as bioluminescence (BLI) (Firefly luciferase, *Renilla* luciferase, NanoLuc®) (130), and fluorescence imaging (iRFP, tdTomato, etc.). One consideration is that reporter genes might become silenced upon stem cell differentiation.

1.7.1 *In vivo* cell tracking

1.7.1.1 Bioluminescence
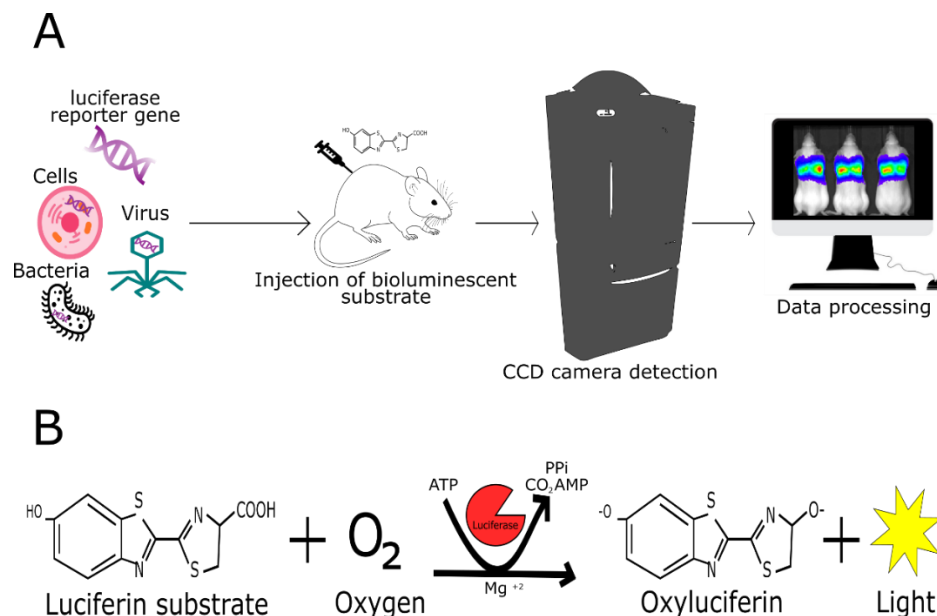
Figure 2. Bioluminescence imaging. A) Luciferase reporter genes or genetically engineered cells, bacteria, or viruses expressing luciferase are inserted into an animal. Then, luciferin is injected into the experimental subject. An in vivo imaging system detects the emitted light, analyses the signals and generates an image. B) Bioluminescence results from an oxidation reaction catalyzed by the luciferase enzyme in the presence of oxygen. Luciferin is transformed into oxyluciferin and light.

In order to track the fate of stem cells *in vivo* via the optical imaging technique BLI, cells are commonly modified with reporter gene vectors, which are maintained transiently, or permanently when integrated into the host cell genome (129,131). Genomic integration of reporter genes can be achieved with high efficiency in most mammalian cell types through the use of VSV-G pseudotyped lentivirus vectors, which bind to the low-density lipoprotein receptor (132). Alternatively, adenovirus, are non-integrating vectors that are increasingly used for a variety of applications (133). A clinically relevant aspect to consider is that the insertion of constructs via viral vectors might result in downstream immunogenicity and potential mutagenesis (127). The choice of reporter genes for optical imaging is limited by the light absorption and scattering characteristics of tissues. Absorption by endogenous molecules like haemoglobins and melanin, as well as scattering, are minimal in the near-infrared part of the spectrum (~650-900 nm), thus leaving an ideal imaging window that can be explored with reporter genes (134).

BLI utilises reporter genes encoding luciferase enzymes for monitoring of exogenous cell fate (131,135). This technique relies on the oxidation of specific substrates by luciferases, which results in light emission (Figure 2). It constitutes the most sensitive optical imaging method in small animals, and the firefly luciferase/D-luciferin system provides light emission at 600 nm, i.e., close to the NIR window. Recent efforts have been made to develop mutant firefly and click beetle luciferases in combination with novel enzyme substrates to shift light emission closer to the NIR window (136). These systems can detect small cell numbers in deep tissues and in the brain (137,138).

Overall, BLI is a non-invasive technique that allows for pre-clinical whole-animal imaging and longitudinal cell tracking, limited mainly by its low spatial resolution (127,139).

1.7.1.2   Computed tomography

Computed tomography (CT) is a non-invasive imaging technique in which a narrow beam of x-rays is spun around a subject, producing 3D anatomical images based on the differential X-Ray attenuation from tissues (140). Its high spatial resolution with high signal-to-noise ratio, high depth of penetration, quantitative capabilities, fast temporal resolution, and cost effectiveness have made it a widely applied imaging modality in the clinic (141).

In recent years, micro-computed tomography (micro-CT) has emerged as an imaging modality to study the biodistribution of nanoparticle-labelled MSCs in animal models (142). Gold has been used for this purpose since gold nanoparticles (GNPs) are easily synthesized, and their surface can be straightforwardly modified and functionalized (143). Moreover, gold has excellent X-ray attenuation properties (144). The primary shortcomings of micro-CT are its low sensitivity and the need for ionising radiation (142,145).

1.7.1.3 Photoacoustic imaging

Photoacoustic effect

1 Short laser light pulses illuminate the tissue of interest.

2 Chromophores in the tissue absorb the light causing the molecules to vibrate (thermoelastic expansion) generating acoustic waves.

3 Soundwaves are detected by a tomographic transducer.

4 Ultrasound signals are reconstructed using advanced algorithms to form an image.
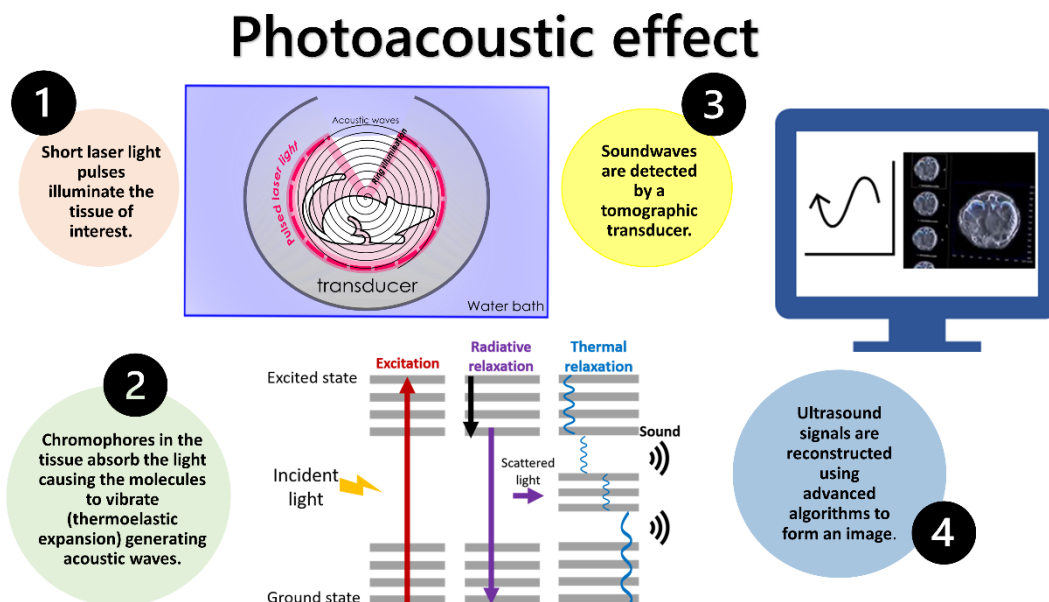
Figure 3. Photoacoustic imaging is based on the photoacoustic effect. In pre-clinical imaging, the specimen is anaesthetised, secured with a sealed pouch with air supply and placed in a water bath. Pulsed infra-red laser light is delivered into the specimen, where it is absorbed by endogenous molecules and labelling probes. It then undergoes radiative and non-radiative relaxation. Non-radiative relaxation is converted into heat, generating a thermoelastic expansion of the absorbing molecules, which results in acoustic waves that are transmitted efficiently in the fluid environments of the body and water bath. The ultrasonic waves are detected by a tomographic transducer, which allows signal analysis, processing and image generation.

Photoacoustic imaging provides functional and anatomical information in real-time and is clinically relevant as it has been used in human diagnostics (146). The depth of penetration is up to several centimetres while maintaining a high spatial resolution (147). Photoacoustic imaging detects the ultrasound waves that result from thermal expansion induced by the absorption of pulses of infrared laser light (Figure 3). The contrast can be endogenous (for example due to absorption by haemoglobin) or exogenous via the use of a contrast agent (148). Gold nanorods are ideal contrast agents for PAI as these particles have a longitudinal plasmon band with strong absorption in the infrared and their surface is easily modifiable (149). In addition to gold nanoparticles, other PAI contrast agents can be used. These include near-infrared fluorescent

protein (iRFP) reporter genes and dyes, single-walled carbon nanotubes, silver nanoparticles and hybrid contrast agents (148–151).

Examples of PAI applications in pre-clinical research include short- and long-term tracking of a MSC line in mice after combined labelling with an iRFP and gold nanorods (150) and monitoring the viability of gold nanorod-labelled MSCs that were coated with a ROS-sensitive near-infrared dye (152).

PAI has also been incorporated into small endoscopes for cell imaging inside the body, allowing much deeper tissue penetration (153). As with other imaging modalities, the general limitation of probe/ signal dilution due to cell division, if not genetically encoded, also applies to PAI contrast agents.

1.7.1.4   Other imaging modalities

Although not used in this thesis, other imaging modalities, such as nuclear imaging and magnetic resonance imaging (MRI) have been used to track MSCs *in vivo* (154)*.*

Nuclear imaging is a non-invasive imaging modality, which offers high sensitivity with well-established imaging probes (155,156). Positron emission tomography (PET) and single photon emission tomography (SPECT) are nuclear imaging technologies that allow sensitive 3D tracking of cells that have been labelled with radiotracers by detection of γ-rays (157).

Limitations in PET and SPECT are the use of radioactivity and the identification of safe dosages of the radiotracers, their leakage into host tissue cells, dilution of signal due to cell proliferation, lack of anatomical information, and the fact that information on cell viability and function cannot always be obtained (154,158).

MRI can be used to study anatomical and physiological processes in the body without requiring ionising radiation. Instead, strong magnetic fields, magnetic field gradients, and radio waves are used in MRI scanners to manipulate the protons and neutrons contained in hydrogen atoms to generate images (159). MRI's ability to image deep within tissues and its high sensitivity and temporal resolution make this technique a good option to track cells non-invasively *in*

vivo. MSCs can be labelled before transplantation by incubation with MRI contrast agents or by using transfection methods (160).

Limitations of MRI cell tracking include the potential toxicity of the cells labelled with MRI contrast agents to the surrounding tissues, as well as the signal dilution due to cell proliferation when the label is not genetic, the difficulty of access to this technique, and its inability to image the lungs (161), were MSC localize after IV injection (162).

1.7.1.5　Multi-modal imaging

As each of the previously described imaging modalities have specific limitations, for robust and reliable assessments of the fate of cells applied in pre-clinical animal models it is necessary to combine different labelling and imaging strategies to allow a more comprehensive analysis (35).

Multimodal cell labelling and imaging approaches are increasingly being used. An example is the combination of BLI with gold-nanorod PAI to evaluate the safety of mouse cells and hUC-MSCs by following their biodistribution after intravenous or intracardiac injection into mice (35). A PAI/BLI approach has also been used to track a MSC line after intracardiac injection into mice (150).

Multimodal imaging can achieve the highest possible sensitivity and spatial resolution of cell tracking over the short- as well as the long-term by maximizing the strengths of the individual imaging modalities. Importantly, such longitudinal experimental designs can significantly reduce the number of animals required in cell-based regenerative medicine.

1.7.2　*Ex vivo* cell tracking

1.7.2.1　Microscopy

The field of life sciences relies on visualization techniques to understand biological events. One such technique is optical microscopy. Microscopes have been at the heart of scientific discoveries since the first one was developed by Leeuwenhoek in the 17th Century (163).

Fluorescence microscopes are a common tool in biology laboratories. Fluorescence microscopy offers a high signal-to-background, sensitivity and specificity (164). However, traditional fluorescence microscopy excites all the fluorescence within the field of view in all dimensions, generating out-of-focus light and inducing photobleaching and photodamage. Moreover, only thin sections can be visualized by this approach (165).

To overcome these limitations, confocal microscopes work on the principle of point excitation in the specimen (diffraction-limited spot) and point detection of the resulting fluorescent signal by using a pinhole, meaning that light detection is restricted to photons originating from the focal plane. This characteristic allows for the visualization of thick specimens by optical sectioning in the Z-axis (166).

1.7.2.2 Optical tissue clearing

As mentioned, confocal microscopy enables 3D imaging of thick sections. Nevertheless, biological samples are inherently opaque and deep tissue imaging is challenging (167,168). Optical tissue clearing is a technique that renders opaque samples transparent by removing lipids and pigments and matching the refractive index (RI) within the sample, while preserving its structure. This process minimizes the heterogeneities within specimens and results in decreased light scattering, allowing deep tissue imaging (169,170).

Whole organ imaging maximizes tissue sampling and reveals 3D structures necessary to accurately evaluate the cellular organization within tissue microenvironments. This circumvents the shortcomings associated with thin section analysis as sampling bias might result in an inaccurate analysis; for instance, many cell types are rare and their distribution within organs is not uniform, meaning they could be missed in thin sections (171).

Despite its many advantages, optical tissue clearing also has several disadvantages, including (i) it is limited to fixed samples; (ii) the use of corrosive solvents and the objective's working distance can limit the microscopes that can be used; (iii) antibody labelling can be challenging when working with thick samples; (iv) high-resolution, deep imaging generates

terabytes of data, posing a challenge for data storage and handling (172). Regardless of its limitations, this field is continually evolving, and technological advances will allow its implementation in a broader range of applications, including MSC tracking.

1.7.2.2.1 Optical tissue clearing methods

The interest in optical tissue clearing has grown rapidly resulting in an abundance of clearing protocols, making its categorization challenging (172). Broadly, clearing methods can be divided into solvent-based (hydrophobic) and aqueous-based (hydrophilic), depending on the chemistry used (173). The first step in either method relies on tissue fixation to preserve morphological and functional information throughout clearing (174).

1.7.2.2.1.1 Solvent-based methods

Solvent-based methods consist of two simple steps: Dehydration and delipidation, and RI matching (169). Dehydration and delipidation remove water and lipids, the most abundant components of tissue. The remaining tissue has an RI of ~1.55; thus, the RI matching step replaces water with a solution similar in RI to reduce light scattering (175).

Samples cleared by solvent-based methods shrink, which can be an advantage when imaging large samples (176). In contrast, disadvantages are the quenching of fluorescent proteins, and the high toxicity of most organic solvents used in these protocols, as well as their capacity to melt plastic and dissolve glues (169,177).

In this thesis the Ethyl-cinnamate (ECi) and stabilized DISCO (s-DISCO) solvent-based methods were used and will be described in more detail in the following sections.

1.7.2.2.1.2 Ethyl-cinnamate clearing

Ethyl-3-phenylprop-2-enoate (ethyl cinnamate [ECi]) is a safe organic solvent that has been used as a food flavour and cosmetic additive since its approval by the Food and Drug Administration in 2007. Its RI of 1.558 makes it an excellent clearing reagent. The clearing protocol consist of dehydrating

samples in a series of pH-adjusted alcohol solutions followed by immersion in ECi (178).

1.7.2.2.1.3   Stabilized DISCO clearing

The stabilized DISCO (s-DISCO) clearing method was developed based on the need to preserve the fluorescence of fluorescence proteins in solvent-based cleared samples. It consists of removing aldehydes and peroxides, known to deteriorate fluorescence, from both dehydrating (tetrahydrofuran) and RI-matching solutions (Di-benzyl ether [DBE]: RI=1.562) using column chromatography with basic activated aluminium, as well as preventing the re-accumulation of these contaminants by the addition of the antioxidant propyl gallate (179).

1.7.2.2.2   Aqueous-based methods

Aqueous-based methods employ water-soluble agents, making them simple, safe and compatible with fluorescent proteins. The two main steps to water based clearing are decolourization and delipidation using detergents, and RI matching (180).

Samples cleared by hydrophilic methods cause sample expansion, which might be an advantage when interested in increasing imaging resolution. The main disadvantage is that water-based clearing is time-consuming taking several days to weeks to fully clear a specimen depending on its size (169).

1.7.2.2.2.1   CUBIC clearing

The clear, unobstructed brain/body imaging cocktails and computational analysis (CUBIC) method was developed by Ueda and colleagues in 2014 (181).

This method consists of removing lipids by immersing the samples in a cocktail of amino alcohol, Triton X-100, and urea. Then, the RI of the samples is matched with a high RI solution. Derived from this protocol, they developed other cocktails for delipidation and RI matching. In the CUBIC-cancer protocol, used in this thesis, the samples are immersed in N-butyl diethanolamine/TritonX-100 and antipyrine/nicotinamide (RI=1.52) (182).

1.8   Thesis overview

The motivation behind this thesis was to assess the safety of MSCs and understand their effects on the host's innate immune system to determine whether they are suitable for clinical use. Understanding how MSCs are distributed throughout the whole body as well as within individual organs following systemic administration is necessary to evaluate safety since it enables the monitoring of any possible harmful effects; for example, tumour formation, mal-differentiation or pulmonary embolism, which can occur following intra-vascular administration due to MSCs becoming trapped in the lung (183).

Non-invasive imaging allows the biodistribution of MSC therapies to be monitored *in vivo*. Individual imaging technologies have strengths and limitations, but combining them in a multi-modal imaging approach enables the maximal amount of information to be obtained from each experiment (184).

In this study, the suitability of a multimodal imaging strategy comprising BLI and micro-CT was assessed for monitoring the whole-body and intra-pulmonary biodistribution of gold nanoparticle-labelled hUC-MSCs that expressed firefly luciferase.

Then, to evaluate the fate and biodistribution of IV delivered hUC-MSCs within the lungs at single-cell resolution, I established an optical tissue clearing method that enabled us to study the localization of the hUC-MSCs in relation to the vasculature, as well as their interactions with the cells of the host's innate immune system.

The mechanisms that underly the potential therapeutic effects of hUC-MSCs are not fully understood, but evidence from animal studies suggests immunomodulatory effects are important. To study the effect of IV administered hUC-MSCs on the host immune system, a combination of flow cytometry and immunostaining was employed.

1.9   Aims and Objectives

The overall goal of this thesis was to evaluate the safety, distribution and fate of MSC therapies using imaging tools.

The study objectives addressed in each chapter are:

1.   To assess the suitability of a multi-modal imaging strategy comprising BLI and micro-CT to assess the whole body and intra-pulmonary distribution of hUC-MSCs, respectively.

2.   To evaluate hUC-MSC biodistribution at single cell resolution using an optical tissue clearing approach.

3.   To investigate the fate of hUC-MSCs in the lung and their effect on innate immune cell populations.

Chapter 2. *In vivo* tracking of administered MSCs by a multimodal BLI/MSOT/micro-CT approach

2   Introduction

The ability to image cells and non-invasively track their fate in animal models has become increasingly important in assessing the long-term safety and efficacy of cell-based regenerative therapies. Moreover, the ability to monitor the biodistribution of cells over time can also offer key insights into their mechanisms of action; for instance, establishing whether engraftment in the target organ is required for the cells to have any beneficial effects.

The intravenous administration of MSCs in mice leads to their entrapment in the pulmonary vasculature and inability to reach other organs (33,35,38). Bioluminescence imaging (BLI) has been key in this discovery. BLI is a non-invasive, whole-animal, pre-clinical imaging modality with high sensitivity and a temporal resolution of seconds to minutes (185). BLI allows longitudinal cell tracking via a reporter gene encoding luciferase, an enzyme that oxidises a substrate to generate light (131,136). However, BLI is limited by low spatial resolution (3 – 5 mm) which does not allow the biodistribution of the cells to be mapped at the intra-organ level (186).

Multispectral optoacoustic tomography (MSOT) is a non-invasive imaging modality that provides functional and anatomical information in real-time. MSOT operates by the photoacoustic effect: incident modulated light energy is absorbed leading to thermo-elastic expansion and the generation of ultrasound waves (187). MSOT uses a range of near-infrared excitation wavelengths, and subsequent spectral unmixing algorithms allows the identification of the optical signatures of endogenous and administered contrast agents. It benefits from high spatial (100 μm) and temporal (0.1 s) resolutions. Its main limitation for tracking cells delivered intravenously is that due to the high air content of the lungs and the behaviour of sound in this medium, MSOT is unable to image this organ.

Computed tomography (CT) is inherently effective for lung imaging due to the native contrast provided by the airspaces. CT is a non-invasive imaging modality that generates 3D anatomical images based on the differential X-Ray

attenuation of materials (140). Its high spatial resolution (50-200 µm) with high signal-to-noise ratio, high depth of penetration, quantitative capabilities, fast temporal resolution, and cost-effectiveness have made it a widely applied imaging modality in the clinic (188). The main drawbacks of CT are that it uses ionising radiation, and its sensitivity is low (142,188).

To distinguish administered cells from endogenous tissue in animal models, cells need to be labelled with a contrast agent. Gold nanoparticles, which exist in different shapes, are a suitable contrast agent for both micro-CT and MSOT. The micro-CT contrast is due to gold's high density and atomic number (140) whilst MSOT contrast can be achieved via the near-infrared (NIR) longitudinal surface plasmon bands that are characteristic of gold nanorods (GNRs) (189). Cell labelling with GNRs is achieved by endocytosis. The tight packing of the GNRs within endosomes can result in the GNRs undergoing plasmon coupling, altering their optical properties and compromising MSOT detection (190). Coating the GNRs with silica prevents plasmon coupling and does not affect cell viability, allowing MSOT to reach its full potential (191).

Our group has previously applied a dual BLI/MSOT imaging strategy to track GNR-labelled cells (190,192). Here, the possibility of expanding this approach to include micro-CT is explored. In addition, we aimed to compare the effectiveness of MSOT and micro-CT for tracking cells labelled with silica-coated GNRs to study the *in vivo* biodistribution of MSCs delivered subcutaneously or intravenously.

2.1   Methods

2.1.1   Nanoparticle characterization

Commercially available silica-coated gold nanorods (GNRs) pre-adsorbed with bovine serum albumin (BSA) were purchased from Creative Diagnostics (2.5 mg/mL). Their properties were characterized using transmission electron microscopy (TEM) (Tecnai G2 Spirit BioTWIN) coupled to a Gatan RIO16 camera and Vis-NIR spectroscopy (FLUOstar Omega, BMG Labtech). GNR stability was studied by incubating the GNRs in cell culture medium at 37°C in a humidified incubator, with 5% CO_2. After 24 h, the GNRs were recovered by

centrifugation at 13000 x g for 20 min, washed three times with dH2O and imaged by TEM. Particles were deposited onto glow discharged fomvar/carbon coated grids for 10 mins, excess wicked off and stained for 20 s with 1% aqueous uranyl acetate.

2.1.2 Cell isolation, generation of reporter cell line and culture

Human umbilical cord-derived mesenchymal stromal cells (hUC-MSCs) were obtained from the National Health Service Blood and Transplant (NHSBT, UK) at passage 3 (p3). The hUC-MSCs were transduced with a lentiviral vector encoding luc2 firefly luciferase (FLuc) reporter under the constitutive elongation factor 1-α (EF1α) promoter and the ZsGreen fluorescent protein downstream of the bioluminescence reporter via an IRES linker. The pHIV-Luc2-ZsGreen vector was kindly gifted by Bryan Welm and Zena Werb (Addgene plasmid #39,196) (138). To obtain a >98% FLuc positive population, the cells were sorted based on ZsGreen fluorescence.

The cells were grown in MEM-α and supplemented with 10% foetal bovine serum (FBS) (Gibco) and kept at 37°C in a humidified incubator, with 5% CO_2.

2.1.3 Cell viability assay

5×10^3 cells were seeded into 96-well plates (Corning) and allowed to attach for 24 h. The viability of hUC-MSCs after 24 h exposure to increasing concentrations of GNRs was determined by the CellTiter-Glo™ Luminescent Cell Viability Assay (Promega Corporation), which generates luminescent signals based on ATP levels. Tests were performed in triplicate with two PBS washing steps between GNR exposure and the assay. Luminescence was measured in a multi-well plate reader (FLUOstar Omega, BMG Labtech).

2.1.4 Assessing the extent of GNR uptake by hUC-MSCs

hUC-MSCs were seeded at 13×10^3 cells/cm^2 into 24-well plates (Corning) and allowed to attach for 24 h. Based on the available material, cells were exposed to 1:100 and 1:10 GNR dilutions (0.125 or 0.25 mg/mL) in cell culture medium for 24 h. After this period, the cells were washed with PBS to remove excess GNRs and fixed with paraformaldehyde (4 % w/v in PBS, pH 7) for

20 min at room temperature (RT). GNR uptake by the cells was assessed by using a silver enhancement solution kit (Sigma SE100) according to the manufacturer's instructions. After rinsing three times with PBS, the cells were imaged by light microscopy with a Leica DM IL microscope coupled to a DFC420C camera.

2.1.5 Animal experiments

Eight- to ten-week-old female albino (C57BL/6) (B6N-TyrC-Brd/BrdCrCrl, originally received from the Jackson Lab) mice were used for all animal experiments. Mice were housed in individually ventilated cages (IVCs) under a 12-h light/dark cycle and provided with standard food and water ad libitum. All animal procedures were performed under a licence granted under the Animals (Scientific Procedures) Act 1986 and were approved by the University of Liverpool Animal Welfare and Ethics Review Board (AWERB).

Mice were injected with 5×10^5 FLuc-hUC-MSCs (hUC-MSCs hereinafter) suspended in 100 μL of PBS by either intravenous (IV) or subcutaneous (SC) administration to the flank, and subsequently imaged via BLI, MSOT and CT, all under terminal anaesthesia with isoflurane.

2.1.6 Bioluminescence imaging

Immediately after cell injection, the animals received a SC injection of D-Luciferin (10 μL/g [body weight] of a 47 mM stock solution). 20 min later, the animals were imaged with an IVIS Spectrum instrument (Perkin Elmer). All data is displayed in radiance (photons/second/centimeter^2/steradian), where the signal intensity scale is normalised to the acquisition conditions.

2.1.7 Multispectral optoacoustic tomography imaging

All imaging was performed in the inVision 256-TF MSOT imaging system (iThera Medical, Munich, Germany).

Tissue-mimicking imaging phantoms with a 2 cm diameter were constructed from 1.5 w/v % agar and 0.4 w/v % intralipid in distilled water (193). Two cavities were created to facilitate insertion of clear straws containing either unlabelled hUC-MSCs or hUC-MSCs labelled with 0.25 mg/mL GNRs. 5×10^5

hUC-MSCs were prepared by labelling and trypsinization as described above and suspended in 100 µL of PBS. Then, the whole volume was inserted into the phantom cavity.

The agar phantoms with inserts were imaged at 61 wavelengths (680 nm to 980 nm in 5 nm steps) at 25°C. 3 frames were measured per wavelength and averaged.

To image mice *in vivo*, their abdomens were shaved and de-epilated using Veet Hair removal cream (Reckitt Benckiser, UK) 24 h before imaging. Mice were imaged at 34°C. In mice receiving subcutaneous hUC-MSC injection, scans were acquired at the site of injection at 61 wavelengths (680 nm to 980 nm in 5 nm steps) in 1 mm slices. 10 frames per wavelength were measured and averaged. In mice receiving intravenous hUC-MSC injection, scans were acquired at the lungs at 61 wavelengths (680 nm to 980 nm in 5nm steps) in 1 mm slices. Additionally, images were acquired through the full volume of all animals at 8 wavelengths (660, 700, 730, 750, 760, 800, 850, 900 nm) in 1 mm slices.

For image processing, the ViewMSOT 4.0.1.34 (iThera Medical, Germany) was used. Data were reconstructed with the back-projection algorithm. Multispectral unmixing was performed using the linear regression algorithm. Images were unmixed for haemoglobin, oxyhaemoglobin, melanin, and the GNR MSOT spectrum. Unmixing for native absorbers is performed to remove their signal contribution toward the total signal within a single voxel to increase the likelihood of quantifying the absorption of the GNRs accurately.

2.1.8 Computed tomography

Agar phantoms with inserts, as used for MSOT, were imaged using an aluminium filter 0.5 mm thick or a 0.06 mm copper filter with an applied X-ray tube voltage of 90 kV in a Quantum GX micro-CT (Rigaku Corporation). Images were acquired with a field of view (FOV) of 25 mm giving a voxel size of 50 µm.

After MSOT imaging, the mice were culled and their carcasses were imaged using an aluminium filter 0.5 mm thick and an applied X-ray tube voltage of 90

kV with the same instrument. Images were acquired with a FOV of 25 mm giving a voxel size of 50 μm. Surface-rendered 3D models were constructed for 3D viewing of the analysed mice. Volume rendered 3D images were generated using the Quantum GX software version 3.0.39.5100.

2.1.9 Statistical analysis

All values in graphs are represented as mean ± standard deviation. The statistical analysis was performed using the GraphPad Prism software. The type of statistical test and the number of replicates included in the analyses are indicated in the figure legends.

2.1.10 Data availability

All datasets from this study are publicly available on Zenodo, http://doi.org/10.5281/zenodo.6624805

2.2 Results

2.2.1 Gold nanorod characterization

To characterise the silica-coated GNRs, their absorbance spectrum was assessed using Vis-NIR spectroscopy which revealed that their longitudinal surface plasmon resonance (LSPR) peaks at 738 nm. The integrity of the silica shell was evaluated after incubation in cell medium as etching might occur (194). After 24 h, the GNRs lose the silica coating resulting in a 25 nm LSPR left shift with a peak at 713 nm (Figure 4a).

The size of the GNRs and the thickness of the silica shell was determined using transmission electron microscopy (TEM). The core size was 55.77 ± 7.32 nm length by 17.36 ± 1.99 nm width with a silica shell thickness of 7.25 ± 1.65 nm (Figure 4b). TEM confirmed the loss of the silica shell after incubation in cell medium (Figure 4c). Despite the LSPR shift, the GNRs absorbance remained within the optical window (700 - 900 nm) where endogenous light absorbance of biological tissues is lower, making them good candidates for cell labelling (195).
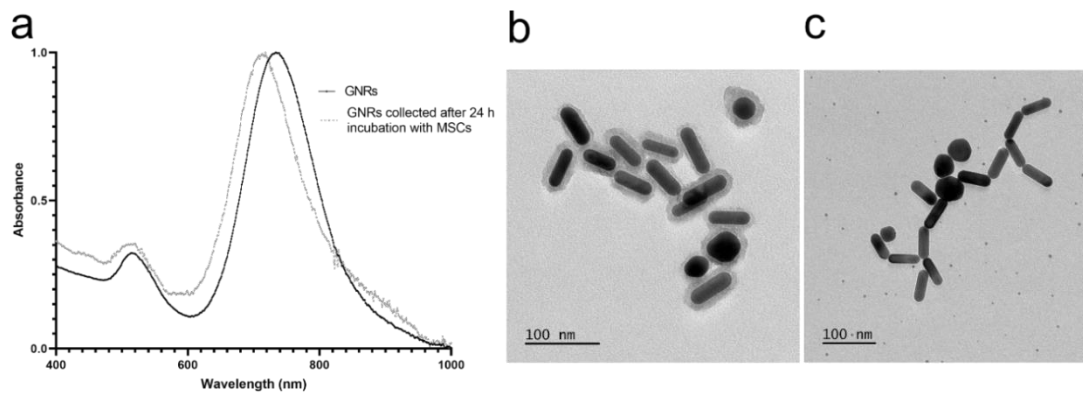
Figure 4. Characterisation of GNRs. (a) Vis-NIR spectrum of GNRs. (b) Representative TEM picture of silica-coated GNRs. (c) TEM image of GNRs 24 h post incubation in cell culture medium.

2.2.2 Gold labelling of hUC-MSCs

Next, we assessed the effect of different GNR concentrations on morphology, labelling efficiency and cell viability. No overt changes in cell morphology were observed via microscopy 24 h after GNR labelling (Figure 5a, top). Using the gold-specific silver staining, GNR uptake by the hUC-MSCs was confirmed at all concentrations, showing a clear dose-dependent uptake trend as indicated by an increase in contrast. The gold particles accumulated in the perinuclear space, consistent with lysosomal accumulation as previously reported (Figure 5a, bottom) (196,197).

To determine cell viability, we quantified the total amount of ATP in cells labelled for 24 h with 0.125 mg/mL or 0.25 mg/mL GNRs. Our results indicated that viability levels were at 94.6 %, and 78.7 % of unlabelled control cells. While a significant reduction in viability was observed at the highest concentration, the GNRs were not overtly toxic to the cells (Figure 5b). Given that labelling with 0.25 mg/mL yielded more uptake (Figure 5a, bottom right), this concentration was taken forward for cell phantom imaging with MSOT and CT.
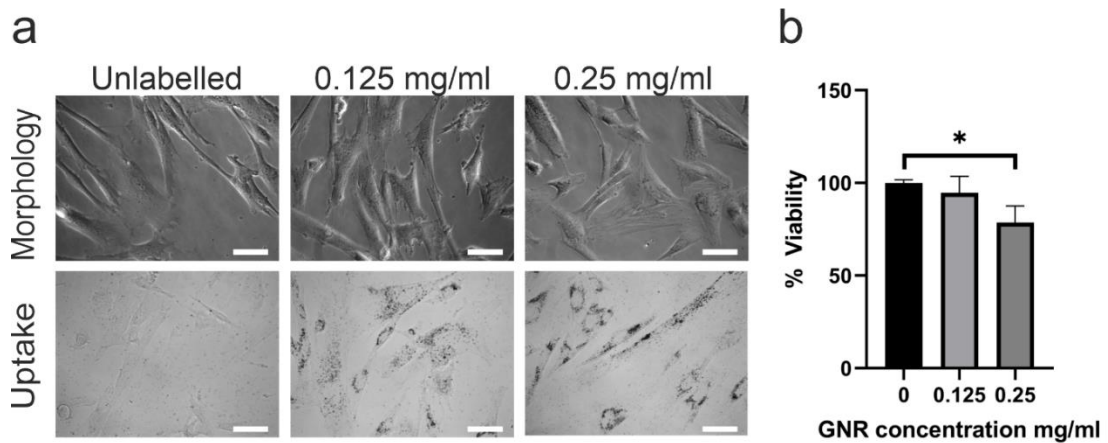
Figure 5. Cell morphology, viability and nanoparticle uptake after GNR labelling. (a) Cell morphology (top) after labelling with GNRs at different concentrations and uptake (bottom) assessed by silver staining. Optical microscopy images of hUC-MSCs labelled with different GNR concentrations for 24 h. Dark contrast is generated by silver-enhanced staining of GNRs. Scale bar 100 µm. (b) Cell viability. One way ANOVA with Tukey's multiple comparisons p<0.05. n=3

2.2.3 MSOT/micro-CT imaging of GNR labelled hUC-MSCs in phantoms

Before *in vivo* imaging, it is important to establish whether the GNR-labelled MSCs can be visualized by MSOT and micro-CT. To do this, 5 x 10^5 hUC-MSCs were suspended in 100 µL PBS (GNR-labelled and control MSCs) into an agar phantom and MSOT intensity was recorded at wavelengths ranging from 680 to 980 nm. The absorbance spectrum of the labelled MSCs measured with the MSOT instrument was broadened compared to the spectrum of unlabelled cells (Figure 6a, left). Nevertheless, labelled cells could still be detected after applying a multispectral unmixing algorithm, where they are seen as a crescent shape due to the cells sedimenting to the bottom of the phantom (Figure 6a, right). Imaging of the phantom by micro-CT showed no difference in contrast between unlabelled and GNR-labelled MSCs when using either the standard filter (aluminium) or a specialized copper filter for the detection of metals (Figure 6b).
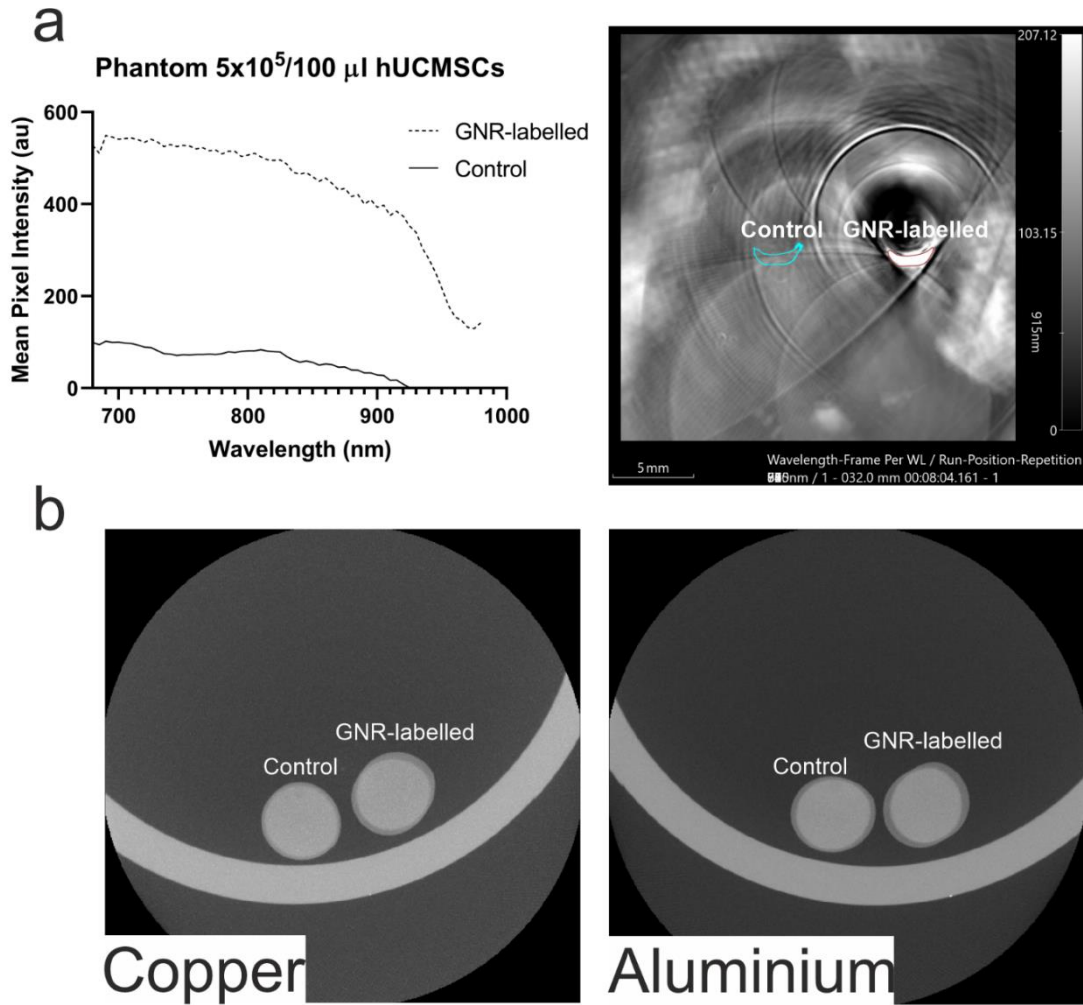
Figure 6. Phantom imaging of GNR-labelled and unlabelled hUC-MSCs. (a) MSOT demonstrates a clear distinction in signal intensity between samples containing labelled or unlabelled cells. The left panel shows the spectrum of GNR-labelled and unlabelled MSCs. The right panel shows a maximum intensity projection of imaging phantoms containing MSCs. (b) micro-CT fails to detect GNR-labelled MSCs, with both samples having identical contrast regardless of the imaging filter used. Copper (left); Aluminium (right).

2.2.4 *In vivo* multi-modal monitoring of GNR-labelled cells administered subcutaneously or intravenously

To further investigate the potential for cell tracking of gold-labelled MSCs by MSOT and CT, 5×10^5 control hUC-MSCs cells or hUC-MSCs labelled with 0.25 mg/mL GNRs were administered either IV or SC.

BLI demonstrated that following either delivery route, the hUC-MSCs showed a strong luminescent signal confirming their presence in the mice. SC injection resulted in the cells localising at the site of injection, with comparable signals at the site of unlabelled (left flank) or gold-labelled cells (right flank). By contrast, when the cells were administered IV, the hUC-MSCs localised to the lungs (Figure 7a).

MSOT confirmed the presence of GNR-labelled cells in the mouse right flank as observed by the high contrast resulting from the GNRs. On the other hand, the unlabelled cells failed to generate optoacoustic contrast, demonstrating the ability of MSOT to detect gold-labelled cells. As expected, the GNR-labelled cells in the lungs could not be detected due to the high air content within this organ (Figure 7b).

Finally, the SC injected GNR-labelled hUC-MSCs could not be detected by CT. A clear image of the lungs could be obtained by micro-CT but the IV-delivered GNR-labelled MSCs were undetectable (Figure 7c).

These results demonstrate that 5×10^5 luciferase-expressing hUC-MSCs can be detected by BLI following both IV and SC administration, gold-labelled hUC-MSCs can be detected by MSOT following SC administration, but micro-CT lacks the sensitivity to detect the hUC-MSCs via either administration route.
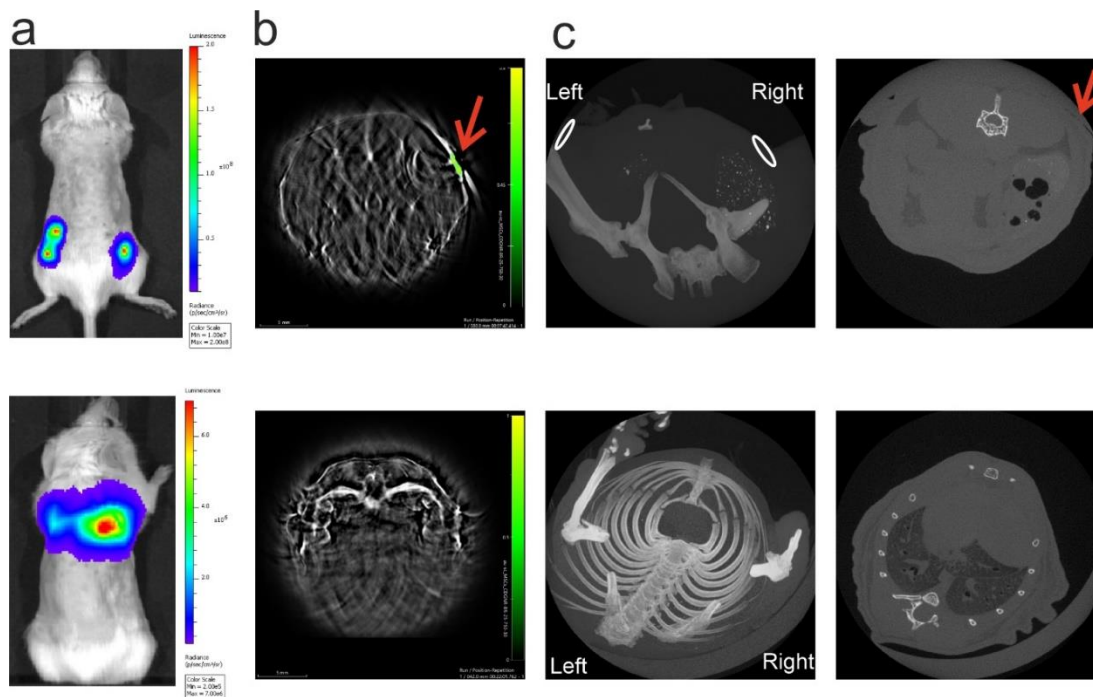
Figure 7. Representative bioluminescence, MSOT and micro-CT imaging of mice after receiving hUC-MSCs. n=6 (a) BLI shows that cells injected SC remain at the site of injection whereas when injected IV, they localise to the lungs. (b) MSOT imaging of mouse after IV or SC injection. GNR labelled cells were distinguished from any internal organ when injected SC (green scale displays GNR-specific signal, indicated by arrow) but not IV. (c) micro-CT fails to generate contrast of GNR labelled cells administered via either route. 3D volume rendered images (left), site of cell location is indicated by ovals. 2D representative micro-CT section of the site of SC injection (top, right; indicated by a red arrow) and lungs (bottom, right).

2.3   Discussion

One aim of multi-modal imaging strategies is the analysis of the whole-body and intra-organ biodistribution of administered cells in preclinical animal models. In this study, we explored the feasibility of combining the sensitivity of BLI with the spatial resolution of MSOT and the ability to image the lungs by micro-CT to track GNR-labelled MSCs *in vivo*.

Photoacoustic imaging uses contrast that can be endogenous or exogenous via the use of contrast agents (190). For cell tracking by MSOT, labelling with gold nanorods has been a method of choice as these particles have a longitudinal plasmon band with strong absorption in the near-infrared (152,190,198,199). Therefore, the silica-coated GNRs used in this study, with

LSPR bands at 738 nm or 713 nm in cell medium are good candidates for generating contrast in cells.

Previously, our group showed that a BLI/MSOT strategy to monitor intracardially administered GNR-labelled FLuc+ mouse MSCs revealed the presence of cells in the head, liver and kidneys of mice with both imaging techniques, proving the efficacy of this methodology for cell tracking (192).

Here, in line with earlier publications, BLI showed that IV injection leads to hUC-MSC accumulation and trapping in the lungs (33,35,38). Due to differences in sound propagation in air, the capacity of MSOT to detect GNR-labelled cells within the lung is hampered. However, following subcutaneous injection, GNR-labelled hUC-MSCs could be detected by MSOT.

micro-CT has been used to track gold-labelled cells in the lung, as well as in other organs *in vivo* and *ex vivo*. Cell labelling strategies to achieve this vary widely (Table 1). Studies describe using gold nanoparticles with different surface chemistries, diameters, initial gold concentrations, and incubation times (200–206,141,207–210). It has been shown that the properties of gold nanoparticles impact cell uptake (200), which agrees with the variation in uptake efficiency reported in these studies. Moreover, cell number, administration routes and injection volumes, tracking time, micro-CT scanners, and scanning settings differ greatly between studies. This reflects the complexity of comparing results in the field of gold-labelled cell tracking by micro-CT. Nonetheless, at least twelve reports suggest that micro-CT enables longitudinal tracking of gold-labelled cells (200–206,141,207–210), although it should be noted that at least 6 of these originate from the same research group.

Table 1. Overview of articles reporting pre-clinical micro-CT tracking of gold labelled cells. IPF = Idiopathic pulmonary fibrosis. RCS = Royal college of surgeons. *Gold nanoparticles (GNP) characteristics in order of appearance are size, coupling/coating, other characteristics. CPP= cell penetrating peptide. PSD= polymer polysulfonamide. PEG= polyethylene glycol, TAT= trans-activator of transcription. RBITC= Rhodamine B isothiocyanate. PLL= Poly-L-Lysine. DMSA= 2,3-dimercaptosuccinic acid. Y = yes. N = No.

Cell type	Cell number	Animal model	Administration route	Tracking time	Labelling conditions	GNP characteristics*	Gold/cell	Imaging	Cells detected?	Ref
hUCMSCs	4×10^6	Mouse IPF	Tracheal infusion	1, 9, 25, 35 days	100 µg/mL 4 h	127.3 nm, CPP-PSD pH-sensitive	313.5 pg	*In vivo*	Y	(200)
hUCMSCs	4×10^6	Mouse IPF	Tracheal infusion	1, 4, 7, 10 days	1000 µg/mL ≥ 12 h	40 nm, PEG-TAT RBITC-labelled	920 pg	*In vivo*	Y	(201)
hUCMSCs	4×10^6	Mouse IPF	Tracheal infusion	1,3,5,7,10days	200 µg/mL 12 h	40 nm, temperature responsive	120 pg	*In vivo*	Y	(202)
hUCMSCs	1.5×10^6	Mouse IPF	Tracheal infusion	3,48 h, 9, 16, 23 days	200 µg/mL 24 h	10.7 ± 1.7 nm, BSA-PLL	293 pg	*In vivo*	Y	(203)
Rat glioma C6 cell line	1×10^5	Wistar rat	Stereotactic injection into brain	16 days Ex vivo	50 µg/mL 22 h	50 nm, colloidal	0.04 ng	*Ex vivo*	Y	(204)
hUCMSCs	2×10^5	RCS rat model	Subretinal injection	1, 15, 30 days post injection	1.4×10^8 particles/mL 24 h	80 nm, colloidal	Not mentioned	*In vivo*	Y	(205)
Human periodontal ligament stem cells (hPDLSCs)	1×10^6	Wistar rats	- Intramuscular - Subcutaneous - Submucosal - Subgingival	0, 2, 5 days	50 µg/mL 12 h	40nm, PLL-hydrobromide RBITC-labelled	Not mentioned	*In vivo*	Y	(206)
hMSCs (undetermined source)	2×10^4 or 5×10^5	Sprague Dawley rats	Stereotactic injection into brain	30 min post injection	100 µg/mL 12 h	40 nm, PLL RITC-labelled	382.5 pg	*In vivo*	Y	(141)

Bone marrow MSCs	1×10^6	BL/6 IPF	Tracheal infusion	7, 14, 21 days	200 µg/mL 24 h	12.2 nm ± 1.59 nm, Albumin-PLL ICG-labelled	218 pg	*In vivo*	Y	(207)
hMSCs (undetermined source)	1×10^6	Nude mice	Intra-arterial (carotid artery)	24 h	52 µg/mL 22 h	50 nm, colloidal	332 ± 2 µg	*Post mortem*	Y	(208)
F98 rat glioma cells	1×10^5 or 2×10^5	Nu/nu mice	Stereotactic injection into brain	6-8 days after tumor implantation	No dose mentioned 4 h.	50 nm, Colloidal	26,500 GNPs	*In vivo*	Y	(209)
Dental pulp MSCs	5×10^5 and 1×10^6	Mouse Silicosis	Intranasal	Daily up to 7 days	90 µg/mL 24 h	26.4 ± 0.96 nm, DMSA	4 pg	*In vivo*	N	(210)

In contrast, despite BLI and MSOT confirming the presence of cells in the mice, our study failed to detect contrast generated by the gold-labelled MSCs by micro-CT regardless of whether they were delivered SC or IV. Silva *et al.* also reported failure to detect labelled cells *in vivo* by micro-CT (210), and of the studies reported in Table 1, this is the only one with negative results. They labelled hMSCs with dimercaptosuccinic acid (DMSA) gold nanoparticles (GNPs) for 24 h at a concentration of 90 µg/mL and observed a slightly higher contrast than unlabelled MSCs in micro-CT phantoms, but the difference was not significant, and intranasal inoculation of labelled MSCs did not result in detectable contrast by *in vivo* micro-CT.

Here, although not highly toxic, the gold concentration used showed reduced cell viability after 24 h. The fact that other groups have used higher labelling concentrations might be explained as GNP toxicity depends on functionalisation and uptake (144). The effects of surface modifications have been studied in various cell lines. Naked GNRs negatively affect mammalian cells at concentrations as low as 0.7 µg/mL while silica coating increases the cell tolerance to GNRs (211) consistent with the viability of hUC-MSCs exposed to the silica-coated GNRs in this study.

Silica shell thickness plays a key role in preventing plasmon coupling and preserving the GNRs optical signature after cell uptake, which are important considerations for optimal MSOT imaging (190). While the commercial GNRs used here lost their silica coating during labelling (contrarily to those used in (190)), MSOT still enabled the detection of the GNR-labelled hUC-MSCs in the mouse flanks. In contrast to MSOT, aggregation might work in favour of the detection of gold by micro-CT by preventing the GNRs from being removed by exocytosis which would reduce intracellular gold (202,212,213). Despite this aggregation phenomenon potentially taking place in our study, the GNR hUC-MSCs were still undetectable by micro-CT.

High gold uptake per cell is necessary to achieve good contrast as micro-CT signal increases proportionally with increasing gold concentrations; however, cell uptake usually reaches saturation (214,215). The GNRs used here had an average core size of 56 x 18 nm, which results in high uptake by receptor-

mediated internalization (216). We used the highest concentration that did not induce overt toxicity. Despite this, no micro-CT signal was detected in our study.

The discrepancy between our results and those of other studies raises the question of the limit of detection of micro-CT for gold. This determination is not straightforward as micro-CT scanning conditions along with the properties of the gold nanoparticles impact X-ray attenuation (217).

Attempts at determining the minimal amount of gold necessary to achieve contrast in micro-CT have been made using phantom imaging. Galper *et al.* established that the attenuation of gold is 5.1 HU/mM (218). This is a physical parameter that should not vary between research groups. We attempted to evaluate the attenuation of gold corresponding to results in the publications reporting cell tracking with micro-CT. Table 2 shows those estimated HU/mM attenuations. To arrive at these numbers, we calculated the molar concentration of gold in the micro-CT phantoms used in the studies using equation 1:

$$\frac{\left(\frac{(Au\ per\ cell\ [g])}{197} * cell\ number\right)}{cell\ suspension\ volume\ (L)} = Au\ concentration\ [M]$$

(1)

It is noteworthy that most studies show a much higher HU/mM attenuation in their phantom studies when compared to Galper's data. Considering the 5.1 HU/mM attenuation, Cormode and colleagues concluded that 5.8 mM is the minimum detectable gold concentration (219). Considering a cell volume of 8 pL, the minimum amount of gold per cell necessary to achieve a 5.8 mM (1.16 g/L) concentration for a voxel filled entirely with labelled cells is 9 pg of gold/cell. Equation 2:

$$cell\ volume * Au\ concentration = min\ amount\ of\ Au\ per\ cell$$

(2)

The gold/cell column in table 2 shows that all studies except for Silva *et al.* (210) achieved a nanoparticle load per cell higher than the 9 pg detection

threshold, potentially explaining why Silva's study is the only one that failed to visualize the gold-labelled cells by micro-CT. It is thus clear that extremely high cellular uptake of GNPs is necessary in order to obtain micro-CT contrast, which increases costs and may adversely affect cell health.

Table 2. HU/mM attenuation estimated from the published literature where micro-CT imaging of gold-labelled cell phantoms was undertaken. Question mark (?) indicates that the cell No. was assumed to be 1 x 10^6 cells as this information was not indicated in the papers. Asterisk (*) indicates that the cell suspension volume was estimated based on a pellet of 1 x 10^6 cells.

Cell type	Cell No.	Cell suspension volume µL	Labelling concentration µg/mL	Incubation time	GNP characteristics	Gold/cell pg	Au [mM]	HU	HU/mM	Ref
hUCMSCs	1 x 10^6	30*	100	4 h	127.3 nm pH-sensitive CPP-PSD@Au	313.5	53	2119	39.9	(200)
hUCMSCs	1 x 10^6	30*	1000	12 h	40 nm Au@TAT	920	156	660	4.2	(201)
hUCMSCs	?	30*	200	12 h	40 nm temperature responsive GNPs	120	20	423	20.8	(202)
hUCMSCs	1 x 10^6	30*	200	24 h	10.7 ± 1.7 nm Au@BSA@PLL	293	50	4921	99.3	(203)
hMSCs	1 x 10^6	50	100	12 h	40 nm AuNP-PLL-RITC Poly-L-Lysine	382.5	39	813	21.0	(141)
BMSCs	3 x 10^6	30*	200	24 h	(AA@ICG@PLL)	218	36	156	4.2	(207)
Dental Pulp MSCs	?	30*	90	24 h	Au-DMSA	4	0.7	353	521.2	(210)

The main limitation of our study is that we did not quantify the amount of gold per cell. Given the lack of contrast observed during the imaging of cell phantoms as well as *in vivo*, it is clear that even at the highest labelling concentration, the GNRs did not accumulate in high enough numbers inside the cells and thus, were not detectable by micro-CT. On the contrary, they were easily detectable in the same conditions by MSOT when injected subcutaneously, showing that this imaging modality is significantly more sensitive than micro-CT.

2.4   Conclusions

We tested the feasibility of a non-invasive, multimodal imaging approach that utilises a combination of GNRs and reporter genes to track MSCs after subcutaneous or intravenous injection *in vivo*. This labelling approach did not affect cell morphology and viability of hUC-MSCs significantly and allowed for robust tracking of the cells by BLI for both IV and SC delivery. The GNR-labelled cells were detectable by MSOT when injected subcutaneously validating the ability of a BLI/MSOT tracking approach. Although micro-CT produces anatomical images of the lungs, the same GNR-labelled cells could not be detected within this organ or in the flanks of the mice indicating that the cells did not carry enough contrast agent to be tracked by micro-CT.

To provide enough contrast for micro-CT imaging, large amounts of gold are necessary. However, high labelling concentrations might impair cell viability making micro-CT tracking of gold labelled cells challenging.

In summary, our study found that multimodal imaging of MSCs labelled with gold nanoparticles and the reporter gene firefly luciferase allows BLI and MSOT detection of administered cells *in vivo*, however micro-CT lacks sensitivity toward gold under the conditions investigated.

Chapter 3. Establishment of an optical tissue clearing strategy for detecting administered hUC-MSCs in mouse lungs

3 Introduction

Cell-based therapies include the administration of exogenous cells to trigger a regenerative response. Several sources of therapeutic cells have been investigated (220). The majority of clinical trials have explored the potential of mesenchymal stromal cells (MSCs). Although it has been reported that MSCs are multipotent, their therapeutic effects *in vivo* are mostly mediated by secreted factors that promote the repair of injured host tissues and modulate the host's immune system (221). Increasing evidence suggests that the intravenous administration of MSCs and various other cell types is followed by the entrapment of most of the administered cells in the lung capillaries (150,162,222). Little is known about the role of therapeutic cells in this organ as cell persistence is low, with most cells dying within the first 24 h post systemic administration (223).

One of the most common safety issues upon intravascular infusion of MSC therapies are thromboembolic complications (224–226). Thus, it is important to analyse the distribution of the MSCs within the vasculature to determine their potential to occlude the pulmonary vessels (36). Moreover, MSCs can exert their therapeutic effects via immune effector cell mediation triggered by MSC death in the lungs (119), but the interactions of the MSCs with different immune cell populations in the lung remains to be established. Cell tracking by following the biodistribution of labelled therapeutic cells within tissues might offer insights into these questions.

Cell tracking in tissues at single-cell resolution has been traditionally done using thin section histological analyses. Although useful, the field of view is limited and might not be an accurate representation of the whole organ (227). Investigating the biodistribution of cells in thick tissue sections offers an advantage to thin-section analyses (171,228), but biological tissues are dense and inherently scatter light, preventing the visualization of deeper structures (168). Optical tissue clearing is a technique that minimizes the heterogeneities within tissues by removing lipids and matching the refractive index (RI)

between the sample and the imaging medium (170). As a result, opaque samples become more transparent and the decrease in light scattering allows deep-tissue imaging (169).

Optical tissue clearing, in combination with molecular labelling and optical sectioning microscopy, has become an important tool for 3D imaging in several biological applications including investigating the biodistribution of cells in whole organs (229,230).

Despite the many advantages of optical tissue clearing, practical limitations to the applicability of clearing protocols for imaging remain. Several protocols have been developed in recent years (172) and selecting between them requires careful consideration of a range of parameters to achieve the optimal trade-off for specific applications. Sample size and tissue composition impact the clearing speed and limit the microscopes that can be used when imaging large samples (231). Fluorophore preservation poses another challenge as certain clearing protocols are incompatible with fluorescent probes (232). In particular, preservation of protein-based fluorescence and lipid staining remain open challenges in the field (170). The compatibility of immunostaining with the chemicals used for clearing as well as antibody penetration in large samples requires testing and optimization (231). Moreover, certain parameters differ between tissue and sample types, and no single clearing approach fits all, necessitating the use of application/tissue specific protocols.

Several studies have focused on clearing lung tissue to investigate biological processes (232–234). An example is blood vessel formation, achieved by labelling the intact vasculature with the organic dye Evans Blue (235). Nevertheless, no study to date has performed optical tissue clearing to investigate the biodistribution of administered MSCs within the lungs. Here, we compared three different tissue clearing protocols: CUBIC, a modified s-DISCO and ECi. CUBIC was chosen based on its ability to preserve fluorescent proteins (236); ECi due to its cost-effectiveness, safety and ease of access to the reagents required (237); and s-DISCO due to its reported compatibility with fluorescent proteins despite being a solvent-based method (26).

The comparison of these methods was performed with the aim of imaging thick lung slices in 3D to track MSCs labelled with the genetic reporter tdTomato and study their biodistribution within the host's lung. Moreover, as a proof of principle, we explored the possibility of using optical tissue clearing to investigate the interactions of the administered MSCs with the host's endothelial cells and immune microenvironment.

3.1 Methods

3.1.1 Cell culture and stable cell line generation

Human umbilical cord-derived mesenchymal stromal cells (hUC-MSCs) were obtained from the National Health Service Blood and Transplant (NHSBT, UK) at passage 3. The hUC-MSCs were transduced in the presence of 6 µg/ml DEAE-Dextran with a lentiviral vector pCDH-EF1-Luc2-P2A-tdTomato, encoding luc2 firefly luciferase (FLuc) reporter under the constitutive elongation factor 1-α (EF1α) promoter and upstream of a P2A linker followed by the tdTomato fluorescent protein (gift from Kazuhiro Oka; Addgene plasmid # 72486; http://n2t.net/addgene:72486; RRID: Addgene_72486). To obtain a >98% transduced population, the cells were sorted based on tdTomato fluorescence (BD FACS Aria). Cells were cultured in α-MEM supplemented with 10% FBS at 37°C and in 5% CO_2, and passaged at 80% confluence.

3.1.2 Animal experiments

Eight to ten-week-old female albino mice (C57BL/6) (B6N-Tyr^{C-Brd}/BrdCrCrl (n=15), originally purchased from the Jackson Lab) were used for all animal experiments. Mice were housed in individually ventilated cages (IVCs) under a 12 h light/dark cycle and provided with standard food and water ad libitum. All animal procedures were performed under a licence granted by the Home Office under the Animals (Scientific Procedures) Act 1986 and were approved by the University of Liverpool Animal Welfare and Ethics Review Board. Mice received 2.5 x 10^5 FLuc-tdTomato-hUC-MSCs suspended in 100 µL of PBS by intravenous (IV) administration via the tail vein under inhaled anaesthesia with isoflurane.

3.1.3 Bioluminescence imaging

In vitro bioluminescence was performed by seeding a range of cell densities (from 625 to 2 x10^4 cells/well) into an optical bottom 96-well plate with black walls (#165,305, ThermoFisher). The cells were allowed to attach for 3 h prior to the addition of 5.12 mM D-Luciferin. Imaging was performed immediately after substrate addition without an emission filter, a 13.3 cm field of view (FOV), f-stop of 1 and a binning of 8. For *in vivo* bioluminescence imaging, mice received a subcutaneous (SC) injection of D-Luciferin (10 µL/g [body weight] of a 47 mM stock solution) after FLuc-tdTomato-hUC-MSCs (hUC-MSCs hereinafter) injection. After 20 min, the animals were imaged with an IVIS Spectrum instrument (Perkin Elmer). Data are displayed in radiance (photons/second/centimeter^2/steradian), where the signal intensity scale is normalised to the acquisition conditions. Acquisition was performed without an emission filter, a 22.8 cm FOV, f-stop of 1 and a binning of 8.

3.1.4 Tissue preparation

Immediately after bioluminescence imaging (BLI), the animals received an IV injection of Evans Blue (Sigma; 3 µl/g) for vascular labelling. The dye was allowed to circulate for 5 min before proceeding with a retrograde perfusion fixation protocol (234). The animals received an intraperitoneal overdose of pentobarbital (Pentoject, 100 µl) followed by cannulation of the abdominal aorta, opening of the vena cava and flushing PBS with a manual pump at a constant pressure of 200 mbar (supplementary figure 1) for 6 min, to remove all blood cells, followed by 6 min perfusion with 4% paraformaldehyde (PFA) to fix the whole animal. The total volume of each solution used per animal was 40 ml. The trachea was tied tightly with a surgical suture before opening the thoracic cavity for lung dissection. Finally, the lungs were post-fixed in 4% PFA overnight at 4°C.

3.1.5 Optical tissue clearing

Solvent-based tissue clearing: modified s-DISCO and ECi

The general procedure consists of dehydrating fixed samples by sequentially adding pH9-adjusted solvents chilled to 4°C. After dehydration, the respective RI matching solution was added until the samples reached optimal transparency for 3D imaging (179,237). Solvents used and incubation duration are detailed in _Table_ 3.

Table 3. Solvent based clearing protocols. The RI matching solvents used were Ethyl cinnamate (ECi), Dichloromethane (DCM), and Dibenzyl ether (Dibenzyl ether [DBE] - Sigma-Aldrich).

	500 µm sections		Whole organ	
	s-DISCO	ECi	s-DISCO	ECi
1-propanol 50%	10 min	10 min	30 min	30 min
1-propanol 80%	10 min	10 min	30 min	30 min
1-propanol 100%	3x 10 min	3 x 10 min	3 x 30 min	3 x 30 min
DCM	5 min	-	20 min	-
DBE w/ 0.4% propyl gallate	storage	-	storage	-
ECi	-	storage	-	storage

Aqueous-based tissue clearing: Clear, Unobstructed Brain/Body Imaging Cocktails and Computational Analysis (CUBIC)

The CUBIC-cancer protocol was followed (182). Briefly, CUBIC-L2 solution (L2), for delipidation and decolourisation, was prepared as a mixture of 10 w%/10 w% Triton X-100 (Sigma-Aldrich)/N-buthyldiethanolamine (B0725 Tokyo Chemical Industry). CUBIC-R2 solution (R2), for RI matching (RI=1.52), was prepared as a mixture of 30% (w/v) nicotinamide (Sigma) and 45% (w/v) antipyrine (Sigma).

For whole-organ clearing, 4% PFA fixed lungs were washed with PBS for 2 h, three times each, followed by immersion in CUBIC-L1 solution (L1) (50% (v/v) mixture of water and CUBIC-L2) for 6 h at 37°C. Then, the organs were immersed in L2 solution at 37°C for 48 h. L2 solution was refreshed after 24 h during this process. After decolourisation and lipid clearing, the organs were washed with PBS at room temperature for 2 h, followed by immersion in CUBIC-R1 solution (R1) (50% (v/v) mixture of water and CUBIC-R2) for 6 h at room temperature. Finally, organs were immersed and stored in R2 solution at room temperature overnight.

3.1.6 Size change and transparency measurements

Fixed adult mouse lungs were cleared and imaged before and after clearing. The size and transparency of the samples were outlined and calculated using ImageJ (by drawing the region of interest and measuring mean pixel intensity) (NIH, USA) (239). The area (cm^2) of each single lung lobe was calculated by delineation using the ROI tool and the average of all samples was set as the before value for all comparisons. The median grey value of the cleared organ image was used to measure transparency by normalizing the obtained value to the background of the same image (240).

$$Transparency = \frac{sample\ median\ grey\ value}{average\ background\ median\ grey\ value} * 100$$

3.1.7 Immunofluorescence

The lungs were cryoprotected in 15% sucrose followed by 30% sucrose over a period of 48 h before embedding in optimal cutting temperature (OCT) medium. The samples were cut into 500 μm sections on a cryostat (Thermo Scientific, Microm HM505E) at -20°C and stored at -80°C.

For CUBIC staining, the tissue sections were delipidated by immersion in 50% CUBIC-L for 30 min at 37°C followed by overnight incubation in CUBIC-L at 37°C with shaking. All sections were washed 3x with PBS for 5 min. Tissues were incubated with zenon Alexa Fluor® 647 (Invitrogen, Z25008) labelled human mitochondria primary antibody (Merck, MAB1273), 1:500 for 48 h at 4°C and washed with PBS overnight at 4°C. For CD31 (R&D systems,

AF3628) staining, the lung sections were blocked overnight with PBS-TxDBN buffer (1x PBS, 2% TritonX-100, ddH$_2$O, 2% BSA, 20% DMSO) at 37°C and incubated with CD31 1:100 antibody for 72 h at 37°C. Upon an overnight washing step, secondary antibody (Alexa Fluor® 647) incubation was done at 37°C for 24 h. After the final overnight washing step, solvent-based or CUBIC clearing was performed as indicated in the clearing section.

3.1.8 Imaging

Cells in culture were imaged by light microscopy with a Leica DM IL microscope coupled to a DFC420C camera. Confocal images were acquired on a Leica DMi8 with Andor Dragonfly spinning disk, coupled to an EMCCD camera using a 10x/0.45 air objective. Z-stacks were captured using the 488, 561 and 637 nm laser lines. The emission filters used were 525/50, 600/50 and 700/75. Maximum intensity projections, three-dimensional reconstructions and image analysis were done using the IMARIS (Bitplane) software packages, processed with ImageJ 3D viewer (239). 3D surfaces were obtained via un-stacking the .ims image in Image J and reconstructed via variable threshold intensity (3D slicer). 3D elaboration was performed using NVIDIA ® Quadro 6000 GPUs, and exported as .stl.

3.1.9 Statistics

The GraphPad Prism software was used to conduct the statistical analysis. The mean and standard deviation are used to represent all values in graphs. The number of replicates included in the analyses, as well as the type of statistical test used, are given in the figure legends.

3.1.10 Data availability

The data that support the findings of this study are available to download from Zenodo at http://doi.org/10.5281/zenodo.6638775

3.2   Results

3.2.1   BLI imaging reveals hUC-MSCs entrapment in the lungs
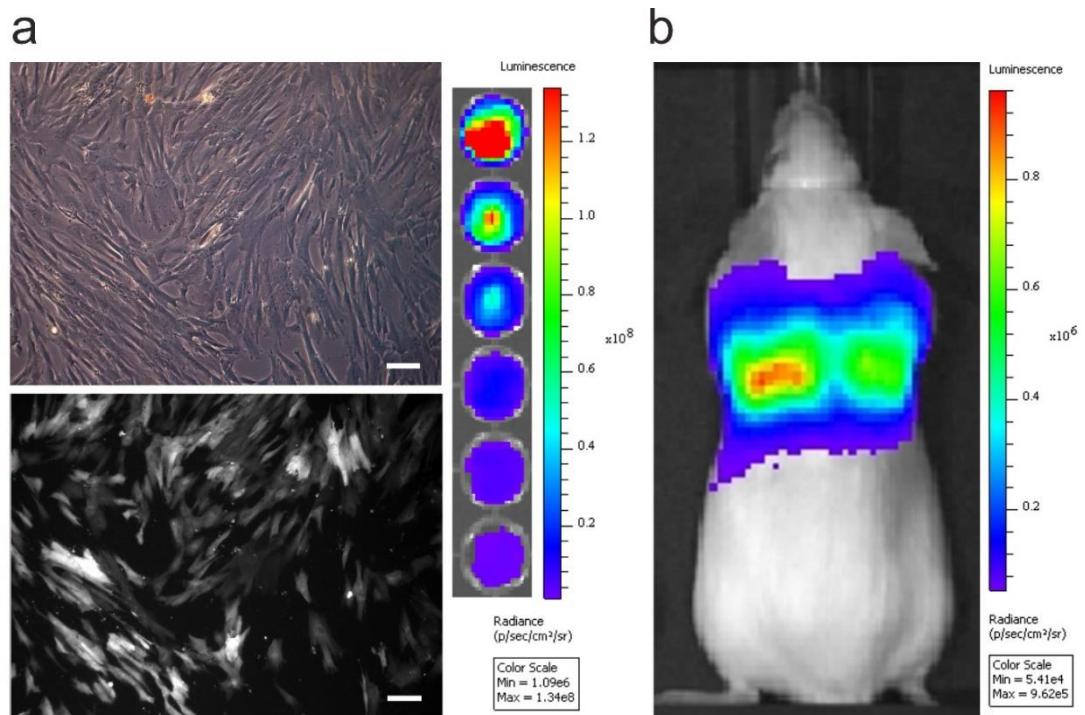
Figure 8. In vitro and in vivo imaging of hUC-MSCs. a) Transmitted (top) and epifluorescence (bottom) images of transfected hUC-MSCs in culture. Scale bar = 100 µm (left). Representative image of hUC-MSCs seeded at decreasing concentrations (from 2 x 10^4 to 625 cells/well) and treated with 5.12 mM D-Luciferin (right). b) In vivo biodistribution of 2.5 x 10^5 hUC-MScs 20 min after intravenous administration.

To monitor the fate of MSCs administered in mice, the cells were stably labelled with fluorescent and luminescent reporters. The tdTomato reporter was used as it is the brightest red shifted fluorescent protein available, helping overcome the high autofluorescence of tissues (Figure 8a, left) (241). In vitro, the level of emitted bioluminescence is dependent on the number of hUC-MSCs present (Figure 8a, right). Immediately after IV administration of hUC-MSCs their localisation was monitored *in vivo* using bioluminescence imaging, allowing us to observe that the hUC-MSCs were localised to the lungs (Figure 8b).

3.2.2 Lung clearing comparison after different optical tissue clearing methods

Whilst bioluminescence is useful for monitoring the whole body biodistribution of hUC-MSCs *in vivo*, the low spatial resolution precludes a detailed analysis of the cell distribution within the lung. To better understand why the cells were retained in the lungs, and to analyse their impact on the host at the molecular, cellular and tissue level, we sought to monitor cell biodistribution in the lung tissues ex vivo at single cell resolution. To achieve this, we compared three different optical tissue clearing methods that would enable the cells to be visualised in thick lung sections; CUBIC, a modified s-DISCO and ECi. s-DISCO and ECi are solvent-based methods that cleared whole mouse lungs in a matter of hours, while CUBIC uses water-based reagents and required several days to entirely clear tissues with an average lipid-clearing of 3 days (Figure 9a).

To reach transparency, the samples were immersed in RI matching solutions and representative images of the cleared lungs are shown in Figure 9b. We quantified the resulting levels of transparency from digital images taken of the tissues before and after clearing. The CUBIC protocol resulted in the highest transparency of the lungs, reaching close to 90%, while s-DISCO and ECi demonstrated transparency of approximately 30% (Figure 9c). Additionally, we calculated the size change and found that there was a significant increase in size after CUBIC clearing. The opposite was observed after s-DISCO and ECi clearing, where the samples shrunk (Figure 9d). We observed the presence of adequate air spaces, bronchioles, alveolar sacs, and blood vessels in images acquired by recording tissue autofluorescence. Overall, this indicates that the characteristic lung structure remains detectable after all the clearing protocols (Figure 9e).
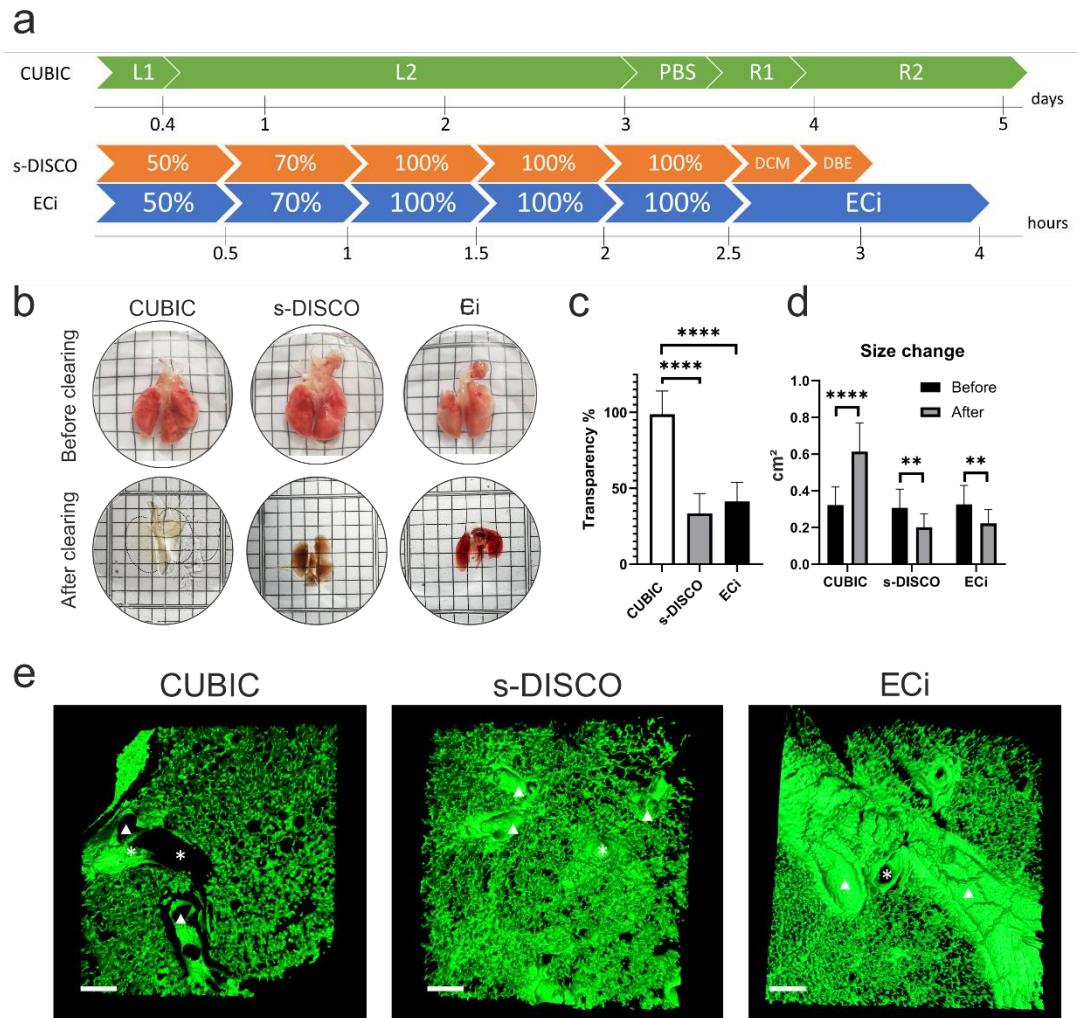
Figure 9. Comparison of the effect of different clearing methods on lung tissue. A) Timeline required to clear whole lungs using each protocol. L1 = Delipidation and decolourisation cocktail 50% (v/v). L2 = Delipidation and decolourisation cocktail 100%. R1 = RI matching cocktail 50% (v/v). R2 = RI matching cocktail 100%. Percentages in s-DISCO and Eci represent the solvent concentration. B) Representative images of lungs before (top row) and after (bottom row) optical tissue clearing. Each line of a square represents 2 mm. c) Quantification of transparency of lung samples after optical tissue clearing (240). One-way ANOVA with Tukey's multiple comparisons test p < 0.05 n = 3. D) Size change (area cm^2) of single lung lobes before and after each tissue clearing method was evaluated using multiple paired t-tests p < 0.05 n = 3. E) 3D variable threshold intensity surface reconstruction of lung sections cleared by the different protocols. CUBIC, s-DISCO and Eci cleared lungs show that the characteristic lung structures such as large blood vessels [indicated by asterisks (*)], and airways such as bronchi (indicated by arrowheads) are preserved after optical tissue clearing. Processing artefacts, due to tissue dehydration, are observed as cracks in the Eci cleared sample. Scale bar = 150. 3D MIPs before reconstruction can be viewed in supplementary figure 2.

3.2.3 Effect of different optical tissue clearing methods on the preservation of fluorescence in the lungs

The ability to detect fluorescent dyes and fluorescent proteins is essential to study the environment and fate of the injected cells, yet fluorescence quenching is one of the key limitations of many organic solvent-based optical tissue clearing methods. Therefore, we compared the effect of CUBIC, s-DISCO and Eci on the tdTomato fluorescent label intensity of the UC-MSCs. By acquiring fluorescent images of cleared 500 µm lung sections immediately after clearing and 3 days after the samples had been stored in RI matching medium, we found that CUBIC preserved tdTomato fluorescence upon all clearing steps and that storage did not affect the fluorescence of tdTomato. On the other hand, the solvent-based methods increased background autofluorescence, and also appeared to quench the tdTomato fluorescence (Figure 10a). Interestingly, clearing thinner lung sections (100 µm) using a reduced dehydration time (Supplementary table 1) allowed the detection of tdTomato immediately after both, s-DISCO and Eci, indicating that dehydration time is a key parameter in preserving the fluorescence of proteins. Moreover, storage of the thin sections in Eci for 3 days did not result in tdTomato quenching, but storage in dibenzylether (DBE) in the modified s-DISCO protocol did (Supplementary figure 3).
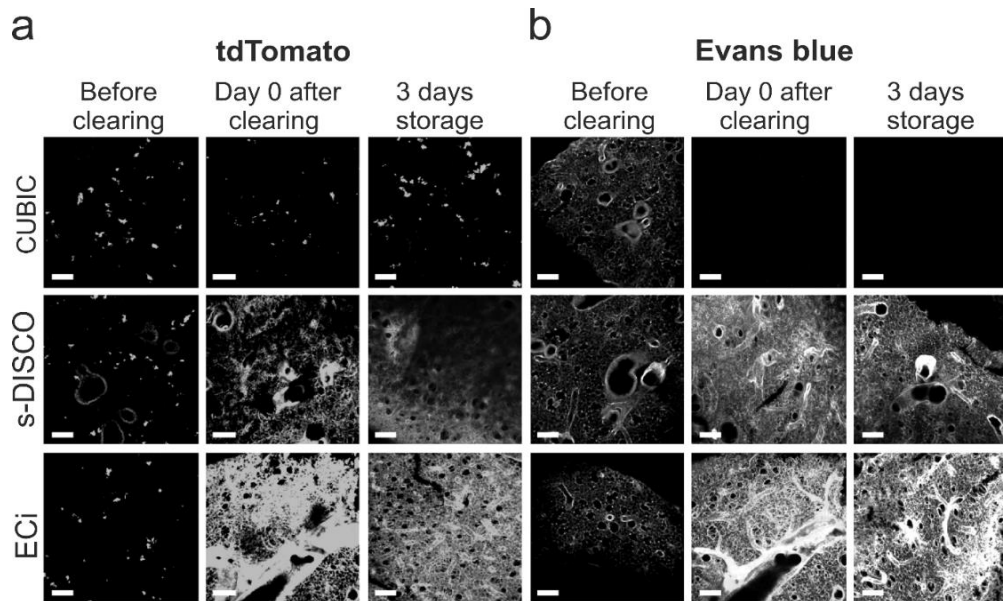
Figure 10. Fluorescence preservation of tdTomato and Evans Blue after clearing thick lung sections. Impact of CUBIC, s-DISCO and ECi clearing on the fluorescence of a) tdTomato or b) Evans Blue in 500 µm thick lung sections before, immediately after, and after storage for 3 days in RI solution. All confocal images are maximum intensity projections (MIPs), taken from the surface of the slices. The same exposure times and display settings were used to acquire and visualize the images to reflect the change in the fluorescence preservation accurately. Scale bars = 150 µm.

Systemic cell administration results in a large fraction of the cells becoming entrapped in the lung's vasculature (36). Since Evans Blue allows the labelling of the vasculature to analyse IV administered hUC-MSCs in the context of the pulmonary 3D vascular network, we determined whether Evans Blue labelling was affected by the clearing protocols. Our analysis showed that Evans Blue is incompatible with CUBIC since all fluorescent signals were lost (Figure 10b). By contrast, Evans Blue fluorescence was not only preserved by s-DISCO and ECi, but the fluorescence intensity of the dye had increased after clearing with either solvent-based method. We speculate that the shrinkage of the samples leads to a higher density of fluorescent molecules and subsequent increase in signal intensity, since the samples were imaged under the same conditions.

3.2.4 Compatibility of antibody labelling with different clearing methods

Although the tdTomato fluorescence of hUC-MSCs was not detectable in s-DISCO- and ECi-treated thick lung sections, the biodistribution of administered cells can be investigated using cell-specific antibodies. To test the compatibility of each optical clearing method with antibody staining, we aimed to detect the hUC-MSCs with a specific antibody within the lungs. In this instance, we utilised the human origin of the hUC-MSCs and applied an antibody specific for human mitochondria to distinguish the hUC-MSCs from the mouse tissue. Alternatively, antibodies against the tdTomato or FLuc reporters could be applied.

Our image analysis showed that the human mitochondria antibody colocalizes with the tdTomato signal in CUBIC cleared samples confirming the specificity of this antibody to the human hUC-MSCs (Figure 11a). Moreover, we observed that the antibody signal was detected throughout the 500 μm thick sample. Similarly, in the s-DISCO and ECi cleared samples, the antibody permeated the entire tissue (Figure 11b, c).
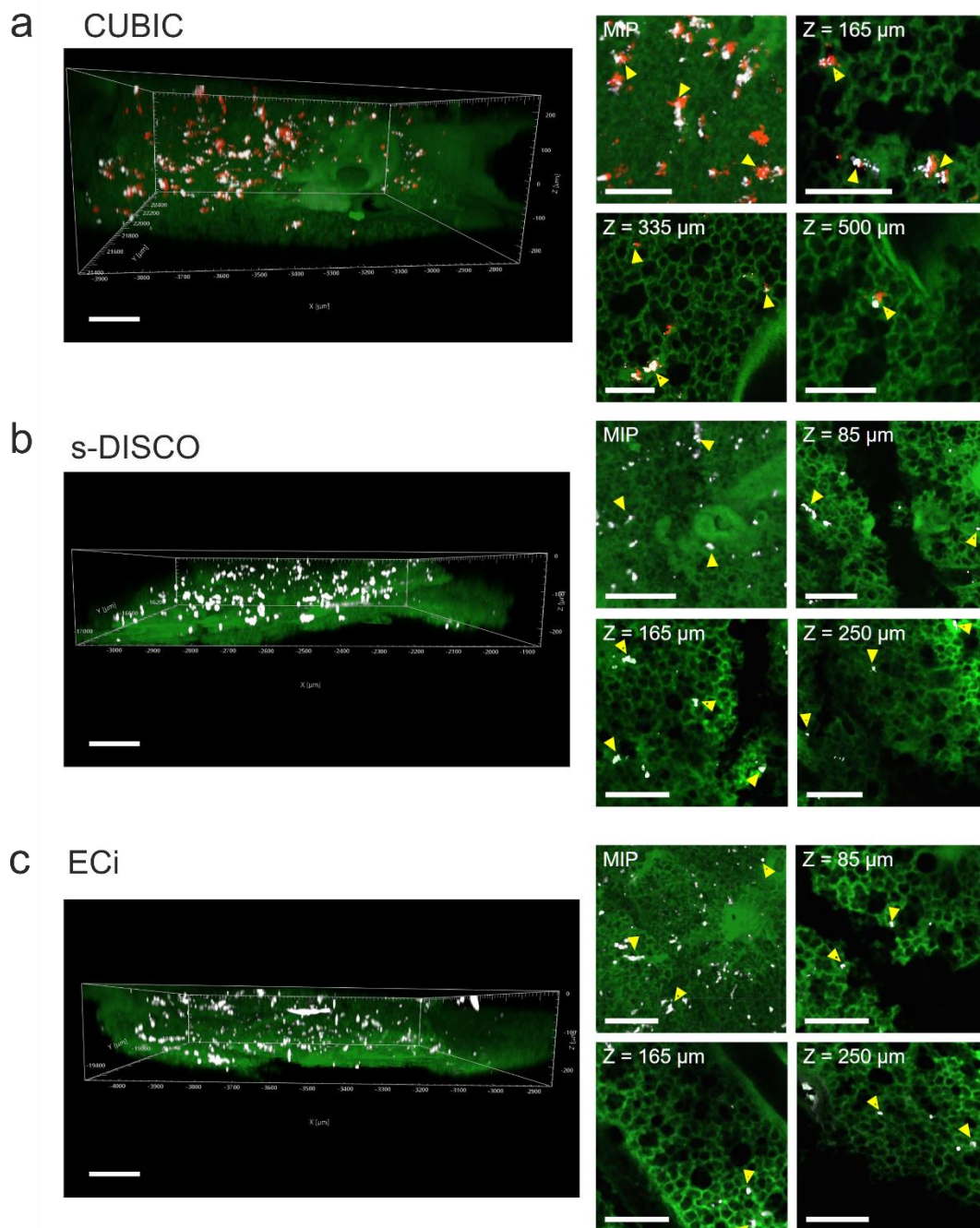
Figure 11. Preservation of immunofluorescence after optical tissue clearing. The human mitochondria antibody (white) was used to stain the tdTomato hUC-MSCs (red) in 500 µm lung sections followed by clearing with either CUBIC, s-DISCO or ECi. The antibody penetrated the entire depth in all samples. a) 3D z-stack of a CUBIC cleared lung section (left). Maximum intensity projection and single slices at different sample depths (right). b) 3D z-stack of an s-DISCO cleared lung section (left). MIP and single slices at different sample depths (right). c) 3D z-stack of an ECi cleared lung section (left), MIP and single slices at different sample depths (right). hUC-MSCs are indicated by arrowheads. Scale bar = 200 µm (left), 150 µm (right).

3.2.5 *In vivo* and ex vivo tracking of administered hUC-MSCs by BLI and optical tissue clearing

To evaluate the biodistribution and fate of hUC-MSCs *in vivo*, the animals were imaged using BLI immediately after IV administration of the cells, and 24 h post injection. A strong signal was detected in the lungs on the administration day but was significantly reduced on day 1 (Figure 12a, b). We dissected whole lung lobes on the day of cell injection and at 24 h post cell administration, and performed CUBIC clearing, as this was the method that allowed the direct detection of the hUC-MSCs. Subsequent confocal imaging of whole lung lobes revealed that the cells distributed throughout the tissue and did not home preferentially to any site as they can be found dispersed within the lung. *Ex vivo* imaging of CUBIC-cleared lungs collected 24 h after cell administration confirmed that most of the cells had been cleared from the lungs as shown by the reduced size of the cell clumps (figure 12c, right). The overall cell distribution remained similar as on the injection day, with the hUC-MSCs localizing evenly throughout the organ (Figure 12c).

Given the compatibility of the CUBIC protocol with immunofluorescence, as a proof of concept, we explored the possibility of using this clearing method to study the interaction of the hUC-MSCs with cells of the mouse lung. The vasculature was labelled with the CD31 endothelial marker. Although the image resolution was not sufficient to demonstrate the localisation of the hUC-MSCS in intra-capillary space we observed that the hUC-MSCs appear to be retained in the pulmonary microvasculature as no cells were detected within large blood vessels (Figure 12d, supplementary videos 1 and 2).

Alternatively, the vasculature can be labelled by injecting Evans Blue IV. In the experiment described previously (Figure 11), the Alexa Fluor® 647 secondary antibody was used, but its spectrum overlaps with Evans Blue. Due to an increase in tissue autofluorescence across all wavelengths, following ECi, we were unable to label the hUC-MSCs utilising the green, red, or near infrared channels. Thus, it was not possible to immunolabel the hUC-MSCs in lungs stained with Evans Blue and cleared by ECi. Nevertheless, thin section analysis of uncleared lungs stained with Evans Blue, by injecting dye IV after cell injection, revealed that hUC-MSCs remained in close contact with the

74

pulmonary vasculature when the lungs were harvested immediately after cell administration (Supplementary figure 4a). In addition, hUC-MSCs blocked the free flow of Evans Blue dye as evidenced by the accumulation of dye around areas where the hUC-MSCs are present. Moreover, the lack of Evans Blue vascular staining in lung regions surrounded by hUC-MSCs suggested that the cells might have formed emboli (39) (Supplementary figure 4b).

Finally, to demonstrate the usefulness of the CUBIC clearing protocol to study immune responses in the lung after hUC-MSC administration, neutrophils were stained with the myeloperoxidase (MPO) marker. A rapid neutrophil infiltration was observed 2 h after IV hUC-MSC injection with decreasing neutrophil levels after 24 h (Figure 12e).
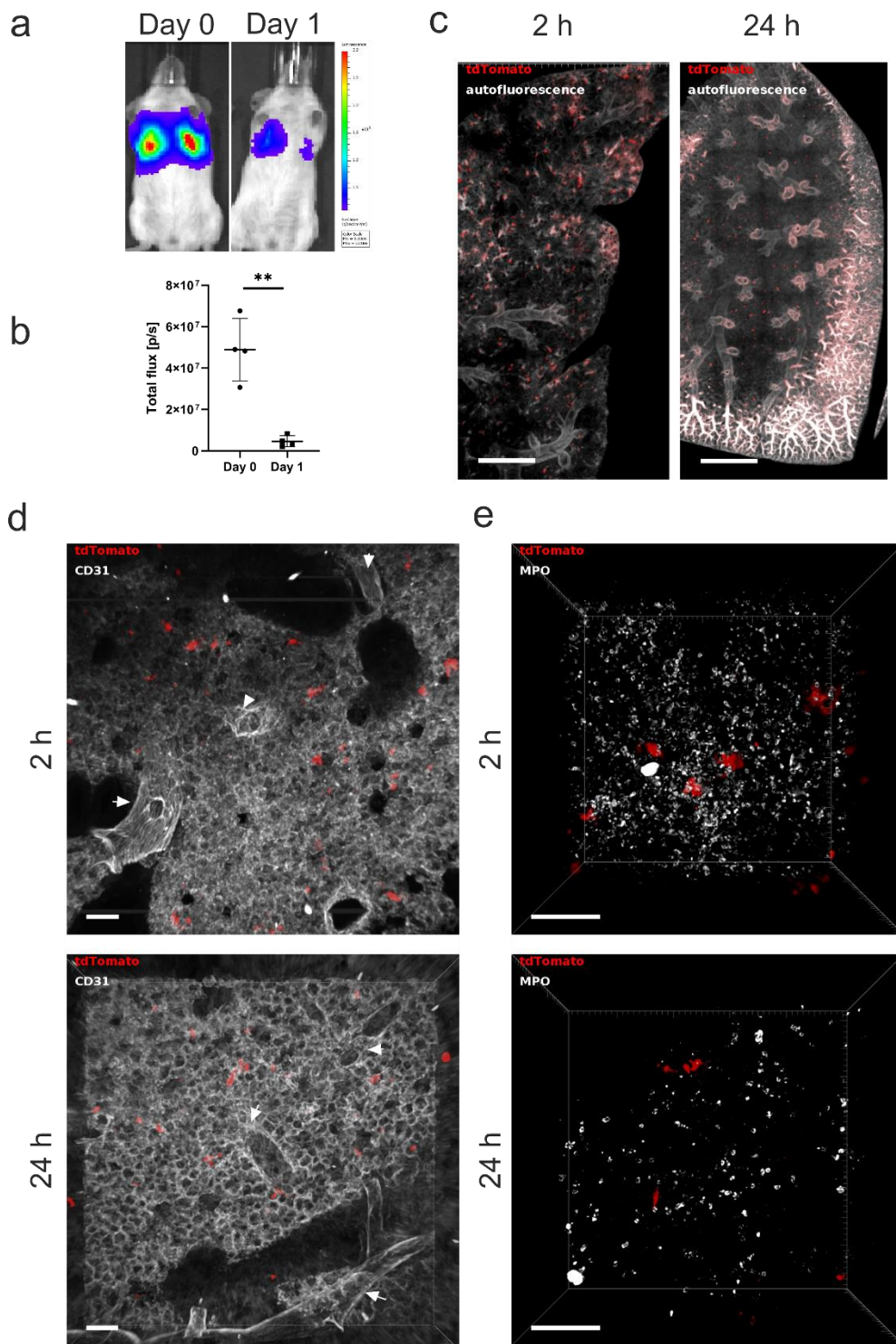
Figure 12. In vivo and ex vivo imaging to detect hUC-MSC distribution for up to 24 h post-administration. a) 2.5 x 10^5 hUC-MSC were injected via the tail vein and the mice were imaged on the administration day (Day 0) and 24 h post cell administration (Day 1). Representative images of the mice as acquired 20 min post subcutaneous administration of D-Luciferin. b) Flux (light output) as a function of time. Data are displayed as mean ± SD from n = 4. Statistical analysis was performed using a paired student T-test. **p < 0.05. c) hUC-MSC biodistribution in whole mouse lung lobes after CUBIC clearing 2 h after cell administration and 24 h post injection. Scale bar = 800 μm. d) CD31

stained 500 µm lung section on the day of administration and 24 h post cell injection. Large vessels are indicated by arrowheads. e) Neutrophil recruitment to the lungs 2 and 24 h after hUC-MSCs administration. MPO = Myeloperoxidase. Scale bar = 100 µm.

In summary, of the three methods compared, the CUBIC protocol proved to be suitable for efficiently clearing the lung specimens without altering the tissue morphology. CUBIC was the only method that preserved tdTomato fluorescence in thick lung sections, allowing for direct visualisation of hUC-MSCs by confocal microscopy. However, CUBIC failed to preserve Evans Blue labelling of the vasculature but showed good antibody compatibility. In contrast, s-DISCO and ECi allowed rapid optical clearing of whole lungs but permanently quenched the fluorescence of tdTomato, while preserving the endothelial Evans Blue signal. Even though no clearing method was perfect for all subsequent imaging applications, by combining the CUBIC clearing method with various staining approaches, we were able to demonstrate that hUC-MSCs seem to be trapped in the lung microvasculature just after injection, potentially blocking blood flow, and that hUC-MSC intravenous administration triggers neutrophil infiltration.

3.3   Discussion

In this work, the CUBIC, s-DISCO and ECi optical tissue clearing protocols were compared with the aim of establishing a suitable approach to study the biodistribution of hUC-MSCs in mouse lungs following systemic cell delivery.

Optical tissue clearing matches the RI of heterogeneous samples and reduces light scattering, enabling the investigation of biological processes in a whole organ context. Broadly, clearing methods can be classified into water-based (hydrophilic) and solvent-based (hydrophobic) methods depending on the chemistry used (172). Selecting a clearing protocol depends on parameters such as the size of the sample, tissue composition and the intended goal of the experiment.

First, it is relevant to characterize the effect of the clearing method on the tissue of interest. When applied to lung tissue, CUBIC is the superior method regarding tissue transparency albeit taking 5 days to complete. In contrast, both solvent-based methods cleared the samples within hours but resulted in

a transparency below 50%. Changes in sample size occurred as expected: hydrophilic methods led to sample expansion, which might be an advantage when interested in increasing imaging resolution; solvent-based protocols resulted in sample shrinkage, which can be advantageous when imaging large samples (230).

Another relevant consideration when selecting a clearing protocol is whether there is a need to preserve fluorescent proteins. In this study, the red fluorescent protein tdTomato was used as a molecular label for the hUC-MSCs. tdTomato was immediately quenched after s-DISCO and ECi clearing of thick lung sections, rendering these protocols unsuitable for direct visualization of fluorescently labelled cells, while CUBIC preserved the fluorescence of tdTomato.

Fluorescent proteins are stabilized by water molecules and thus, dehydration results in their denaturation and subsequent loss of fluorescence (242). To overcome this, the use of milder dehydrating chemicals such as tetrahydrofuran (THF) in the 3DISCO protocol (243), tert-butanol and diphenyl ether in the uDISCO protocol (176), and 1-propanol in the second generation ECi protocol have been used successfully allowing GFP preservation for days to months (237). Given these reports, we used 1-propanol as the dehydration agent for both s-DISCO and ECi protocols in the hope of preserving tdTomato. Nevertheless, we were not able to detect tdTomato fluorescence. Interestingly, Glaser and colleagues acquired a 3D image of a whole mouse lung cleared with ECi via autofluorescence at 561 nm, which is consistent with our observation that tissue autofluorescence at this wavelength is increased after immersion in ECi (244). Moreover, the compatibility of a variety of fluorescent probes with ECi was tested and tdTomato fluorescence was reported to be poor after clearing (237).

In this study, the s-DISCO protocol was chosen given that it suggests that adding the antioxidant propyl gallate to DBE prevents the formation of peroxides and aldehydes, which are partly responsible for fluorescence decline, and makes it possible to preserve tdTomato for up to a year. This protocol is complex and requires specific expertise to purify reagents with

explosive properties to eliminate all peroxide and aldehyde contents before adding the propyl gallate to prevent their regeneration (179). We aimed to test whether simplifying the protocol to make it more accessible to the wider research community, by preventing peroxide formation in DBE, would suffice to preserve the fluorescence of tdTomato. Nevertheless, we did not observe fluorescence preservation after the modified s-DISCO clearing, indicating that this approach is not sufficient to preserve fluorescent proteins and suggests that pure chemicals might be necessary throughout the entire clearing protocol (179).

Interestingly, we observed that the fluorescence of tdTomato was preserved immediately after the completion of the modified s-DISCO and ECi protocols by decreasing the dehydration time when clearing 100 μm thin lung sections. This finding might explain the variability in the results between users of the same protocols for different applications and samples (245). Moreover, it indicates that optimizing the duration of the dehydration steps might be necessary when implementing a solvent-based optical tissue clearing method where fluorescent proteins are involved. Decreasing the dehydration time might result in protein-based fluorescence preservation but it would come at a cost regarding sample transparency. Moreover, dehydration is not the only factor that affects tdTomato as evidenced by the preservation of fluorescence upon storage in ECi, but not in DBE, indicating that the RI matching solvent also plays a critical role in fluorescence quenching.

Temperature and pH have also been proven to play an important part in fluorescence retention, with alkaline pH and 4°C being the optimal parameters that allow fluorescent protein preservation. The studies that showed this were done specifically to preserve GFP fluorescence (173,243,246). Although we followed these recommendations, we failed to visualize tdTomato fluorescence.

Preservation of other fluorescent compounds, such as synthetic organic dyes, is another consideration when selecting a tissue clearing method for a particular application. To study hUC-MSC distribution with spatial landmarks in the 3D lung context, the vasculature was labelled with Evans Blue. CUBIC

washed away the dye, while s-DISCO and ECi preserved Evans Blue fluorescence.

The field of optical tissue clearing is moving at a fast pace with new protocols becoming available often. Here, we did not find a single protocol that allowed us to preserve the fluorescence of tdTomato, stain the vasculature and perform immunostaining simultaneously highlighting the challenges of establishing an optical tissue clearing method for a new application. Alternative protocols that could be tested in the future include Ce3D, OPTIClear, and MACS (171,247,248). The Ce3D protocol has been tested for lung tissue and is compatible with immunofluorescent staining of immune cells while preserving fluorescence of reporter proteins (171). OPTIClear preserves fluorescence proteins, is compatible with lipophilic labels and most fluorescent dyes. Although this method decreases the brightness of some dyes, is incompatible with some primary antibodies and long term storage in the clearing solutions decreases fluorescence, it might be explored for the purpose of cell tracking in the lungs (247). Finally, the MXDA-based Aqueous Clearing System (MACS) has also been validated for lung tissue and is compatible with fluorescent proteins as well as with lipophilic dyes that have been used to stain vascular structures, and antibody labelling, making it a promising approach (248).

In summary, CUBIC is the only protocol that preserved tdTomato but it resulted in Evans Blue washing out of the sample. The opposite occurred when using a modified s-DISCO or ECi, as tdTomato was quenched, but Evans Blue was preserved. These results reflect the challenges of optimizing a clearing method for a specific application. Nevertheless, using immunofluorescence for the endothelial marker CD31 to label the vasculature in CUBIC-cleared lung sections indicated that the hUC-MSCs localise within the micro vessels and do not seem to migrate to the parenchyma after 24 h.

Finally, we briefly explored the possibility of using CUBIC to study the immune response in the lung to the administration of hUC-MSCs. A rapid infiltration of neutrophils was observed 2 h post cell injection with the number of these cells decreasing after 24 h. This proof of principle paves the way for studying other immune cell populations in thick lung sections in the context of cell therapies.

3.4   Conclusions

We compared three optical tissue clearing methods previously described in the literature to track the lung biodistribution of hUC-MSCs labelled with the fluorescent protein tdTomato. Direct detection of the tdTomato cells was only possible using the CUBIC clearing protocol, which although time consuming, results in highly transparent lungs and showed good antibody compatibility and penetration. Moreover, using immunofluorescent staining allows the study of the interaction of the hUC-MSCs with cells in the host's lung. Using 3D imaging of CUBIC cleared lungs we showed that hUC-MSCs were trapped in the pulmonary vasculature and are mostly cleared within the first 24 h after IV injection.

Chapter 4. Investigating the fate of hUC-MSCs in the lung and their effect in immune cell populations

4 Introduction

In the third chapter, we showed that after IV injection, most hUC-MSCs remain within the lung vasculature and die within 24 h. Despite the first-pass effect, several studies suggest that exogenous MSCs can ameliorate injury in a variety of animal models such as the heart (26), eye (249), kidney (250), bone (22), cartilage (251), liver (252), etc.

Although the mechanisms are not fully elucidated, it appears that at least some of the therapeutic effects of MSCs are mediated by the immune system (53). However, it is unclear what initial effect the MSCs have on the immune-cell populations in the lung.

To provide an early line of defence against infections in tissues, the first type of immune cells that respond to invading pathogens or foreign materials are the cells of the innate immune system (44). Bone marrow-derived myeloid cells consist of a heterogeneous population comprising macrophages, monocytes, dendritic cells (DCs) and granulocytes (253). Despite each subset having specialized functions based on their environment, all myeloid cells play a role in the phagocytosis of foreign materials and in the secretion of cytokines and chemokines to induce an immune response (254).

Granulocytes (mast cells, basophils, eosinophils, and neutrophils) are the first cells recruited to local sites upon foreign invasion, followed by monocytes and macrophages (255). Among granulocytes, neutrophils are the most abundant (256). These non-proliferative cells are known for their pathogen-clearing mechanisms involving reactive oxygen species generation, antimicrobial protein degranulation, and neutrophil extracellular traps (NETs) formation (257,258). After MSC IV administration, neutrophils show an enhanced phagocytic capacity that aided bacterial clearance in a murine sepsis model (259).

Monocytes are precursor cells that give rise to DCs and macrophages. Their mobility gives them a unique role in the mononuclear phagocyte system. In

contrast to the limited migration potential of terminally differentiated DCs and macrophages, monocytes are rapidly mobilized upon challenge and can access any location within the body catering to its needs (260). In the context of cell therapies, an IV injection of hUC-MSCs into mice showed that monocytes mediate the rapid clearance of the cells by phagocytosis (116). Moreover, phagocytosis of the administered cells in the lung results in monocyte reprogramming toward an anti-inflammatory activation state (116).

Tissue macrophages play various homeostatic roles such as tissue remodelling and repair, clearing of senescent cells, as well as induction and resolution of the inflammatory response (260). In addition, macrophages engage with T and B lymphocytes and participate in the induction of adaptive immunity (261). The IV infusion of MSCs in mice leads to an inflammatory response accompanied by increased numbers of macrophages in the lungs shortly after the cells home to this organ (262). Moreover, the MSCs increase the number of anti-inflammatory macrophages and decrease the inflammatory macrophages *in vivo* (263), affecting disease outcomes via macrophage polarization (264).

Macrophages can further be categorized based on their location. In the lung, resident alveolar macrophages are maintained by local proliferation (48) and perform tissue-specific roles such as surfactant clearance (265). MSCs reduced the severity of lung injury in an *E. coli* pneumonia model and modulated alveolar macrophage polarization *in vivo* (266). Interstitial macrophages mature in the lung after the recruitment of precursors from the blood (260). Their localization within the lung remains unclear. Studies have shown their presence in the parenchyma (267) and the bronchial interstitium (268). Their functions include phagocytosis of foreign invaders, antigen presentation and immune modulation (269).

Some studies have been done to understand the interactions between infused MSCs and specific immune cell populations *in vivo* (116,270,271) but a comprehensive analysis on the impact on innate cells is lacking. To investigate the fate of hUC-MSCs in the lung and their effect on innate immune cell populations, we administered cells into immunocompetent naïve mice. Then,

we measured the changes in the proportion of myeloid cells and their distribution at two different time points: 2 hours and 24 hours. These time points were selected because at 2 hours following cell injection, most cells remain viable, while by 24 hours, most of the hUC-MSCs have been cleared.

The specific goals of this study include:

1.   Implementing a gating strategy to identify myeloid cells subtypes and their polarization state.

2.   Studying the effect of hUC-MSCs on the distribution of myeloid cells in the lungs

3.   Studying the effect of hUC-MSCs on the proportion, distribution and polarization of infiltrating granulocytes within the lung.

4.   Evaluating the effect of hUC-MSC on neutrophil extracellular trap formation

5.   Studying the effect of hUC-MSCs on the proportion, distribution and polarization of infiltrating monocytes and macrophages within the lung.

6.   Assessing the effect of hUC-MSCs on the proportion and polarization of lung macrophage subpopulations.

4.1 Methods

4.1.1 Cell preparation

Primary human umbilical cord-derived mesenchymal stromal cells (hUC-MSCs) were collected from consenting donors at the National Health Service Blood and Transplant (NHSBT, UK) and obtained at passage 3.

The hUC-MSCs were transduced in the presence of 6 µg/ml DEAE-Dextran with a lentiviral vector encoding luc2 firefly luciferase (FLuc) reporter under the constitutive elongation factor 1-α (EF1α) promoter and the tdTomato fluorescent protein downstream of the bioluminescence reporter via an IRES linker. pCDH-EF1-Luc2-P2A-tdTomato was a gift from Kazuhiro Oka (Addgene plasmid # 72486; http://n2t.net/addgene:72486; RRID:Addgene 72486). To obtain a >98% transduced population, the cells were sorted based on tdTomato fluorescence (BD FACS Aria). The cells were cultured in α-MEM supplemented with 10% FBS and incubated at 37°C, 5% CO_2. When confluent, cells were washed with PBS and incubated with 1% trypsin at 37°C for 3 min. Subsequently, culture medium was added and the cell suspension was transferred to a 15 ml conical tube and centrifuged at 300G for 3 minutes. The supernatant was discarded and the cell pellet resuspended in an adequate volume of medium for passaging. Prior to re-plating, 10 µl of cell suspension was transferred into a haemocytometer and cells were counted. All procedures were performed under sterile conditions.

4.1.2 Animal studies

All experiments were carried out under a licence granted under the UK Animals Act 1986 and were approved by the ethics committee of the University of Liverpool Animal Welfare and Ethics Review Board (AWERB). Eight to ten-week-old female albino mice (C57BL/6) (B6N-TyrC-Brd/BrdCrCrl, originally purchased from the Jackson Lab) were housed in individually ventilated cages under a 12 h light/dark cycle, with ad libitum access to water and food.

4.1.3 Dissociation of lung tissue

Mice received an IV injection of 2.5 x 10^5 untransduced hUC-MSCs or PBS (100 µL) under anaesthesia with isoflurane. 2 or 24 h post injection, the animals were culled by cervical dislocation. The lungs were removed *en bloc*. The large airways were dissected from the peripheral lung tissue and each lung lobe was separated. The lung lobes were cut into small pieces with scissors, transferred into C-tubes (Miltenyi, Auburn, CA), and processed in digestion buffer (1 mg/ml of Collagenase D and 80 U/ml DNase I, both from Roche, in DMEM) and a GentleMACS dissociator (Miltenyi), according to the manufacturer's instructions. The lung homogenates were strained through a 70 mm nylon mesh to obtain single-cell suspensions. Red blood cells were lysed using ammonium-chloride-potassium (ACK) lysis buffer (Gibco, A1049201). The resultant cells were counted using an automated cell counter (TC10, BioRad).

4.1.4 Flow cytometry

One million cells suspended in 90 µl of staining buffer (eBiosciences, 00-4222-26) were incubated with 10 µl FcBlock (Miltenyi Biotech, 130-092-575) to reduce nonspecific antibody binding. The cells were stained with a mixture of fluorochrome-conjugated antibodies (see Table 4) for a list of antibodies, clones, and fluorochromes). Data were acquired on a BD CANTO II flow cytometer using BD FACSDiva software (BD Biosciences; see supplementary figure 5 Supplementary Figure for instrument configuration), and compensation and data analyses were performed using the DIVA software). The gating strategy followed was adapted from Misharin, A. *et al.* 2013 (272). See results for the gating strategy used to identify cell populations (Figure 13 and Figure 14). The results of the flow cytometric analysis are displayed as the percentage of the total cells (percentage of cells %).

Table 4. Antibodies used for flow cytometry. All antibodies were purchased from Miltenyi Biotec.

Conjugated antibody	Host/ Isotype	Clone	Dilution	Cat. No
CD45 FITC	rat IgG2bκ	30F11	1:50	130-116-500
CD11b VIOBLUE	Rat IgG2b, k	M1/70.15.11.5	1:50	130-113-238
Cd11c APC-Vio770	Hamster IgG	N418	1:50	130-122-016
CD64 APC	Human IgG1	REA286	1:50	130-126-950
CD24 PE-Vio770	rat IgG2bκ	M1/69	1:10	130-102-736
MHCII PE	rat IgG2bκ	M5/114.15.2	1:10	130-102-186
CD71 PERCPVIO700	Human IgG1	REA627	1:50	130-128-620
Siglec-F PE-Vio770	Human IgG1	REA798	1:50	130-112-334
CD103	Hamster IgG	2E7	1:50	130-121-442
Ly6G	Human igG1	REA526	1:50	130-120-803

4.1.5 Retrograde perfusion fixation

2 or 24 h after IV administration of FLuc+ tdTomato hUC-MSCs, the mice received an intraperitoneal overdose of pentobarbital (Pentoject, 100 µl) followed by cannulation of the abdominal aorta, snipping of the vena cava and flushing of Heparin/PBS (5 IU/ml) with a manual pump at a constant pressure of 200 mbar (Supplementary figure 1) for 6 min to remove all blood cells, followed by 6 min perfusion with 4% w/v paraformaldehyde (PFA) to fix the whole animal. The total volume of each solution used per animal was 40 ml.

The trachea was tied tightly with a surgical suture before opening the thoracic cavity for lung dissection. Finally, the lungs were post-fixed in 4% PFA overnight at 4°C.

4.1.6 Immunofluorescence

Before staining, the lungs were cleared using the CUBIC protocol as described in chapter 2. The cleared lungs were sucrose protected and cryo-embedded in optimal cutting temperature (OCT) medium before sectioning 30 µm thick sections using a cryostat (Thermo Scientific, Microm HM505E) at -20°C and stored at -80°C.

All sections were washed with PBS 3x for 5 min. Tissues were incubated with primary antibodies for 2 h at RT or O/N at 4°C. The primary antibody was washed with PBS, and the secondary antibodies and DAPI were added. Incubation was done at RT for 1 h. After a final washing step, the sections were mounted in fluorescence mounting media (Dako, S3023). All antibodies and dilutions used can be found in *Table 5*.

Table 5. Antibodies used for immunofluorescence.

	Host	Clone	Isotype	Dilution	T°/time	Manufacturer
F4/80 - FITC	Human	REA126	igG1	1:50	RT / 2 h	Miltenyi Biotec (130-117-509)
CD16/32	Human	REA377	igG1	1:10	RT / 2 h	Miltenyi Biotec (130-107-066)
Ly6C	Rat	HK1.4	IgG2c, k	1:200	4 / ON	Biolegend (128001)
Myeloperoxidase	Goat	Polyclonal	igG	1:100	4 / ON	R&D Systems (AF3667-SP)
HDAC2	Rabbit	Polyclonal	igG	1:250	RT / 2 h	Sigma-Aldrich (HPA011727)
CD11b - APC	Rat	M1/70.15.11.5	IgG2b, k	1:50	RT / 2 h	Miltenyi Biotec (130-113-231)
Ly6G - APC	Human	REA526	igG1	1:50	RT / 2 h	Miltenyi Biotec (130-120-803)
CD163	Rabbit	Polyclonal	igG	1:100	RT / 2 h	Invitrogen (PA5-78961)
Alexa Fluor® 750 donkey anti-rat	Donkey	Polyclonal	IgG	1:200	RT / 1 h	Abcam (ab175750)
Alexa Fluor® 647 goat anti-rabbit	Goat	Polyclonal	igG	1:1000	RT / 1 h	Invitrogen (A-212465)
Alexa Fluor® 647 goat anti-hamster	Goat	Polyclonal	igG	1:1000	RT / 1 h	Invitrogen (A-21451)
Alexa Fluor® 633 goat anti-rat	Goat	Polyclonal	igG	1:1000	RT / 1 h	Invitrogen (A-21094)

4.1.7 Imaging

Confocal microscopy images were acquired using a Leica DMi8 with Andor Dragonfly spinning disk, coupled to an EMCCD camera using a 40x/1.3 oil objective. Z-stacks were captured using the 488, 561 and 637 nm laser lines. The emission filters used were 525/50, 600/50 and 700/75. Maximum intensity projections, three-dimensional reconstructions and image analysis were done using the IMARIS (Bitplane) software package.

Cell counting with IMARIS was performed by opening *Z*-stacks in their native format, as they are automatically reconstructed into a multi-channel 3D model, which eliminates the need for image pre-processing. To designate individual cells of interest, the Spots creation tool was used. In the Spots creation wizard, the source channel corresponding to the staining of interest was selected. Background subtraction was used to separate the cell from the background. The auto-threshold value was utilized during background subtraction. The generated spots were a direct map of the intensity distribution of the immunostaining of interest as detected by Imaris. Adjustments to the Spots to create an accurate representation of the staining were made using the manual spot creation/deletion tool.

4.1.8 Statistics

Data were analysed using GraphPad Prism for Windows version 8.4.2 (GraphPad Software, Inc., San Diego, CA). Values are presented as means ± standard deviations. Comparisons between animal groups were performed using the Kruskal-Wallis test with multiple comparisons. $P < 0.05$ was considered statistically significant. The number of replicates included in the analyses, are given in the figure legends.

4.2 Results

4.2.1 Implementation of gating strategy to identify myeloid cell subtypes and their polarization state

To identify immune cells in the lung in response to cell therapy, we first established a flow cytometric gating strategy using lung cell suspensions from naïve animals.

After excluding debris and doublets, the pan-hematopoietic marker CD45 was used to identify leukocytes. The markers used to identify specific populations can be found in *Table* 6.

Table 6.Surface markers used to identify immune cells by flow cytometry.

Cell type	Phenotype	Refs
Granulocytes	Cd11c$^-$ CD24^{hi}	(272)
Neutrophils	Siglec F$^-$ CD11b^{hi} CD103$^-$ Ly6G^{hi}	(272)
Monocyte/M0 macrophages	CD11b^{hi} MHC II$^{+/-}$ CD64$^{+/-}$	(272)
Alveolar macrophages	Cd11b$^-$ CD11c^{hi} CD64$^+$	(265)
Interstitial macrophages	MHC II$^+$ CD11b$^+$ CD64$^+$ CD24$^-$	(273)

The strategy was used to identify all myeloid cells, and the specific sub-types. The strategy for granulocytes, polarised resident lung macrophages and polarised interstitial macrophages is shown in Figure 13a; the strategy for polarised infiltrating monocytes/macrophages is shown in Figure 13b; and the strategy for neutrophils is shown in Figure 14. CD64 (274) and CD71 (275,276) were used as polarization markers of pro- and anti-inflammatory phenotypes, respectively.
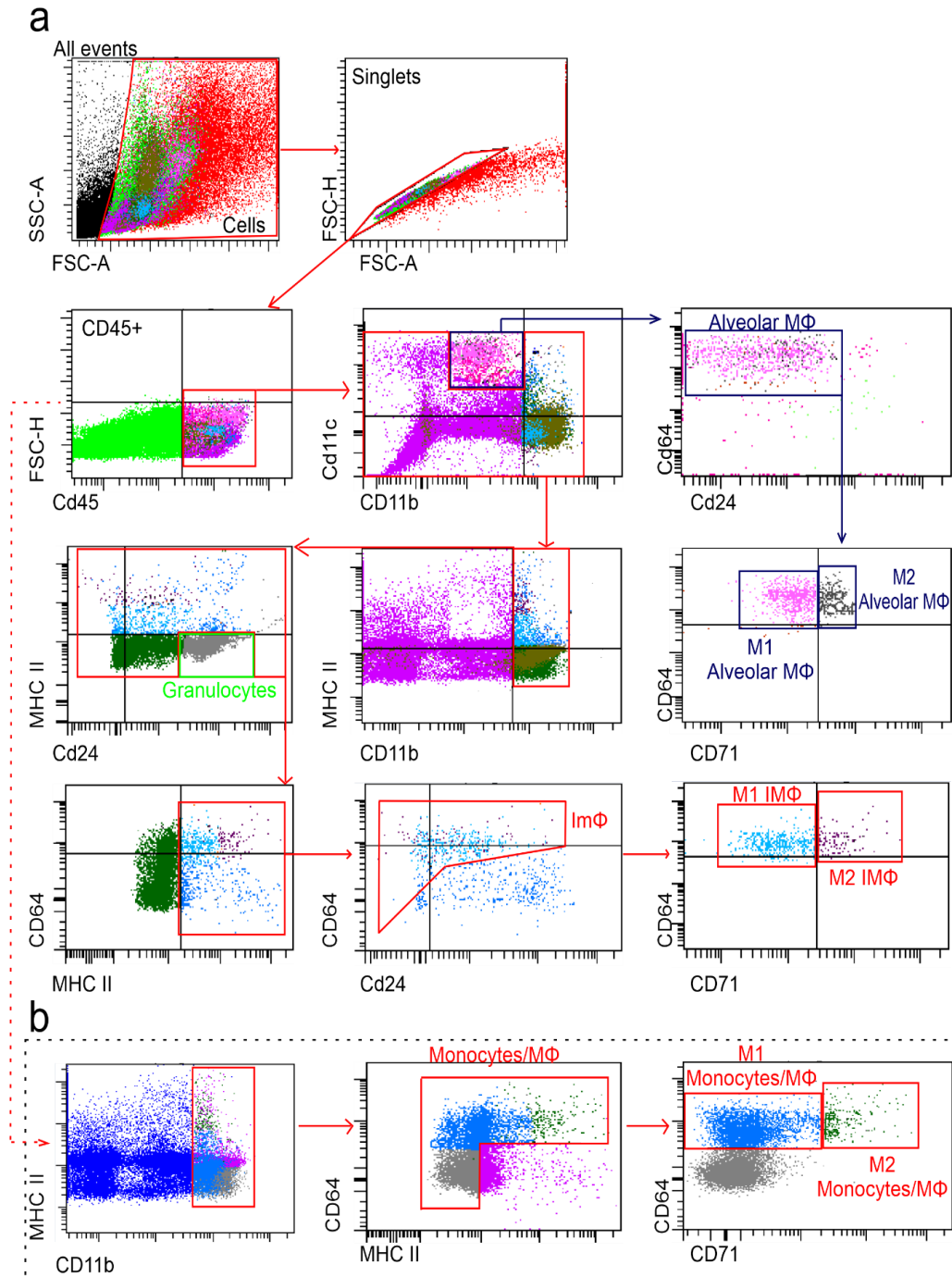
Figure 13. Gating strategy used to identify immune-cell subsets in the mouse lung after IV administration of hUC-MSCs or saline. After enzymatic and mechanical digestion of mouse lungs, debris and doublets were excluded. Leukocytes were identified by CD45 staining. a) To find specific populations, a sequential gating strategy was used: alveolar macrophages (MΦ) (CD11b⁻ CD11cʰⁱ), granulocytes (CD11c⁻ CD24ʰⁱ), interstitial macrophages (CD11b⁺ MHC II⁺ CD64⁺ CD24⁻). The polarization status toward a pro- or anti-inflammatory phenotype was assessed by the expression of CD64 and CD71, respectively. b) A parallel gating strategy was used to identify monocytes: monocytes/M0 MΦ (CD11bʰⁱ MHC II⁺/⁻ CD64⁺/⁻). To identify classically- and alternatively-activated cell types the CD64 (M1 marker) and CD71 (M2 marker) were used.
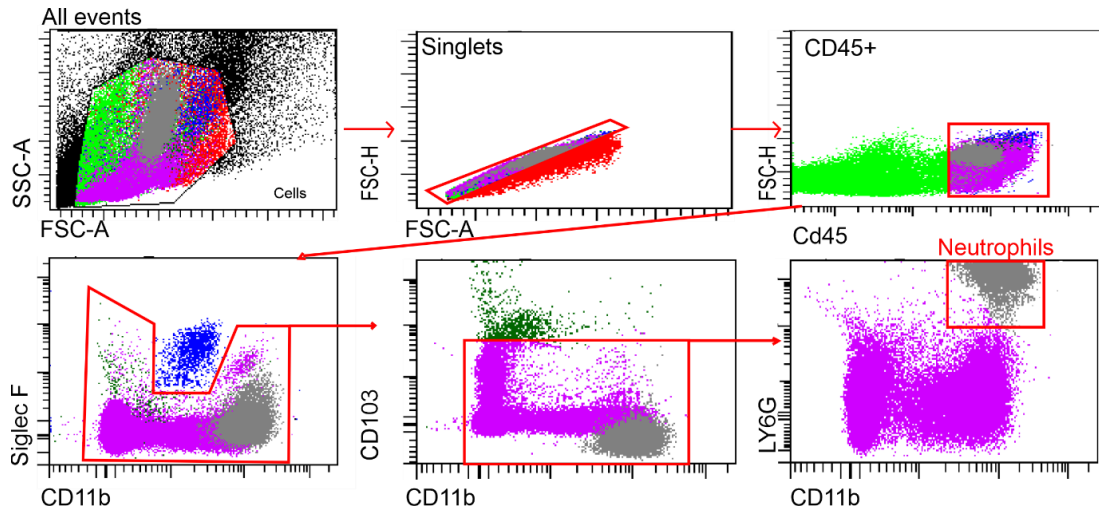
Figure 14. Gating strategy used to identify neutrophils in the mouse lung after IV injection of hUC-MSCs or saline. Lung enzymatic and mechanic digestion was performed. Debris and doublets were excluded. CD45 staining was used to identify leukocytes. Neutrophils were gated as Siglec F$^-$ CD11b^{hi} CD103$^-$ Ly6G^{hi}.

4.2.2 Effect of hUC-MSCs on the distribution of myeloid cells in the lungs

To investigate changes in biodistribution of the myeloid cells within the lung after hUC-MSC administration, the lungs of mice that received FLuc TdTomato-expressing hUC-MSCs were fixed and used to prepare frozen sections for histology.

Using the CD11b pan-myeloid marker (277), confocal microscopy revealed that 2 h post hUC-MSC IV administration, there was an increase in myeloid cells. These cells persisted in the lungs up to 24 h. Moreover, the cells accumulated in close proximity to the hUC-MSCs clusters and fragments (Figure 15a), suggesting that these cells might be phagocytosing the hUC-MSCs. Quantification of myeloid cells confirmed a sharp increase in these cells at 2 h that was sustained at 24 h (Figure 15b).
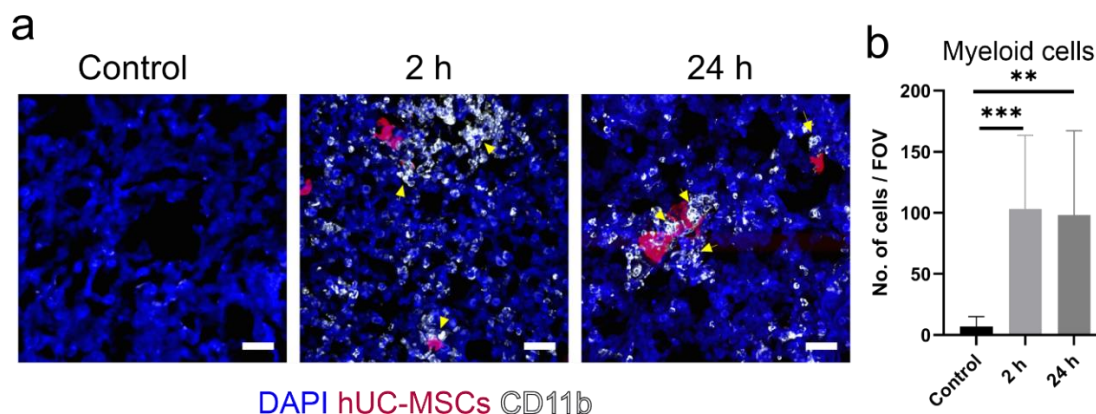
*Figure 15. CD11b⁺ myeloid cells infiltrated into the lungs after IV administration of hUC-MSCs. a) Representative maximum intensity projection (MIP) confocal microscopy images showed CD11b⁺ cells (white) infiltrated into the lungs in comparison with control animals that received saline. CD11b⁺ cells clustered around the hUC-MSCs (red) in the lungs 2 and 24 h after cell injection (yellow arrows). Scale bar = 30 μm. b) Immunofluorescence quantification of CD11b⁺ cells. Kruskal-Wallis test with multiple comparisons. n=9; P<0.005 **; P<0.0005 ***.*

Immunofluorescence analysis and quantification showed that myeloid cells infiltrate the lungs after IV injection of hUC-MSCs.

4.2.3 Effect of hUC-MSCs on the proportion, distribution and polarization of infiltrating granulocytes within the lung

To understand what type of myeloid cells had accumulated in the lung, flow cytometry was undertaken to determine the proportion of innate immune cell sub-types. Mice received untransduced hUC-MSCs IV and their lungs were dissociated for flow analysis. To study the biodistribution in the lung, a different cohort of mice was used to inject FLuc TdTomato-expressing hUC-MSCs. Their lungs were fixed and used to prepare frozen section for immunofluorescence.

Flow cytometric analysis revealed that the proportion of granulocytes increased approximately twofold from baseline 2 h post hUC-MSC administration. The number of these cells decreased after 24 h, but remained 1.7x higher than control (Figure 16a, left). Particularly, neutrophils showed an approximate 4.5x increase at 2 h with the number of these cells returning to baseline after 24 h (Figure 16a, right).

The granulocyte/monocyte marker MPO (278,279) was used for immunofluorescence staining. MPO positive cells localized in the vicinity of the hUC-MSC clusters as well as in areas were cell debris was observed (Figure 16b), potentially indicating an active role of these cells in the clearance of the exogenously administered human cells. Quantification of the fluorescence images showed an approximate threefold increase in MPO expressing cells at 2 h, with a decline back to control levels at 24 h (Figure 16c).

To reliably identify neutrophils by immunostaining, we used the MPO surface marker in combination with Ly6G, recognized as a marker that is highly expressed by neutrophils (280). We observed that double-labelled neutrophils localized to the vicinity of the hUC-MSCs at 2 h. After 24 h, cells expressing only Ly6G, which might be monocytes or other granulocytes, were observed distributed evenly throughout the lung (Figure 16d). Their quantification confirmed that, as seen by flow cytometry, these cells infiltrated into the lungs at 2 h and returned to baseline levels at 24 h (Figure 16e).

Together, these data showed that granulocytes, particularly neutrophils, accumulated in the lung in response to hUC-MSC IV administration at the 2 h time point. After 24 h, the number of these cells decreased.
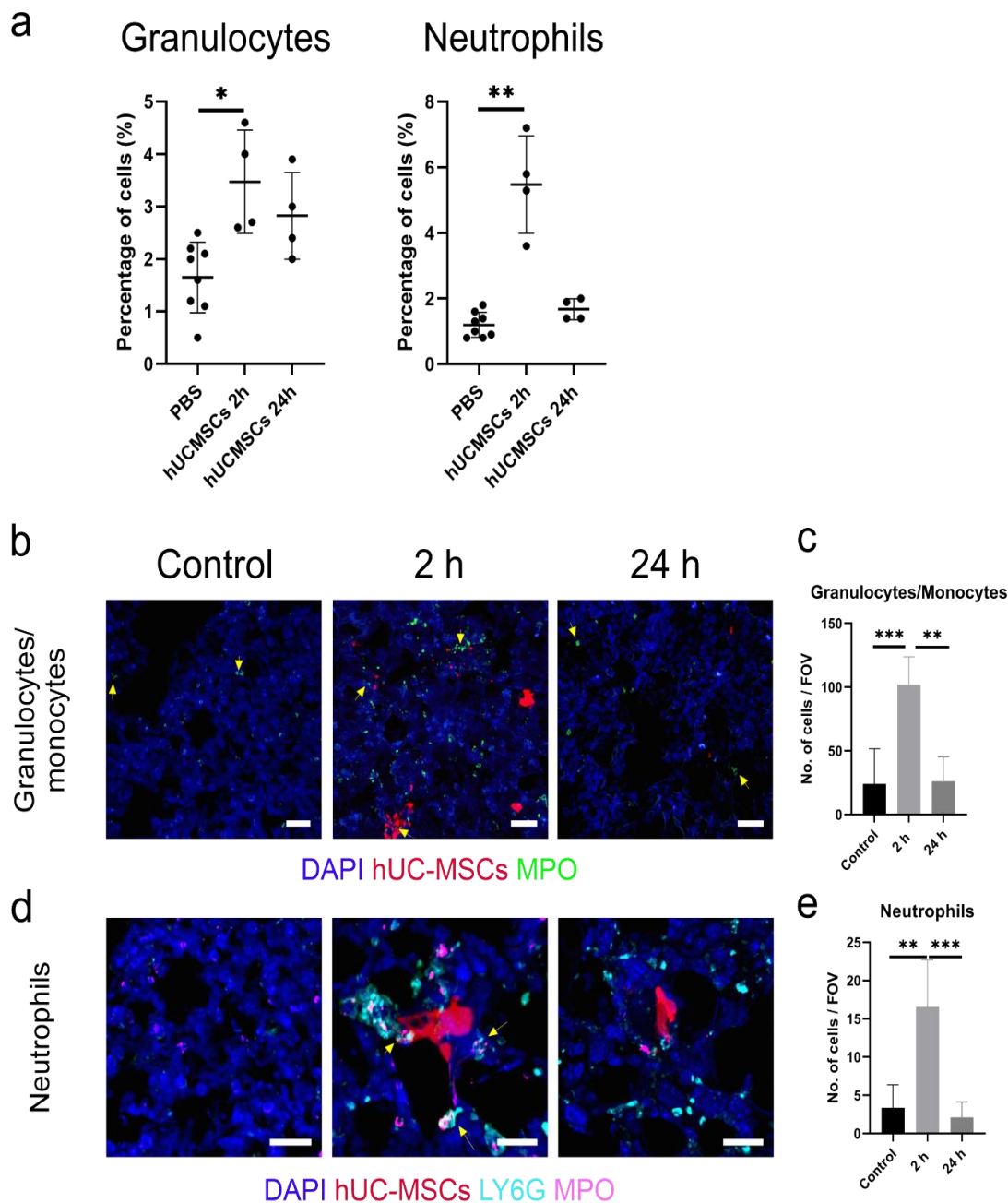
*Figure 16. Granulocytes are recruited to the lungs rapidly after hUC-MSC IV infusion. a) Flow cytometry showed that Cd11c- CD24^{hi} granulocytes and Siglec F$^-$ CD11b^{hi} CD103$^-$ Ly6G^{hi} neutrophils increased 2 h after hUC-MSC injection and decreased at the 24 h time point. Percentage of total cells is displayed in the y-axis. Kruskal-Wallis test with multiple comparisons; control n=8, hUC-MSC group n=4. P<0.05 *; P<0.005 **. b) MPO$^+$ cells (green) clustered around the hUC-MSCs (red) in the lungs 2 h after cell injection (yellow arrows) and their levels decreased at 24 h. Scale bar = 30 µm. c) Immunofluorescence quantification of MPO$^+$ cells. Kruskal-Wallis test with multiple comparisons. n=9. P<0.005 **; P<0.0005 ***. d) Ly6G + MPO (magenta + cyan) neutrophils surrounded the hUC-MSCs (red) in the lungs 2 h after cell injection (yellow arrows). 24 h later, Ly6G cells were still present in the lung. e) Immunofluorescence quantification of MPO + LY6G neutrophils. Kruskal-Wallis test with multiple comparisons. n=9. P<0.005 **; P<0.0005 ***.*

4.2.4 Effect of hUC-MSC on neutrophil extracellular trap formation

Given the high influx of neutrophils into the lung after IV injection of hUC-MSCs, we questioned whether NETs formed as a consequence. We stained frozen lung sections of mice that received FLuc TdTomato-expressing hUC-MSCs for Histone deacetylase 2 (HDAC2), DAPI and MPO, which in combination are common indicators of NET formation (281).

Although an increase in HDAC2 was observed at both time points, the characteristic elongated NET structures where not observed (Figure 17). We observed that HDAC2 expression colocalizes with the hUC-MSCs. Given the body's homeostatic mechanisms, it is unlikely that the DNA of the dying cells would have been exposed. Thus, we speculate that the exposed DNA observed in the tissue environment might have been induced by sample processing leading to the observation of HDAC2 in the lung sections. Thus, NET formation is likely not induced by the administration of hUC-MSCs.
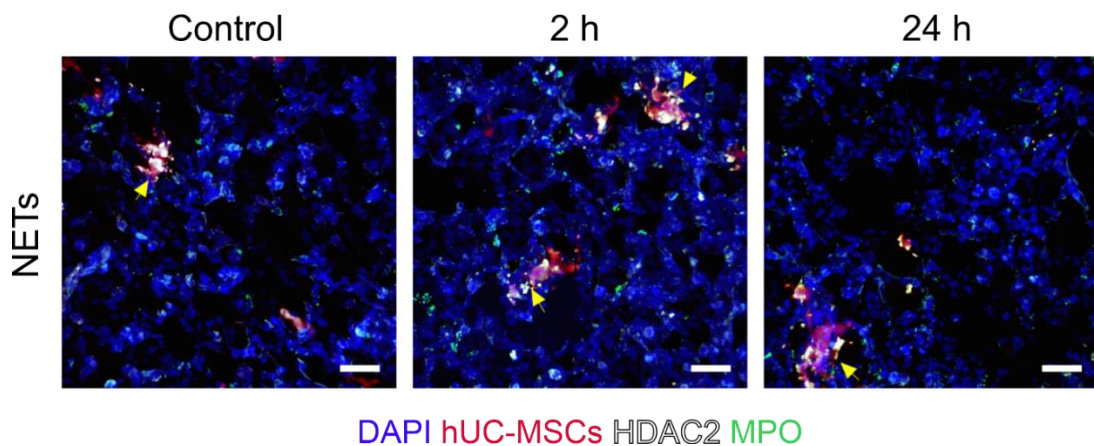
Figure 17. Neutrophil extracellular traps are not observed in the lungs of mice at any timepoint after hUC-MSC IV infusion. hUC-MSCs (red), MPO (green), HDAC II (white). Scale bar = 30 µm.

4.2.5 Effect of hUC-MSCs on the proportion, distribution and polarization of infiltrating monocytes and macrophages within the lung

To determine how hUC-MSCs affected the quantity, localization, and phenotype of infiltrating macrophages and monocytes in the mouse lung we performed flow cytometric analysis and immunofluorescence after injecting untransduced or reporter hUC-MSCs, respectively. Monocytes and macrophages express similar surface molecules. The selection of markers used in our panel, made it difficult to differentiate between these cell populations, thus they were analysed in conjunction.

We observed by flow cytometry that 2 h after hUC-MSC administration, the proportion of monocytes/M0 macrophages increased by approximately 2.8x when compared to control. After 24 h, there was a sharp decrease (Figure 18a, left). Pro-inflammatory monocytes/M0macrophages increased ~2-fold at 2 h (Figure 18a, middle), followed by a shift of this population toward an M2 phenotype at 24 h, with an approximate 3.2x increase (Figure 18a, right).

To study immune cell polarization, lung tissue sections were co-stained for CD11b and LY6C (M1 monocytes). The distribution of classically activated monocytes was even throughout the tissue without a preference for accumulating around the hUC-MSCs at any time point (Figure 18b). Quantification of M1 monocytes showed an infiltration of these cell into the lung at 2 h which was sustained at 24 h (Figure 18c). M2 monocytes were not investigated by immunofluorescence due to technical challenges regarding antibody performance. Nevertheless, it would be expected to observe an increase in these cells 24 h post cell injection (116).

Co-staining for the F4/80 and CD16/32 markers revealed that M1 macrophages distributed homogeneously throughout the tissue without clustering preferentially around hUC-MSCs (Figure 18d), suggesting a global inflammatory state in the lungs. Quantification showed that M1 macrophages infiltrate the lung 2 h after cell injection with the level of these cells remaining high at 24 (Figure 18e). To identify M2 macrophages, we used the F4/80 and CD206 markers. Double-labelled cells were observed homogeneously

distributed within the tissue at 24 h (Figure 18f) in agreement with the quantification which showed that M2 macrophages increase only after 24 h (Figure 18g).

All in all, the monocyte/M0 macrophage population was increased significantly 2 h post hUC-MSC injection. At this time point, an inflammatory response was observed as both monocytes and macrophages differentiated toward an M1 phenotype. At 24 h, although the levels of M1 cells remained high, as shown by immunofluorescence, a resolution of inflammation phase was observed as the monocytes and macrophages acquired an M2 phenotype.
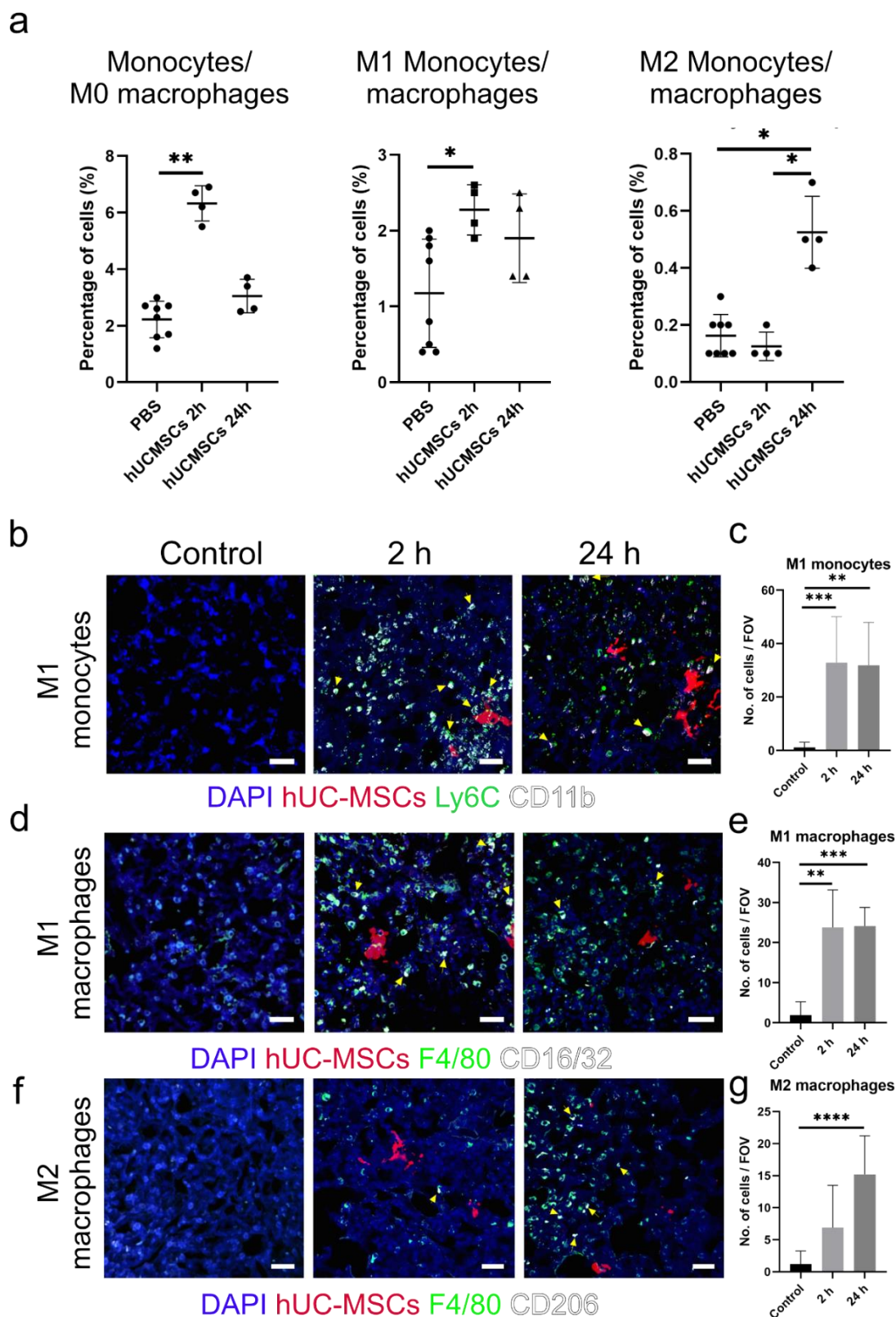
Figure 18. Monocytes and M0 macrophages in the lung show a 2-step polarization response to IV injection of hUC-MSCs. a) Flow cytometry showed that the CD11b^{hi} MHC II$^{+/-}$ CD64$^{+/-}$ monocyte and M0 macrophage populations increased at 2 h and presented a classically activated phenotype. At 24 h these cells transitioned toward an alternatively activated phenotype. Percentage of

total cells is displayed in the y-axis. Kruskal-Wallis test with multiple comparisons. control n=8, hUC-MSC group n=4. P<0.05 *. b) (CD11b [white] + Ly6C [green]) classically activated monocytes distribution in the lungs (yellow arrows). Scale bar = 30 µm. c) Immunofluorescence quantification of LY6C + CD11b M1 monocytes. Kruskal-Wallis test with multiple comparisons. n=9. P<0.005 **; P<0.0005 ***. d) M1 macrophages (F4/80 [green] + CD16/32 [white]) biodistribution in the lung after cell therapy (yellow arrows). Scale bar = 30 µm. e) Immunofluorescence quantification of F4/80 + CD16/32 M1 macrophages. Kruskal-Wallis test with multiple comparisons. n=9. P<0.005 **; P<0.0005 ***. f) (F4/80 [green] + CD206 [white]) M2 macrophages distribution (yellow arrowheads). Scale bar = 30 µm. g) Immunofluorescence quantification of F4/80 + CD206 M2 macrophages Kruskal-Wallis test with multiple comparisons. n=9. P<0.00005 ****.

4.2.6 Effect of hUC-MSCs on the proportion and polarization of lung macrophage subpopulations

As shown in Figure 18, IV administration of hUC-MSC increased the overall macrophage levels in the lung. The rapid increase in macrophage number within a 2 h period suggests that these macrophages are infiltrating macrophages from the blood circulation (282). However, it is not clear whether the hUC-MSCs also have any effect on the resident macrophage populations in the lung, which comprise interstitial and alveolar macrophages. To address this, we used flow cytometry to investigate the effect of hUC-MSCs on Cd11b⁻ CD11c^{hi} CD64$^+$ alveolar and MHC II$^+$ CD11b$^+$ CD64$^+$ CD24$^-$ interstitial macrophages as well as on their polarization status.

The analysis showed that although not significant, a trend toward lower alveolar cell number was observed at 2 h. The resident alveolar macrophage levels, with just a 0.4x increase at 24 h, remained relatively stable after hUC-MSC infusion (Figure 19a, left). With a 0.5x drop in M1 macrophages, these cells showed a similar trend to the overall population. The MSCs did not trigger a pro-inflammatory response in these cells (Figure 19a, middle). M2 alveolar macrophages were below the level of detection at 2 h, but the 0.16x increase at 24 h does not suggest that alveolar macrophages change their phenotype toward an M2 activation state (Figure 19a, right). The interstitial macrophage population remains unchanged 2 h post cell injection but increased by 2.8x 24 h later. At this timepoint, polarization toward both, an M1 and M2 phenotypes was observed, with increases of 2.3 and 4.2x, respectively (Figure 19b).

IV administration does not seem to have an effect on alveolar macrophages in the lung. On the contrary, the levels of interstitial macrophages are significantly increased and show an initial inflammatory phase that shifts toward a regulatory phase at 24 h, once most of the infused cells have been cleared.
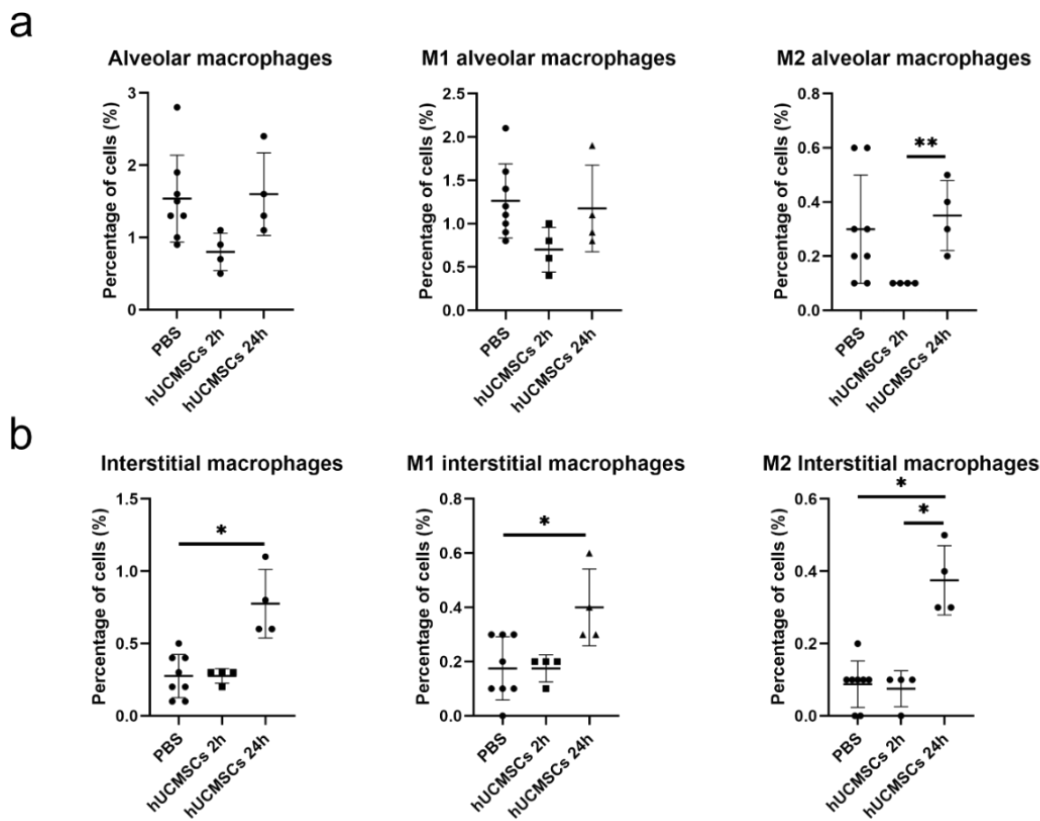
Figure 19. Macrophage subsets and their polarization after IV administration of hUC-MSCs. a) Flow cytometric analysis of *Cd11b⁻ CD11cʰⁱ CD64⁺* alveolar macrophages and their polarisation in the lung b) *MHC II⁺ CD11b⁺ CD64⁺ CD24⁻* interstitial macrophages were also analysis for changes in their proportion and polarisation by flow cytometry. *Percentage of total cells is displayed in the y-axis.* Kruskal-Wallis test with multiple comparisons. control n=8, hUC-MSC group n=4. P<0.05 * P<0.005 **.

4.3   Discussion

In this study, we implemented a gating strategy to analyse the innate immune cell response to the administration of IV-infused hUC-MSCs in the mouse lung by flow cytometry. Moreover, to study the location and biodistribution of the immune cells impacted by cell therapy, we performed histological analysis.

Overall, hUC-MSCs triggered an innate immune response shortly after being infused intravenously. The levels of granulocytes -particularly neutrophils-,

monocytes and macrophages were increased 2 h post-hUC-MSC administration. At this time point, the myeloid cells were found surrounding the administered cells. This suggests that the clearance of hUC-MSC from the lungs might involve efferocytosis by phagocytes. Moreover, monocytes and macrophages acquired a pro-inflammatory phenotype, which agrees with studies that have shown that MSCs delivered IV induce an inflammatory response (262). After 24 h, the levels of neutrophils returned to baseline and a shift of the monocytes and macrophages toward an anti-inflammatory phenotype was observed. The resident alveolar macrophage population did not react to the infusion of exogenous cells, but the lung interstitial macrophages increased at the 24 h time point and showed both a pro- and anti-inflammatory phenotype.

Identifying myeloid cell subtypes and their polarization state in the lung is a complex task. Several myeloid populations express similar and overlapping markers. Moreover, researchers have used inconsistent antibody panels resulting in a lack of strictly defined identifiers for specific cell subsets (283). We followed a well-established protocol (272) and modified it in accordance with our instrument's limitations and experimental goals, offering a novel approach to studying the changes in the proportion of different myeloid cells to hUC-MSC delivery *in vivo*.

We and others have shown that hUC-MSC administered IV leads to the cells accumulating in the lungs and are cleared within 24 h (33,35,38,284). Given that the hUC-MSCs are short-lived, their mechanisms of action in the resolution of disease are still unclear.

Hypotheses regarding the limited survival and rapid clearance of MSC in the lung include apoptosis (270), lack of nutrients/growth factors (285), mechanical stress/anoikis (286), hypoxia (287), and phagocytosis by immune cells (117,288).

We showed that interactions between transplanted MSCs with phagocytic myeloid cells occur shortly after administration. In agreement with our data, others have shown direct interactions of MSCs with host platelets and neutrophils *in vivo* (289), and that MSCs colocalize with macrophage and

granulocyte markers via immunofluorescence *ex vivo* (270), suggesting that MSCs might affect the innate immune system through cell-to-cell interactions (290).

Moreover, we observed a 4.5-fold increase in neutrophils and a 2.8-fold increase in monocytes and M0 macrophages 2 h after hUC-MSC IV injection. Although trends for increased neutrophil levels have been reported (262), the results were not as significant as the ones shown here. In contrast, an increase in monocyte chemo attractants, as well as proinflammatory cytokines (116), and a doubling of macrophages in the lung agrees with our findings that IV delivery of hUC-MSCs increases these cells (262).

The rapid increase in neutrophils, monocytes and macrophages in response to the hUC-MSCs corresponds to a typical innate immune reaction to pathogens (44), suggesting that the administered hUC-MSCs are recognized as foreign and trigger an inflammatory response. Supporting this hypothesis, we observed that the monocytes and macrophages infiltrating the lungs after cell therapy displayed an inflammatory phenotype 2 h after cell infusion, which agrees with reports suggesting that mice whose lungs have been challenged, have increased numbers of infiltrating monocytes in this organ (291).

In this study, we used xenogeneic cells, but studies that have used syngeneic (262) and allogeneic (292) MSCs have also observed an inflammatory immune reaction after MSC delivery, suggesting that the response is not due to the cells being from other species, but rather a response to the MSCs being present in high numbers at an unusual location, which initiates a clearance mechanism (262). In line with this, the immune system reacts to cells that are not normally in contact with the bloodstream (293). The direct interaction between the MSCs and the blood immediately after infusion might trigger an instant blood-mediated inflammatory reaction (IBMIR), that would not be expected when administering cells that are normally present in the blood circulation, such as leukocytes (294). IBMIR causes platelet-, coagulation-, and complement activation, and results in the MSCs being destroyed quickly, inducing the innate immune system to eliminate them (295).

At 24 h post-hUC-MSC administration, we observed an increased monocyte/macrophage polarization toward an immune-regulatory phenotype, indicating a resolution of the initial inflammatory phase. The production of suppressive myeloid cells after close interaction with MSCs has been described as one of the mechanisms by which the therapeutic cells exert positive disease outcomes (296). Phagocytosis has been linked to myeloid cell anti-inflammatory polarization (114).

Phagocytosis of exogenous MSCs by innate immune cells has been demonstrated *in vivo* by Braza *et al.* (117) PKH26 labelled MSCs were injected into mice and the label was found in lung resident macrophages, monocytes, and neutrophils by flow cytometry (117). De Witte *et al* concluded that MSC phagocytosis triggers monocytes to adopt an anti-inflammatory phenotype, which is critical in the mediation of the MSC immunomodulatory effects (116). Moreover, macrophages in the lung that had phagocytosed IV-delivered MSCs expressed an anti-inflammatory phenotype, while macrophages that did not phagocytose MSCs displayed a pro-inflammatory phenotype (117).

In this study, phagocytosis of hUC-MSCs was not evaluated by flow cytometry and no tdTomato was observed inside the myeloid cells by microscopy. This might be due to the small amount of tdTomato uptaken by the immune cells, resulting in an undetectable signal. Nevertheless, the fact that granulocytes, monocytes and macrophages are found in close contact with hUC-MSCs suggests that these cells may be involved in phagocytosing them. However, it isn't clear if the immune cells play any role in inducing the death of the hUC-MSCs.

Innate immune leukocytes regulate lymphocytes of the adaptive immune system and orchestrate more complex immune responses (297,298). Although we did not look at the adaptive immunity in response to IV injected hUC-MSCs, studies suggest that MSCs modulate B- and T- cells (65,67,68,299). *In vitro*, mechanisms such as skewing of monocytes toward anti-inflammatory macrophages (299), suppression by soluble factors (65,67), direct inhibition of proliferation (300), and induction of anti-inflammatory phenotypes have been described (301). *In vivo*, preventive IV injection of MSCs ameliorated

experimental autoimmune encephalomyelitis by inhibiting T-cell proliferation and preventing the secretion of pro-inflammatory cytokines (302).

MSCs can also mediate innate immune cell polarization through their secretome (303), which includes soluble proteins, cytokines, chemokines, lipids, free nucleic acids and exosomes, which might contain mitochondria (304). An example of secretome-mediated immune response was shown when after IV infusion, MSCs improved myocardial infarction by secreting the anti-inflammatory protein TSG-6 in mice (26).

The shape and size of the hUC-MSCs present in the lung after IV infusion varies. Large, medium, and small hUC-MSC clumps, have been observed as round or elongated shapes. In addition to phagocytosis, this might be explained given that rapidly after transplantation, MSCs fragment, losing their cellular and nuclear integrity, and they undergo apoptosis (270).

Apoptosis *in vivo* might be required for the MSCs to exert their benefits (114). After IV injection, MSCs undergo apoptosis in the lung. Their subsequent efferocytosis by macrophages was suggested to be the mechanism behind the reduction in the severity of allergic asthma (118). Moreover, clinical data from patients with graft-versus-host disease (GvHD) who have been administered MSCs intravenously and preclinical murine models showed that the host's cytotoxic cells actively induce the exogenous MSCs to undergo apoptosis. This results in *in vivo* recipient-induced immunomodulation which is required for improved outcomes. In addition, their work demonstrated that the delivery of apoptotic MSCs produced *ex vivo* might circumvent the requirement for recipient cytotoxic cell activity (119).

MSC viability might not be necessary in some contexts. Heat-inactivated MSCs maintain immunomodulatory capacity and reduce sepsis in mice in a secretome and immune cell crosstalk-independent manner (305,306). In our study, we used viable hUC-MSCs. It remains an open question whether apoptotic/unviable cells have a different effect on the innate immune system *in vivo.*

Regarding lung resident macrophages, our data showed that IV hUC-MSCs do not induce changes in the proportion or phenotype of alveolar

macrophages. In contrast, others have shown that IV MSC injection induces a slight increase in alveolar macrophages (118). Moreover, alveolar macrophages were observed efferocytosing the exogenous MSCs, which caused major transcriptional changes that reprogrammed the alveolar macrophages toward an M2 phenotype (118). Similarly, MSCs injected IV induced polarization of alveolar macrophages to an immune regulatory phenotype without raising their levels (307). Moreover, another study found that alveolar macrophages were significantly increased after IV delivery of BM-, UC- or AD-MSCs (308). This might be explained by the fact that healthy mice were used in the current study, while the three studies cited above used a mouse model of allergic asthma. Alveolar macrophages are the first immune effector cells at the air-lung interphase (309), meaning that the induction of asthma might have activated, primed and mobilized the alveolar macrophages prior to MSC therapy (47). Thus, it is difficult to attribute the observed effects on the alveolar macrophages solely to the delivery of MSCs.

As discussed above, the disease context or inflammatory conditions can influence the outcome arising from MSC delivery, as well as differentially alter MSC behaviour (69,310). MSCs can either promote or suppress the immune response as shown by *in vitro* culture of MSCs exposed to different clinical bronchoalveolar lavage (BAL) samples representing a wide range of lung pathologies (310). In our study, healthy animals were used; if injured animals had been studied, it is possible that the results might have differed. Thus, the understanding of the effect of IV delivery of hUC-MSCs on the innate immune system in different disease and inflammatory contexts remains to be elucidated.

Regarding lung interstitial macrophages, we observed an 2.8-fold increase in interstitial macrophages at 24 h, which agrees with Pang, et al. who observed that lung interstitial macrophages play an important role in the clearance of exogenous MSCs (118).

Finally, regarding the tissue biodistribution of myeloid cells, although some cells such as neutrophils seemed to cluster around hUC-MSCS, it was interesting to observe that M1 monocytes and macrophages were also present

at sites were no MSCs were observed. A possible explanation is that MSCs induce a global immune activating state in the lungs. Alternatively, the MSCs might be missed at sites of dense immune cells as they could be adjacent to the field of view.

The MSCs' immunoregulatory properties related to beneficial effects on disease remain unclear. Nevertheless, immunomodulation by innate immune cells mediated by the MSCs secretome as well as by direct interaction with viable, apoptotic, inactivated, and fragmented MSCs after delivery has been established (114). Moreover, upon contact with MSCs, the innate immune cells adapt their phenotype according to the disease context and maintain a footprint that induced therapeutic effects without long-term engraftment (51).

4.4 Conclusion

We performed a comprehensive flow cytometry and histological analysis of mouse lungs following IV administration of hUC-MSCs to investigate the fate of the hUC-MSCs and their effect on the cells of the innate immune system.

We showed that in healthy, immunocompetent mice, an inflammatory response, dominated by an increase in granulocytes, particularly neutrophils, and pro-inflammatory monocytes and macrophages in the lungs, occurred 2 h after cell delivery. These cells were frequently observed in proximity to the hUC-MSCs, which may indicate that they participate in their clearance by means of phagocytosis. After 24 h, a resolution of the inflammatory phase is observed as anti-inflammatory monocytes and macrophages are more prevalent in the lung. These processes might be involved in the immunomodulatory response following MSC infusion in models of disease. Further research is necessary to ascertain the exact cause of the immune response to better tailor cell therapies to specific conditions.

Chapter 5. General discussion and conclusions

MSC therapies have shown favourable results in preclinical models of numerous diseases. Nevertheless, few clinically approved therapies exist (20). To determine whether MSC treatments are suitable for clinical use it is important to evaluate the safety of delivering exogenous MSCs intravenously, given that due to ease of access and patient comfort, this is the preferred administration route (311). IV infused MSCs become entrapped in the lungs due to their relatively large size in comparison to the diameter of the pulmonary capillaries, and the expression of surface molecules that interact with the lung's endothelium (38,36,42). Moreover, they are rapidly cleared from the body (270). Given the short lifespan of MSCs following IV administration and their restricted distribution, it is unclear how they realize their benefits (116). Thus, assessing MSC safety and understanding their mechanisms of action is important for the development of appropriate clinical applications.

Therefore, the main goal of this study was to evaluate the safety, distribution and fate of hUC-MSC therapies using imaging tools. Particularly, the first aim was to track the biodistribution of hUC-MSC *in vivo* using non-invasive multimodal imaging modalities such as BLI, micro-CT and MSOT. Secondly, to evaluate the distribution of the cells within the lung *ex vivo* at single cell resolution. Lastly, to investigate the fate of the hUC-MSCs in the lung and their effect on host immune cell populations.

The results in each chapter will be discussed.

1. Comparison of the effectiveness of MSOT and micro-CT for tracking gold-labelled MSCs *in vivo*.

In chapter 2 of this thesis, it was demonstrated that MSOT could identify the gold-labelled MSCs following subcutaneous administration, but was unable to image the cells within the lung following IV administration due to the presence of air in this organ. On the other hand, micro-CT could be used to generate anatomical images of the lungs but was unable to detect the gold-labelled cells due to poor sensitivity.

The interest in micro-CT stemmed from multiple reports suggesting that micro-CT tracking of gold-labelled cells is feasible (141,202,204,214,312). If this were true, due to the ability of micro-CT to generate high resolution lung images (313), it would offer insights into the intra-lung biodistribution of IV delivered MSC therapies *in vivo*.

In a preliminary phantom study, where gold nanorod solutions were imaged in microfuge tubes, it was observed that the amount of gold necessary to detect any signal would be extremely high, constituting a problem regarding effects on cell viability and/or phenotype as well as a monetary toll that would make this approach unfeasible.

Most studies that have used micro-CT to image gold-labelled cells report positive results. It is interesting that a number of papers on this topic were published by the same research group and display unexpectedly similar figures (314–319). In contrast with their results, the conclusion reached in this thesis was that micro-CT is not a sensitive technique for tracking gold labelled cells under the experimental conditions tested. The mathematical reasoning to support this is outlined in the discussion section of chapter 2.

micro-CT imaging using gold for cell tracking is far from becoming a reality. Aside of the fact that conventional micro-CT scanners lack sensitivity toward gold, the research in this area would first need to reach a consensus on the ideal size, shape, concentration, delivery route, and chemical modifications of the gold nanoparticles, given that currently, nanoparticles that vary widely in the aforementioned parameters are being used (320).

Although visualizing the hUC-MSCs by BLI was possible, this imaging modality is limited by low spatial resolution which does not allow the biodistribution of the cells to be mapped at the intra-organ level (136).

Alternative *in vivo* imaging modalities that might be useful to track nanoparticle-labelled MSCs in the lung include zero-echo time (ZTE) MRI and magnetic particle imaging (MPI).

Lung imaging using conventional MRI has been complicated given the low proton density of this organ as well as respiratory motion artefacts (321).

ZTE imaging is a fast gradient echo-based MRI sequence capable of capturing the intrinsic signal of the lung parenchyma. ZTE MRI overcomes the problems associated with imaging lung tissue and provides high-resolution pulmonary structural information (322). Additionally, MRI has been used to track MSCs labelled with iron oxide nanoparticles (323), making the application of ZTE MRI an interesting avenue to study the fate of MSCs within the lung.

MPI relies on the electronic magnetization of iron oxide nanoparticles as opposed to the nuclear magnetization necessary for MRI. This results in MPI achieving higher sensitivity and specificity without depth limitations (324). Moreover, this imaging technology has no optical limitations working robustly in the lungs and has been used to track iron oxide labelled MSCs in this organ (325).

Failing to monitor the hUC-MSC therapy *in vivo* within the lungs with micro-CT, led to the exploration of *ex vivo* methods such as optical tissue clearing to study the biodistribution and fate of the fluorescent reporter hUC-MSCs in the lung by microscopy at single cell resolution.

2. Evaluation of the distribution of the hUC-MSCs within the lung *ex vivo* at single cell resolution.

Numerous tissue-clearing protocols, based on organic or aqueous chemicals, are available. Depending on the tissue type, size and imaging applications, these techniques can produce variable results. It can be overwhelming for the research community to choose between the different methods. Thus, three different approaches were systematically tested for their ability to not only clear the lungs, whilst maintaining their integrity and morphology, but also to retain the fluorescent label and allow vasculature staining.

In this chapter, the results showed that there was not a single universal method achieving all the requirements for our application. However, the CUBIC clearing protocol gave the best results because it preserved the fluorescence of the administered reporter cells. CUBIC in combination with immunofluorescent microscopy allowed the study of the 3D interactions of the hUC-MSCs with endothelial and innate immune cells. Nevertheless, this

methodology is challenging, and the staining protocols need to be adapted on an antibody-by-antibody basis. Although a given protocol might work reliably in 2D sections, translating it to 3D cleared sections is not straightforward. More work would be necessary to optimize the staining protocols and use this approach for volumetric imaging of the immune processes triggered by the IV administration of hUC-MSCs.

When establishing an optical tissue clearing method for a specific application, many considerations are required, one of which is the technical characteristics of the microscopes available to obtain the best possible images. To avoid optical aberrations, it is important to match the RI of the cleared samples (326). Unfortunately, the microscope objectives available in the confocal system used in this study were not ideal and I did not have access to facilities elsewhere. The high magnification, oil immersion objectives, which would have allowed for a correct refractive index matching had a short working distance that made it impossible to work with samples as thick as the ones used in this study (500 μm). Thus, an air objective had to be used, which resulted in a RI mismatch and did not yield images that were suitable for quantification. Nevertheless, provided that tailored microscope objectives can be used, it can be concluded that the CUBIC clearing protocol in combination with fluorescent labelling strategies offers a novel approach to investigate the volumetric distribution of IV administered MSCs within the lung and their interactions with host cells.

3. **Investigating the fate of the hUC-MSCs in the lung and their effect on host immune cell populations.**

Studying the effect of hUC-MSCs on the lung's innate immune cells in 3D cleared sections was challenging; thus, chapter 4 focused on studying this in more detail by using immunofluorescence of thin sections to study the spatial distribution of the cells. Moreover, a comprehensive flow cytometric analysis was established to study changes in the number of these cells. To the best of my knowledge, such an approach has been reported in this thesis for the first time. Nevertheless, some recommendations on how to improve the panel will be discussed.

The instrument used in the present study allowed for up to 8 different markers to be assessed simultaneously, which posed a limitation for the panel design. If a flow cytometer with higher capacity would have been available, the panel of markers could have been simplified, eliminating the need for setting up two different panels and gating strategies.

Moreover, in the gating strategy used here, it is possible that the alveolar macrophage population could be contaminated with DCs, as it was not possible to separate these populations. DCs display phagocytic activity, and it could have been expected that they also participate in the innate immune response triggered by the infusion of hUC-MSCs. Nevertheless, given that the change in the alveolar macrophage levels was not significant, it could be assumed that the DCs were also not highly impacted by the administration of hUC-MSC. This agrees with the findings that the importance of DCs may not be as great as that of macrophages, as it has been shown by treating mice with chlodronate before MSC therapy. Chlodronate preferentially depletes macrophages while leaving DCs unaffected. These treatment impairs the therapeutic effects of MSCs indicating that macrophages play a more important role (119).

Moreover, although differentiating between monocytes and macrophages is challenging given that these express similar surface markers, adding a marker that is exclusively expressed by monocytes such as CD115 might be beneficial (327).

It has been repeatedly shown that MSC administration skews macrophages toward an M2 state (117,263,266,296,307). On the other hand, it has been suggested that shortly after MSC IV delivery, an inflammatory response is observed (262). In this chapter, it is described for the first time that IV administration of hUC-MSCs into mice results in a two-step innate immune response; It is characterised by an initial pro-inflammatory immune reaction and followed by a resolution phase.

Nevertheless, it is important to remember that the M1, M2 polarisation classification used in this study is very simplistic (328). Polarisation is not limited to the pro- and anti-inflammatory states, and overlapping phenotypes

and populations may exist simultaneously within the same tissue (272). Perhaps gene expression analysis in pulmonary myeloid cell populations at different hUC-MSC administration time points would allow for a deeper understanding of monocyte and macrophage polarization status.

Although new insights have been gained from this study, several open questions remain. Thus, future studies could benefit from the protocols established in this thesis and go beyond the innate immune system to study the response of the adaptive immune response to cell therapies. Moreover, it would be interesting to evaluate whether the immune response would be different if MSCs from other sources were used, whether cell dose has an impact, or if our observations would have differed if unviable or apoptotic MSCs, MSC membrane particles, or primed MSCs were used. Finally, exploring these questions in animal models of injury, such as the renal ischemia reperfusion mouse model would be of interest. Moreover, administering the MSCs as preventative as well as therapeutic measures, would shed light on whether the immune response to administered MSCs varies depending on the disease context. This information could expand on the knowledge about the potential mechanisms of action by which MSCs might ameliorate acute kidney injury.

Conclusions

In summary, this thesis explored a variety of imaging approaches to study the safety, biodistribution and fate of hUC-MSCs administered intravenously into healthy mice. Using BLI and microscopy, this study confirmed and expanded on the findings that hUC-MSCs get trapped in the lung vasculature and are cleared rapidly. In a novel multi-modal imaging approach to track gold labelled-hUC-MSCs *in vivo*, it was demonstrated that although MSOT does not permit lung imaging, it is a sensitive imaging modality to detect gold-labelled cells indicating the potential of a BLI and MSOT multi-modal approach for cell tracking applications. In contrast, micro-CT is a useful method to acquire morphological images of the lung but it is not sensitive enough for tracking gold-labelled cells. *Ex vivo*, after comparing three optical tissue clearing protocols, it was established that the CUBIC protocol enabled fluorescent

reporter hUC-MSC tracking within the lungs at single-cell resolution. In addition, immunolabeling CUBIC-cleared samples allowed the study of the interactions of hUC-MSCs with endothelial and immune cells. It was observed that hUC-MSCs seem to remain in close contact with the lung microvasculature, potentially forming emboli given the high expression of pro-coagulant tissue factor. Moreover, hUC-MSC administration triggers a rapid neutrophil infiltration into the lungs. Finally, by further investigating the interactions between the administered hUC-MSCs and the innate response in the lungs, this thesis adds to the knowledge behind the potential therapeutic mechanisms of action of MSCs in disease. Our results showed that an inflammatory response, characterised by mobilization of neutrophils, monocytes and pro-inflammatory macrophages, takes place in the lung two hours after cell delivery. Twenty-four hours post cell infusion, the number of innate immune cells in the lungs decreased but a polarization toward an anti-inflammatory phenotype was observed. Moreover, immunofluorescent staining revealed that neutrophils were preferentially distributed in close proximity to the hUC-MSCs, suggesting that their clearance within 24 h might involve efferocytosis.

Taken together, these results showed that MSCs induce an inflammatory response in the lungs, which then leads to a subsequent increase in anti-inflammatory monocytes and macrophages. In future studies it would be interesting to investigate the interactions between administered MSCs and immune cells in different injury models.

References

1.	Pichardo AH, Littlewood J, Taylor A, Wilm B, Lévy R, Murray P. Computed tomography lacks sensitivity to image gold labelled mesenchymal stromal cells in vivo as evidenced by multispectral optoacoustic tomography bioRxiv; 2022. p. 2022.06.15.495483.

2.	Pichardo AH, Amadeo F, Wilm B, Lévy R, Ressel L, Murray P, et al. Comparison between optical tissue clearing methods for detecting administered mesenchymal stromal cells in mouse lungs. bioRxiv; 2022. p. 2022.07.23.501233.

3.	Pichardo AH, Wilm B, Liptrott N, Murray P. Intravenous administration of human umbilical cord mesenchymal stromal cells leads to an inflammatory response in the lung [Internet]. bioRxiv; 2022 [cited 2022 Sep 27]. p. 2022.09.26.509547.

4.	Friedenstein AJ, Chailakhjan RK, Lalykina KS. The Development of Fibroblast Colonies in Monolayer Cultures of Guinea-Pig Bone Marrow and Spleen Cells. Cell Proliferation. 1970;3(4):393–403.

5.	Li T, Xia M, Gao Y, Chen Y, Xu Y. Human umbilical cord mesenchymal stem cells: an overview of their potential in cell-based therapy. Expert Opin Biol Ther. 2015;15(9):1293–306.

6.	Sharpe PT. Dental mesenchymal stem cells. Development. 2016 Jul 1;143(13):2273–80.

7.	Bunnell BA. Adipose Tissue-Derived Mesenchymal Stem Cells. Cells. 2021 Dec 6;10(12):3433.

8.	Li N, Gao J, Mi L, Zhang G, Zhang L, Zhang N, et al. Synovial membrane mesenchymal stem cells: past life, current situation, and application in bone and joint diseases. Stem Cell Res Ther. 2020 Sep 7;11(1):381.

9.	Hass R, Kasper C, Böhm S, Jacobs R. Different populations and sources of human mesenchymal stem cells (MSC): A comparison of adult and neonatal tissue-derived MSC. Cell Commun Signal. 2011 May 14;9:12.

10.   Dominici M, Blanc KL, Mueller I, Slaper-Cortenbach I, Marini FC, Krause DS, et al. Minimal criteria for defining multipotent mesenchymal stromal cells. The International Society for Cellular Therapy position statement. Cytotherapy. 2006 Jan 1;8(4):315–7.

11.   Medrano-Trochez C, Chatterjee P, Pradhan P, Stevens HY, Ogle ME, Botchwey EA, et al. Single-cell RNA-seq of out-of-thaw mesenchymal stromal cells shows tissue-of-origin differences and inter-donor cell-cycle variations. Stem Cell Research & Therapy. 2021 Nov 4;12(1):565.

12.   Pevsner-Fischer M, Levin S, Zipori D. The origins of mesenchymal stromal cell heterogeneity. Stem Cell Rev Rep. 2011 Sep;7(3):560–8.

13.   Muraglia A, Cancedda R, Quarto R. Clonal mesenchymal progenitors from human bone marrow differentiate in vitro according to a hierarchical model. J Cell Sci. 2000 Apr;113 (Pt 7):1161–6.

14.   DiGirolamo CM, Stokes D, Colter D, Phinney DG, Class R, Prockop DJ. Propagation and senescence of human marrow stromal cells in culture: a simple colony-forming assay identifies samples with the greatest potential to propagate and differentiate: Human Marrow Stromal Cells in Culture. British Journal of Haematology. 1999 Nov;107(2):275–81.

15.   Musiał-Wysocka A, Kot M, Majka M. The Pros and Cons of Mesenchymal Stem Cell-Based Therapies. Cell Transplant. 2019 Jul;28(7):801–12.

16.   Song N, Scholtemeijer M, Shah K. Mesenchymal Stem Cell Immunomodulation: Mechanisms and Therapeutic Potential. Trends Pharmacol Sci. 2020 Sep;41(9):653–64.

17.   Amadeo F, Trivino Cepeda K, Littlewood J, Wilm B, Taylor A, Murray P. Mesenchymal stromal cells: what have we learned so far about their therapeutic potential and mechanisms of action? Emerging Topics in Life Sciences. 2021 Sep 8;5(4):549–62.

18.   Ankrum JA, Ong JF, Karp JM. Mesenchymal stem cells: immune evasive, not immune privileged. Nat Biotechnol. 2014 Mar;32(3):252–60.

19. Galipeau J, Sensébé L. Mesenchymal Stromal Cells: Clinical Challenges and Therapeutic Opportunities. Cell Stem Cell. 2018 Jun 1;22(6):824–33.

20. Levy O, Kuai R, Siren EMJ, Bhere D, Milton Y, Nissar N, et al. Shattering barriers toward clinically meaningful MSC therapies. Sci Adv. 2020 Jul;6(30):eaba6884.

21. Han Y, Li X, Zhang Y, Han Y, Chang F, Ding J. Mesenchymal Stem Cells for Regenerative Medicine. Cells. 2019 Aug;8(8):886.

22. Jiang Y, Zhang P, Zhang X, Lv L, Zhou Y. Advances in mesenchymal stem cell transplantation for the treatment of osteoporosis. Cell Proliferation. 2021;54(1):e12956.

23. Freitas J, Santos SG, Gonçalves RM, Teixeira JH, Barbosa MA, Almeida MI. Genetically Engineered-MSC Therapies for Non-unions, Delayed Unions and Critical-size Bone Defects. Int J Mol Sci. 2019 Jul 12;20(14):E3430.

24. Zhang R, Ma J, Han J, Zhang W, Ma J. Mesenchymal stem cell related therapies for cartilage lesions and osteoarthritis. Am J Transl Res. 2019;11(10):6275–89.

25. Staff NP, Jones DT, Singer W. Mesenchymal Stromal Cell Therapies for Neurodegenerative Diseases. Mayo Clin Proc. 2019 May;94(5):892–905.

26. Lee RH, Pulin AA, Seo MJ, Kota DJ, Ylostalo J, Larson BL, et al. Intravenous hMSCs Improve Myocardial Infarction in Mice because Cells Embolized in Lung Are Activated to Secrete the Anti-inflammatory Protein TSG-6. Cell Stem Cell. 2009 Jul 2;5(1):54–63.

27. Öztürk S, Elçin AE, Elçin YM. Functions of Mesenchymal Stem Cells in Cardiac Repair. Adv Exp Med Biol. 2021;1312:39–50.

28. Papanikolaou IG, Katselis C, Apostolou K, Feretis T, Lymperi M, Konstadoulakis MM, et al. Mesenchymal Stem Cells Transplantation following Partial Hepatectomy: A New Concept to Promote Liver Regeneration-

Systematic Review of the Literature Focused on Experimental Studies in Rodent Models. Stem Cells Int. 2017;2017:7567958.

29.   Rodgers K, Jadhav SS. The application of mesenchymal stem cells to treat thermal and radiation burns. Adv Drug Deliv Rev. 2018 Jan 1;123:75–81.

30.   Liu X, Cai J, Jiao X, Yu X, Ding X. Therapeutic potential of mesenchymal stem cells in acute kidney injury is affected by administration timing. Acta Biochim Biophys Sin (Shanghai). 2017 Apr 1;49(4):338–48.

31.   Wang S, Li Y, Zhao J, Zhang J, Huang Y. Mesenchymal stem cells ameliorate podocyte injury and proteinuria in a type 1 diabetic nephropathy rat model. Biol Blood Marrow Transplant. 2013 Apr;19(4):538–46.

32.   Zhuo W, Liao L, Fu Y, Xu T, Wu W, Yang S, et al. Efficiency of endovenous versus arterial administration of mesenchymal stem cells for ischemia-reperfusion-induced renal dysfunction in rats. Transplant Proc. 2013 Mar;45(2):503–10.

33.   Eggenhofer E, Benseler V, Kroemer A, Popp FC, Geissler EK, Schlitt HJ, et al. Mesenchymal stem cells are short-lived and do not migrate beyond the lungs after intravenous infusion. Front Immunol. 2012 Sep;3:297.

34.   Kosaric N, Srifa W, Bonham CA, Kiwanuka H, Chen K, Kuehlmann BA, et al. Macrophage Subpopulation Dynamics Shift following Intravenous Infusion of Mesenchymal Stromal Cells. Mol Ther. 2020 Sep 2;28(9):2007–22.

35.   Scarfe L, Taylor A, Sharkey J, Harwood R, Barrow M, Comenge J, et al. Non-invasive imaging reveals conditions that impact distribution and persistence of cells after in vivo administration. Stem Cell Res Ther. 2018 Nov 28;9:332.

36.   Masterson CH, Tabuchi A, Hogan G, Fitzpatrick G, Kerrigan SW, Jerkic M, et al. Intra-vital imaging of mesenchymal stromal cell kinetics in the pulmonary vasculature during infection. Sci Rep. 2021 Mar 4;11(1):5265.

37.   Leibacher J, Henschler R. Biodistribution, migration and homing of systemically applied mesenchymal stem/stromal cells. Stem Cell Research & Therapy. 2016 Jan 11;7(1):7.

38.   Fischer UM, Harting MT, Jimenez F, Monzon-Posadas WO, Xue H, Savitz SI, et al. Pulmonary Passage is a Major Obstacle for Intravenous Stem Cell Delivery: The Pulmonary First-Pass Effect. Stem Cells and Development. 2009 Jun;18(5):683.

39.   Schrepfer S, Deuse T, Reichenspurner H, Fischbein MP, Robbins RC, Pelletier MP. Stem cell transplantation: the lung barrier. Transplant Proc. 2007 Mar;39(2):573–6.

40.   Kerkelä E, Hakkarainen T, Mäkelä T, Raki M, Kambur O, Kilpinen L, et al. Transient proteolytic modification of mesenchymal stromal cells increases lung clearance rate and targeting to injured tissue. Stem Cells Transl Med. 2013 Jul;2(7):510–20.

41.   Nystedt J, Anderson H, Tikkanen J, Pietilä M, Hirvonen T, Takalo R, et al. Cell surface structures influence lung clearance rate of systemically infused mesenchymal stromal cells. Stem Cells. 2013 Feb;31(2):317–26.

42.   Wang S, Guo L, Ge J, Yu L, Cai T, Tian R, et al. Excess Integrins Cause Lung Entrapment of Mesenchymal Stem Cells. Stem Cells. 2015 Nov;33(11):3315–26.

43.   Parkin J, Cohen B. An overview of the immune system. Lancet. 2001 Jun 2;357(9270):1777–89.

44.   Charles A Janeway J, Travers P, Walport M, Shlomchik MJ. Principles of innate and adaptive immunity. Immunobiology: The Immune System in Health and Disease 5th edition [Internet]. 2001 [cited 2022 Jun 23]; Available from: https://www.ncbi.nlm.nih.gov/books/NBK27090/

45.   Cui J, Chen Y, Wang HY, Wang RF. Mechanisms and pathways of innate immune activation and regulation in health and cancer. Hum Vaccin Immunother. 2014;10(11):3270–85.

46.   Boada-Romero E, Martinez J, Heckmann BL, Green DR. The clearance of dead cells by efferocytosis. Nat Rev Mol Cell Biol. 2020 Jul;21(7):398–414.

47.   Martin TR, Frevert CW. Innate Immunity in the Lungs. Proc Am Thorac Soc. 2005 Dec;2(5):403–11.

48.   Carty F, Mahon BP, English K. The influence of macrophages on mesenchymal stromal cell therapy: passive or aggressive agents? Clin Exp Immunol. 2017 Apr;188(1):1–11.

49.   Gwyer Findlay E, Hussell T. Macrophage-Mediated Inflammation and Disease: A Focus on the Lung. Mediators of Inflammation. 2012 Dec 12;2012:e140937.

50.   Lee H, Fessler MB, Qu P, Heymann J, Kopp JB. Macrophage polarization in innate immune responses contributing to pathogenesis of chronic kidney disease. BMC Nephrol. 2020 Jul 13;21:270.

51.   Spees JL, Lee RH, Gregory CA. Mechanisms of mesenchymal stem/stromal cell function. Stem Cell Research & Therapy. 2016 Aug 31;7(1):125.

52.   Song N, Scholtemeijer M, Shah K. Mesenchymal Stem Cell Immunomodulation: Mechanisms and Therapeutic Potential. Trends in Pharmacological Sciences. 2020 Sep;41(9):653–64.

53.   Gao F, Chiu SM, Motan D a. L, Zhang Z, Chen L, Ji HL, et al. Mesenchymal stem cells and immunomodulation: current status and future prospects. Cell Death Dis. 2016 Jan;7(1):e2062–e2062.

54.   Gonçalves F da C, Luk F, Korevaar SS, Bouzid R, Paz AH, López-Iglesias C, et al. Membrane particles generated from mesenchymal stromal cells modulate immune responses by selective targeting of pro-inflammatory monocytes. Sci Rep. 2017 Sep 21;7:12100.

55.   da Costa Gonçalves F, Korevaar SS, Ortiz Virumbrales M, Baan CC, Reinders MEJ, Merino A, et al. Mesenchymal Stromal Cell Derived Membrane Particles Are Internalized by Macrophages and Endothelial Cells Through Receptor-Mediated Endocytosis and Phagocytosis. Front Immunol. 2021;12:651109.

56.   Spaggiari GM, Capobianco A, Abdelrazik H, Becchetti F, Mingari MC, Moretta L. Mesenchymal stem cells inhibit natural killer–cell proliferation, cytotoxicity, and cytokine production: role of indoleamine 2,3-dioxygenase and prostaglandin E2. Blood. 2008 Feb 1;111(3):1327–33.

57. Spaggiari GM, Capobianco A, Becchetti S, Mingari MC, Moretta L. Mesenchymal stem cell-natural killer cell interactions: evidence that activated NK cells are capable of killing MSCs, whereas MSCs can inhibit IL-2-induced NK-cell proliferation. Blood. 2006 Feb 15;107(4):1484–90.

58. Mahmoudi M, Taghavi-Farahabadi M, Rezaei N, Hashemi SM. Comparison of the effects of adipose tissue mesenchymal stromal cell-derived exosomes with conditioned media on neutrophil function and apoptosis. International Immunopharmacology. 2019 Sep 1;74:105689.

59. Raffaghello L, Bianchi G, Bertolotto M, Montecucco F, Busca A, Dallegri F, et al. Human Mesenchymal Stem Cells Inhibit Neutrophil Apoptosis: A Model for Neutrophil Preservation in the Bone Marrow Niche. Stem Cells. 2008 Jan 1;26(1):151–62.

60. Spaggiari GM, Abdelrazik H, Becchetti F, Moretta L. MSCs inhibit monocyte-derived DC maturation and function by selectively interfering with the generation of immature DCs: central role of MSC-derived prostaglandin E2. Blood. 2009 Jun 25;113(26):6576–83.

61. Melief SM, Zwaginga JJ, Fibbe WE, Roelofs H. Adipose Tissue-Derived Multipotent Stromal Cells Have a Higher Immunomodulatory Capacity Than Their Bone Marrow-Derived Counterparts. Stem Cells Translational Medicine. 2013 Jun 1;2(6):455–63.

62. Hyvärinen K, Holopainen M, Skirdenko V, Ruhanen H, Lehenkari P, Korhonen M, et al. Mesenchymal Stromal Cells and Their Extracellular Vesicles Enhance the Anti-Inflammatory Phenotype of Regulatory Macrophages by Downregulating the Production of Interleukin (IL)-23 and IL-22. Frontiers in Immunology. 2018;9.

63. Aggarwal S, Pittenger MF. Human mesenchymal stem cells modulate allogeneic immune cell responses. Blood. 2005 Feb 15;105(4):1815–22.

64. Fu QL, Chow YY, Sun SJ, Zeng QX, Li HB, Shi JB, et al. Mesenchymal stem cells derived from human induced pluripotent stem cells modulate T-cell phenotypes in allergic rhinitis. Allergy. 2012;67(10):1215–22.

65.   Corcione A, Benvenuto F, Ferretti E, Giunti D, Cappiello V, Cazzanti F, et al. Human mesenchymal stem cells modulate B-cell functions. Blood. 2006 Jan 1;107(1):367–72.

66.   Ghannam S, Pène J, Torcy-Moquet G, Jorgensen C, Yssel H. Mesenchymal Stem Cells Inhibit Human Th17 Cell Differentiation and Function and Induce a T Regulatory Cell Phenotype. The Journal of Immunology. 2010 Jul 1;185(1):302–12.

67.   Asari S, Itakura S, Ferreri K, Liu CP, Kuroda Y, Kandeel F, et al. Mesenchymal stem cells suppress B-cell terminal differentiation. Experimental Hematology. 2009 May 1;37(5):604–15.

68.   Rosado MM, Bernardo ME, Scarsella M, Conforti A, Giorda E, Biagini S, et al. Inhibition of B-cell proliferation and antibody production by mesenchymal stromal cells is mediated by T cells. Stem Cells Dev. 2015 Jan 1;24(1):93–103.

69.   Crop MJ, Baan CC, Korevaar SS, IJzermans JNM, Pescatori M, Stubbs AP, et al. Inflammatory conditions affect gene expression and function of human adipose tissue-derived mesenchymal stem cells. Clinical and Experimental Immunology. 2010 Dec 1;162(3):474–86.

70.   Islam D, Huang Y, Fanelli V, Delsedime L, Wu S, Khang J, et al. Identification and Modulation of Microenvironment Is Crucial for Effective Mesenchymal Stromal Cell Therapy in Acute Lung Injury. Am J Respir Crit Care Med. 2019 May 15;199(10):1214–24.

71.   Dunbar H, Weiss DJ, Rolandsson Enes S, Laffey JG, English K. The Inflammatory Lung Microenvironment; a Key Mediator in MSC Licensing. Cells. 2021 Nov 2;10(11):2982.

72.   Caplan AI, Dennis JE. Mesenchymal stem cells as trophic mediators. J Cell Biochem. 2006 Aug 1;98(5):1076–84.

73.   Phinney DG, Hill K, Michelson C, DuTreil M, Hughes C, Humphries S, et al. Biological Activities Encoded by the Murine Mesenchymal Stem Cell Transcriptome Provide a Basis for Their Developmental Potential and Broad Therapeutic Efficacy. Stem Cells. 2006 Jan 1;24(1):186–98.

74. Park HW, Shin JS, Kim CW. Proteome of mesenchymal stem cells. Proteomics. 2007;7(16):2881–94.

75. Mazini L, Rochette L, Admou B, Amal S, Malka G. Hopes and Limits of Adipose-Derived Stem Cells (ADSCs) and Mesenchymal Stem Cells (MSCs) in Wound Healing. Int J Mol Sci. 2020 Feb 14;21(4):E1306.

76. Wu H, Mahato RI. Mesenchymal stem cell-based therapy for type 1 diabetes. Discov Med. 2014 Mar;17(93):139–43.

77. Wang X, Wang Y, Gou W, Lu Q, Peng J, Lu S. Role of mesenchymal stem cells in bone regeneration and fracture repair: a review. Int Orthop. 2013 Dec;37(12):2491–8.

78. Doyle LM, Wang MZ. Overview of Extracellular Vesicles, Their Origin, Composition, Purpose, and Methods for Exosome Isolation and Analysis. Cells. 2019 Jul 15;8(7):727.

79. Abreu SC, Lopes-Pacheco M, Weiss DJ, Rocco PRM. Mesenchymal Stromal Cell-Derived Extracellular Vesicles in Lung Diseases: Current Status and Perspectives. Frontiers in Cell and Developmental Biology. 2021;9.

80. Harrell CR, Jovicic N, Djonov V, Arsenijevic N, Volarevic V. Mesenchymal Stem Cell-Derived Exosomes and Other Extracellular Vesicles as New Remedies in the Therapy of Inflammatory Diseases. Cells. 2019 Dec 11;8(12):E1605.

81. Mead B, Tomarev S. Extracellular vesicle therapy for retinal diseases. Prog Retin Eye Res. 2020 Nov;79:100849.

82. Zhang W, Zhou X, Zhang H, Yao Q, Liu Y, Dong Z. Extracellular vesicles in diagnosis and therapy of kidney diseases. Am J Physiol Renal Physiol. 2016 Nov 1;311(5):F844–51.

83. Rahmani A, Saleki K, Javanmehr N, Khodaparast J, Saadat P, Nouri HR. Mesenchymal stem cell-derived extracellular vesicle-based therapies protect against coupled degeneration of the central nervous and vascular systems in stroke. Ageing Res Rev. 2020 Sep;62:101106.

84.   Barile L, Moccetti T, Marbán E, Vassalli G. Roles of exosomes in cardioprotection. Eur Heart J. 2017 May 7;38(18):1372–9.

85.   Zhang S, Yang J, Shen L. Extracellular vesicle-mediated regulation of tumor angiogenesis- implications for anti-angiogenesis therapy. J Cell Mol Med. 2021 Mar;25(6):2776–85.

86.   Mulcahy LA, Pink RC, Carter DRF. Routes and mechanisms of extracellular vesicle uptake. J Extracell Vesicles. 2014 Aug 4;3:10.3402/jev.v3.24641.

87.   EL Andaloussi S, Mäger I, Breakefield XO, Wood MJA. Extracellular vesicles: biology and emerging therapeutic opportunities. Nat Rev Drug Discov. 2013 May;12(5):347–57.

88.   Huang JY XM; Xu, Y; Xu, CC; Lin, X; Ye, FB; C, Y; L, FY; Systemic Administration of Exosomes Released from Mesenchymal Stromal Cells Attenuates Apoptosis, Inflammation, and Promotes Angiogenesis after Spinal Cord Injury in Rats. Journal of Neurotrauma. 2017 Dec 15;34(24):3388–96.

89.   Zhang S, Chuah SJ, Lai RC, Hui JHP, Lim SK, Toh WS. MSC exosomes mediate cartilage repair by enhancing proliferation, attenuating apoptosis and modulating immune reactivity. Biomaterials. 2018 Feb 1;156:16–27.

90.   Camussi G, Deregibus MC, Cantaluppi V. Role of stem-cell-derived microvesicles in the paracrine action of stem cells. Biochemical Society Transactions. 2013 Jan 29;41(1):283–7.

91.   Zheng X, Hermann DM, Bähr M, Doeppner TR. The role of small extracellular vesicles in cerebral and myocardial ischemia—Molecular signals, treatment targets, and future clinical translation. Stem Cells. 2021 Apr 1;39(4):403–13.

92.   Xu HK, Chen LJ, Zhou SN, Li YF, Xiang C. Multifunctional role of microRNAs in mesenchymal stem cell-derived exosomes in treatment of diseases. World J Stem Cells. 2020 Nov 26;12(11):1276–94.

93. Yin Z, Han Z, Hu T, Zhang S, Ge X, Huang S, et al. Neuron-derived exosomes with high miR-21-5p expression promoted polarization of M1 microglia in culture. Brain Behav Immun. 2020 Jan;83:270–82.

94. Long X, Yao X, Jiang Q, Yang Y, He X, Tian W, et al. Astrocyte-derived exosomes enriched with miR-873a-5p inhibit neuroinflammation via microglia phenotype modulation after traumatic brain injury. J Neuroinflammation. 2020 Mar 19;17:89.

95. Casado-Díaz A, Quesada-Gómez JM, Dorado G. Extracellular Vesicles Derived From Mesenchymal Stem Cells (MSC) in Regenerative Medicine: Applications in Skin Wound Healing. Frontiers in Bioengineering and Biotechnology. 2020;8.

96. Hsu YW YT; Yu, TH; Wei, YH. Mitochondria in mesenchymal stem cell biology and cell therapy: From cellular differentiation to mitochondrial transfer. Seminars in Cell & Developmental Biology. 2016 Apr 1;52:119–31.

97. Mohammadalipour A, Dumbali SP, Wenzel PL. Mitochondrial Transfer and Regulators of Mesenchymal Stromal Cell Function and Therapeutic Efficacy. Front Cell Dev Biol. 2020 Dec 7;8:603292.

98. Islam MND Shonit R; Emin, Memet T; Wei, Michelle; Sun, Li; Westphalen, Kristin; Rowlands, David J; Quadri, Sadiqa K; Bhattacharya, Sunita; Bhattacharya, Jahar. Mitochondrial transfer from bone-marrow-derived stromal cells to pulmonary alveoli protects against acute lung injury. Nat Med. 2012 Apr 15;18(5):759–65.

99. Li H, Wang C, He T, Zhao T, Chen YY, Shen YL, et al. Mitochondrial Transfer from Bone Marrow Mesenchymal Stem Cells to Motor Neurons in Spinal Cord Injury Rats via Gap Junction. Theranostics. 2019;9(7):2017–35.

100. Ahmad T, Mukherjee S, Pattnaik B, Kumar M, Singh S, Kumar M, et al. Miro1 regulates intercellular mitochondrial transport & enhances mesenchymal stem cell rescue efficacy. EMBO J. 2014 May 2;33(9):994–1010.

101. Boukelmoune N, Chiu GS, Kavelaars A, Heijnen CJ. Mitochondrial transfer from mesenchymal stem cells to neural stem cells protects against the

neurotoxic effects of cisplatin. Acta Neuropathologica Communications. 2018 Dec 12;6(1):139.

102.   Yasuda KP Hyeong Cheon;; Ratliff, Brian; Addabbo, Francesco; Hatzopoulos, Antonis K; Chander, Praveen; Goligorsky, Michael S. Adriamycin Nephropathy: A Failure of Endothelial Progenitor Cell-Induced Repair. The American Journal of Pathology. 2010 Apr 1;176(4):1685–95.

103.   Yuan Y, Yuan L, Li L, Liu F, Liu J, Chen Y, et al. Mitochondrial transfer from mesenchymal stem cells to macrophages restricts inflammation and alleviates kidney injury in diabetic nephropathy mice via PGC-1α activation. Stem Cells. 2021 Jul;39(7):913–28.

104.   Jackson MV, Morrison TJ, Doherty DF, McAuley DF, Matthay MA, Kissenpfennig A, et al. Mitochondrial Transfer via Tunneling Nanotubes is an Important Mechanism by Which Mesenchymal Stem Cells Enhance Macrophage Phagocytosis in the In Vitro and In Vivo Models of ARDS. Stem Cells. 2016 Aug;34(8):2210–23.

105.   Piekarska K, Urban-Wójciuk Z, Kurkowiak M, Pelikant-Małecka I, Schumacher A, Sakowska J, et al. Mesenchymal stem cells transfer mitochondria to allogeneic Tregs in an HLA-dependent manner improving their immunosuppressive activity. Nat Commun. 2022 Dec;13(1):856.

106.   Court AC, Le-Gatt A, Luz-Crawford P, Parra E, Aliaga-Tobar V, Bátiz LF, et al. Mitochondrial transfer from MSCs to T cells induces Treg differentiation and restricts inflammatory response. EMBO Rep. 2020 Feb 5;21(2):e48052.

107.   Liu K, Ji K, Guo L, Wu W, Lu H, Shan P, et al. Mesenchymal stem cells rescue injured endothelial cells in an in vitro ischemia-reperfusion model via tunneling nanotube like structure-mediated mitochondrial transfer. Microvasc Res. 2014 Mar;92:10–8.

108.   Yang F, Zhang Y, Liu S, Xiao J, He Y, Shao Z, et al. Tunneling Nanotube-Mediated Mitochondrial Transfer Rescues Nucleus Pulposus Cells from Mitochondrial Dysfunction and Apoptosis. Oxid Med Cell Longev. 2022 Mar 4;2022:3613319.

109.   Lu J, Zheng X, Li F, Yu Y, Chen Z, Liu Z, et al. Tunneling nanotubes promote intercellular mitochondria transfer followed by increased invasiveness in bladder cancer cells. Oncotarget. 2017 Jan 17;8(9):15539–52.

110.   Gerdes HH, Bukoreshtliev NV, Barroso JFV. Tunneling nanotubes: A new route for the exchange of components between animal cells. FEBS Letters. 2007 May 22;581(11):2194–201.

111.   Acquistapace A, Bru T, Lesault PF, Figeac F, Coudert AE, le Coz O, et al. Human Mesenchymal Stem Cells Reprogram Adult Cardiomyocytes Toward a Progenitor-Like State Through Partial Cell Fusion and Mitochondria Transfer. Stem Cells. 2011 May 1;29(5):812–24.

112.   Norris RP. Transfer of mitochondria and endosomes between cells by gap junction internalization. Traffic. 2021 Jun;22(6):174–9.

113.   Phinney DG, Di Giuseppe M, Njah J, Sala E, Shiva S, St Croix CM, et al. Mesenchymal stem cells use extracellular vesicles to outsource mitophagy and shuttle microRNAs. Nat Commun. 2015 Oct 7;6:8472.

114.   Weiss DJ, English K, Krasnodembskaya A, Isaza-Correa JM, Hawthorne IJ, Mahon BP. The Necrobiology of Mesenchymal Stromal Cells Affects Therapeutic Efficacy. Frontiers in Immunology. 2019;10.

115.   Shi X, Zhao M, Fu C, Fu A. Intravenous administration of mitochondria for treating experimental Parkinson's disease. Mitochondrion. 2017 May;34:91–100.

116.   de Witte SFH, Luk F, Sierra Parraga JM, Gargesha M, Merino A, Korevaar SS, et al. Immunomodulation By Therapeutic Mesenchymal Stromal Cells (MSC) Is Triggered Through Phagocytosis of MSC By Monocytic Cells. Stem Cells. 2018 Apr 1;36(4):602–15.

117.   Braza F, Dirou S, Forest V, Sauzeau V, Hassoun D, Chesné J, et al. Mesenchymal Stem Cells Induce Suppressive Macrophages Through Phagocytosis in a Mouse Model of Asthma. Stem Cells. 2016 Jul 1;34(7):1836–45.

118.   Pang SHM, D'Rozario J, Mendonca S, Bhuvan T, Payne NL, Zheng D, et al. Mesenchymal stromal cell apoptosis is required for their therapeutic function. Nat Commun. 2021 Nov 11;12(1):6495.

119.   Galleu A, Riffo-Vasquez Y, Trento C, Lomas C, Dolcetti L, Cheung TS, et al. Apoptosis in mesenchymal stromal cells induces in vivo recipient-mediated immunomodulation. Sci Transl Med. 2017 Nov 15;9(416):eaam7828.

120.   Ghahremani Piraghaj M, Soudi S, Ghanbarian H, Bolandi Z, Namaki S, Hashemi SM. Effect of efferocytosis of apoptotic mesenchymal stem cells (MSCs) on C57BL/6 peritoneal macrophages function. Life Sciences. 2018 Nov 1;212:203–12.

121.   Faiella W, Atoui R. Immunotolerant Properties of Mesenchymal Stem Cells: Updated Review. Stem Cells Int. 2016;2016:1859567.

122.   Müller L, Tunger A, Wobus M, von Bonin M, Towers R, Bornhäuser M, et al. Immunomodulatory Properties of Mesenchymal Stromal Cells: An Update. Frontiers in Cell and Developmental Biology. 2021;9.

123.   Wu X, Jiang J, Gu Z, Zhang J, Chen Y, Liu X. Mesenchymal stromal cell therapies: immunomodulatory properties and clinical progress. Stem Cell Research & Therapy. 2020 Aug 8;11(1):345.

124.   Ashmore-Harris C, Iafrate M, Saleem A, Fruhwirth GO. Non-invasive Reporter Gene Imaging of Cell Therapies, including T Cells and Stem Cells. Mol Ther. 2020 Jun 3;28(6):1392–416.

125.   Mousavinejad M, Skidmore S, Barone FG, Tyers P, Pisupati V, Poptani H, et al. Assessing Human Embryonic Stem Cell-Derived Dopaminergic Neuron Progenitor Transplants Using Non-invasive Imaging Techniques. Mol Imaging Biol. 2020 Oct;22(5):1244–54.

126.   Progatzky F, Dallman MJ, Lo Celso C. From seeing to believing: labelling strategies for in vivo cell-tracking experiments. Interface Focus. 2013 Jun 6;3(3):20130001.

127.   Masterson CH, Curley GF, Laffey JG. Modulating the distribution and fate of exogenously delivered MSCs to enhance therapeutic potential: knowns and unknowns. Intensive Care Med Exp. 2019 Jul 25;7(Suppl 1):41.

128.   Taylor A, Wilson KM, Murray P, Fernig DG, Lévy R. Long-term tracking of cells using inorganic nanoparticles as contrast agents: are we there yet? Chem Soc Rev. 2012 Apr 7;41(7):2707–17.

129.   Sakuma T, Barry MA, Ikeda Y. Lentiviral vectors: basic to translational. Biochem J. 2012 May 1;443(3):603–18.

130.   Mezzanotte L, van 't Root M, Karatas H, Goun EA, Löwik CWGM. In Vivo Molecular Bioluminescence Imaging: New Tools and Applications. Trends Biotechnol. 2017 Jul;35(7):640–52.

131.   de Almeida PE, van Rappard JRM, Wu JC. In vivo bioluminescence for tracking cell fate and function. American Journal of Physiology-Heart and Circulatory Physiology. 2011 Sep 1;301(3):H663–71.

132.   Finkelshtein D, Werman A, Novick D, Barak S, Rubinstein M. LDL receptor and its family members serve as the cellular receptors for vesicular stomatitis virus. Proc Natl Acad Sci U S A. 2013 Apr 30;110(18):7306–11.

133.   Greber UF, Gomez-Gonzalez A. Adenovirus - a blueprint for gene delivery. Curr Opin Virol. 2021 Jun;48:49–56.

134.   Scarfe L, Brillant N, Kumar JD, Ali N, Alrumayh A, Amali M, et al. Preclinical imaging methods for assessing the safety and efficacy of regenerative medicine therapies. npj Regen Med. 2017 Oct 19;2(1):1–13.

135.   Kim JE, Kalimuthu S, Ahn BC. In Vivo Cell Tracking with Bioluminescence Imaging. Nucl Med Mol Imaging. 2015 Mar;49(1):3–10.

136.   Zambito G, Chawda C, Mezzanotte L. Emerging tools for bioluminescence imaging. Curr Opin Chem Biol. 2021 Aug;63:86–94.

137.   Freitas GP, Lopes HB, Souza ATP, Oliveira PGFP, Almeida ALG, Souza LEB, et al. Cell Therapy: Effect of Locally Injected Mesenchymal Stromal Cells Derived from Bone Marrow or Adipose Tissue on Bone Regeneration of Rat Calvarial Defects. Sci Rep. 2019 Sep 17;9(1):13476.

138.   Iwano S, Sugiyama M, Hama H, Watakabe A, Hasegawa N, Kuchimaru T, et al. Single-cell bioluminescence imaging of deep tissue in freely moving animals. Science. 2018 Feb 23;359(6378):935–9.

139.   Nguyen PK, Riegler J, Wu JC. Stem cell imaging: From bed to benchside. Cell stem cell. 2014 Apr 3;14(4):431.

140.   Xi D, Dong S, Meng X, Lu Q, Meng L, Ye J. Gold nanoparticles as computerized tomography (CT) contrast agents. RSC Adv. 2012 Nov 19;2(33):12515–24.

141.   Kim T, Lee N, Arifin DR, Shats I, Janowski M, Walczak P, et al. In Vivo Micro-CT Imaging of Human Mesenchymal Stem Cells Labeled with Gold-Poly-l-Lysine Nanocomplexes. Advanced Functional Materials. 2017 Jan;27(3):1604213.

142.   Ashton JR, West JL, Badea CT. In vivo small animal micro-CT using nanoparticle contrast agents. Frontiers in Pharmacology. 2015 Nov;6:256.

143.   Cole LE, Ross RD, Tilley JM, Vargo-Gogola T, Roeder RK. Gold nanoparticles as contrast agents in x-ray imaging and computed tomography. Nanomedicine (Lond). 2015 Jan;10(2):321–41.

144.   Xu C, Tung GA, Sun S. Size and Concentration Effect of Gold Nanoparticles on X-ray Attenuation As Measured on Computed Tomography. Chem Mater. 2008 Jul 8;20(13):4167–9.

145.   Bernstein AL, Dhanantwari A, Jurcova M, Cheheltani R, Naha PC, Ivanc T, et al. Improved sensitivity of computed tomography towards iodine and gold nanoparticle contrast agents via iterative reconstruction methods. Scientific Reports [Internet]. 2016 [cited 2021 Nov 16];6. Available from: https://www.mendeley.com/catalogue/cc68deba-cad8-36ea-bccb-2770049f36df/

146.   Steinberg I, Huland DM, Vermesh O, Frostig HE, Tummers WS, Gambhir SS. Photoacoustic clinical imaging. Photoacoustics. 2019 Jun 8;14:77–98.

147. Lin L, Wang LV. Photoacoustic Imaging. Adv Exp Med Biol. 2021;3233:147–75.

148. Weber J, Beard PC, Bohndiek SE. Contrast agents for molecular photoacoustic imaging. Nat Methods. 2016 Jul 28;13(8):639–50.

149. Comenge J, Fragueiro O, Sharkey J, Taylor A, Held M, Burton NC, et al. Preventing plasmon coupling between gold nanorods improves the sensitivity of photoacoustic detection of labelled stem cells in vivo. :25.

150. Comenge J, Sharkey J, Fragueiro O, Wilm B, Brust M, Murray P, et al. Multimodal cell tracking from systemic administration to tumour growth by combining gold nanorods and reporter genes. Elife. 2018 Jun 27;7:e33140.

151. Li W, Chen X. Gold nanoparticles for photoacoustic imaging. Nanomedicine (Lond). 2015 Jan 1;10(2):299–320.

152. Dhada KS, Hernandez DS, Suggs LJ. In Vivo Photoacoustic Tracking of Mesenchymal Stem Cell Viability. ACS Nano. 2019 Jul 23;13(7):7791–9.

153. Miao Y, Chen Z, Li SC. Functional endoscopy techniques for tracking stem cell fate. Quant Imaging Med Surg. 2019 Mar;9(3):510–20.

154. Rajendran RL, Jogalekar MP, Gangadaran P, Ahn BC. Noninvasive in vivo cell tracking using molecular imaging: A useful tool for developing mesenchymal stem cell-based cancer treatment. World J Stem Cells. 2020 Dec 26;12(12):1492–510.

155. Moreira ML, da Costa Medeiros P, de Souza SAL, Gutfilen B, Rosado-de-Castro PH. In Vivo Tracking of Cell Therapies for Cardiac Diseases with Nuclear Medicine. Stem Cells Int. 2016;2016:3140120.

156. Zheng Y, Huang J, Zhu T, Li R, Wang Z, Ma F, et al. Stem Cell Tracking Technologies for Neurological Regenerative Medicine Purposes. Stem Cells Int. 2017;2017:2934149.

157. Acton PD, Zhou R. Imaging reporter genes for cell tracking with PET and SPECT. Q J Nucl Med Mol Imaging. 2005 Dec;49(4):349–60.

158. Wallace PK, Palmer LD, Perry-Lalley D, Bolton ES, Alexander RB, Horan PK, et al. Mechanisms of adoptive immunotherapy: improved methods for in vivo tracking of tumor-infiltrating lymphocytes and lymphokine-activated killer cells. Cancer Res. 1993 May 15;53(10 Suppl):2358–67.

159. Srivastava AK, Kadayakkara DK, Bar-Shir A, Gilad AA, McMahon MT, Bulte JWM. Advances in using MRI probes and sensors for in vivo cell tracking as applied to regenerative medicine. Disease Models & Mechanisms. 2015 Apr 1;8(4):323–36.

160. Kircher MF, Gambhir SS, Grimm J. Noninvasive cell-tracking methods. Nat Rev Clin Oncol. 2011 Nov;8(11):677–88.

161. Wielpütz M, Kauczor HU. MRI of the lung: state of the art. Diagn Interv Radiol. 2012 Aug;18(4):344–53.

162. Fischer UM, Harting MT, Jimenez F, Monzon-Posadas WO, Xue H, Savitz SI, et al. Pulmonary passage is a major obstacle for intravenous stem cell delivery: the pulmonary first-pass effect. Stem Cells Dev. 2009 Jun;18(5):683–92.

163. van Zuylen J. The microscopes of Antoni van Leeuwenhoek. J Microsc. 1981 Mar;121(Pt 3):309–28.

164. Yuste R. Fluorescence microscopy today. Nat Methods. 2005 Dec;2(12):902–4.

165. Magidson V, Khodjakov A. Chapter 23 - Circumventing Photodamage in Live-Cell Microscopy. In: Sluder G, Wolf DE, editors. Methods in Cell Biology. Academic Press; 2013. p. 545–60. (Digital Microscopy; vol. 114).

166. Bayguinov PO, Oakley DM, Shih CC, Geanon DJ, Joens MS, Fitzpatrick JAJ. Modern Laser Scanning Confocal Microscopy. Curr Protoc Cytom. 2018 Jul;85(1):e39.

167. Rodríguez C, Ji N. One wavelength to excite them all: deep tissue imaging going multicolor. Trends in Neurosciences. 2021 Sep 1;44(9):689–91.

168. Muntifering M, Castranova D, Gibson GA, Meyer E, Kofron M, Watson AM. Clearing for Deep Tissue Imaging. Curr Protoc Cytom. 2018 Oct;86(1):e38.

169. Richardson DS, Lichtman JW. Clarifying Tissue Clearing. Cell. 2015 Jul 16;162(2):246–57.

170. Ariel P. A beginner's guide to tissue clearing. The International Journal of Biochemistry & Cell Biology. 2017 Mar 1;84:35–9.

171. Li W, Germain RN, Gerner MY. High-dimensional cell-level analysis of tissues with Ce3D multiplex volume imaging. Nat Protoc. 2019 Jun;14(6):1708–33.

172. Tian T, Yang Z, Li X. Tissue clearing technique: Recent progress and biomedical applications. J Anat. 2021 Feb;238(2):489–507.

173. Qi Y, Yu T, Xu J, Wan P, Ma Y, Zhu J, et al. FDISCO: Advanced solvent-based clearing method for imaging whole organs. Sci Adv. 2019 Jan;5(1):eaau8355.

174. Yu T, Zhu J, Li D, Zhu D. Physical and chemical mechanisms of tissue optical clearing. iScience. 2021 Mar 19;24(3):102178.

175. Molbay, M; Ilgin KZ; Ivilinv, TM, Ohn, TL, Ertürk, Ali. A guidebook for DISCO tissue clearing. Molecular Systems Biology. 2021 Mar;17(3):e9807.

176. Pan C, Cai R, Quacquarelli FP, Ghasemigharagoz A, Lourbopoulos A, Matryba P, et al. Shrinkage-mediated imaging of entire organs and organisms using uDISCO. Nat Methods. 2016 Oct;13(10):859–67.

177. Ueda HR, Ertürk A, Chung K, Gradinaru V, Chédotal A, Tomancak P, et al. Tissue clearing and its applications in neuroscience. Nat Rev Neurosci. 2020 Feb;21(2):61–79.

178. Klingberg A, Hasenberg A, Ludwig-Portugall I, Medyukhina A, Männ L, Brenzel A, et al. Fully Automated Evaluation of Total Glomerular Number and Capillary Tuft Size in Nephritic Kidneys Using Lightsheet Microscopy. JASN. 2017 Feb 1;28(2):452–9.

179.   Hahn C, Becker K, Saghafi S, Pende M, Avdibašić A, Foroughipour M, et al. High-resolution imaging of fluorescent whole mouse brains using stabilised organic media (sDISCO). J Biophotonics. 2019 Aug;12(8):e201800368.

180.   Tainaka K, Kuno A, Kubota SI, Murakami T, Ueda HR. Chemical Principles in Tissue Clearing and Staining Protocols for Whole-Body Cell Profiling. Annu Rev Cell Dev Biol. 2016 Oct 6;32(1):713–41.

181.   Susaki EA, Tainaka K, Perrin D, Kishino F, Tawara T, Watanabe TM, et al. Whole-brain imaging with single-cell resolution using chemical cocktails and computational analysis. Cell. 2014 Apr 24;157(3):726–39.

182.   Kubota SI, Takahashi K, Nishida J, Morishita Y, Ehata S, Tainaka K, et al. Whole-Body Profiling of Cancer Metastasis with Single-Cell Resolution. Cell Rep. 2017 Jul 5;20(1):236–50.

183.   Heslop JA, Hammond TG, Santeramo I, Tort Piella A, Hopp I, Zhou J, et al. Concise review: workshop review: understanding and assessing the risks of stem cell-based therapies. Stem Cells Transl Med. 2015 Apr;4(4):389–400.

184.   Sharkey J, Scarfe L, Santeramo I, Garcia-Finana M, Park BK, Poptani H, et al. Imaging technologies for monitoring the safety, efficacy and mechanisms of action of cell-based regenerative medicine therapies in models of kidney disease. Eur J Pharmacol. 2016 Nov 5;790:74–82.

185.   James ML, Gambhir SS. A Molecular Imaging Primer: Modalities, Imaging Agents, and Applications. Physiological Reviews. 2012 Apr;92(2):897–965.

186.   Nguyen PK, Riegler J, Wu JC. Stem cell imaging: from bench to bedside. Cell Stem Cell. 2014 Apr 3;14(4):431–44.

187.   The Production of Sound by Radiant Energy 1. Nature. 1881 May 1;24(602):42–4.

188.   Bernstein AL, Dhanantwari A, Jurcova M, Cheheltani R, Naha PC, Ivanc T, et al. Improved sensitivity of computed tomography towards iodine and gold

nanoparticle contrast agents via iterative reconstruction methods. Sci Rep. 2016 May 17;6(1):26177.

189. Ntziachristos V, Razansky D. Molecular imaging by means of multispectral optoacoustic tomography (MSOT). Chem Rev. 2010 May 12;110(5):2783–94.

190. Comenge J, Fragueiro O, Sharkey J, Taylor A, Held M, Burton NC, et al. Preventing Plasmon Coupling between Gold Nanorods Improves the Sensitivity of Photoacoustic Detection of Labeled Stem Cells in Vivo. ACS Nano. 2016 Jul;10(7):7106–16.

191. Wang S, You Q, Wang J, Song Y, Cheng Y, Wang Y, et al. MSOT/CT/MR imaging-guided and hypoxia-maneuvered oxygen self-supply radiotherapy based on one-pot MnO2-mSiO2@Au nanoparticles. Nanoscale. 2019 Mar 28;11(13):6270–84.

192. Comenge J, Sharkey J, Fragueiro O, Wilm B, Brust M, Murray P, et al. Multimodal cell tracking from systemic administration to tumour growth by combining gold nanorods and reporter genes. Schekman R, editor. eLife. 2018 Jun 27;7:e33140.

193. iThera Medical. MSOT User Guide (User manual - Part 3, Version 3.8). 2017.

194. Yang SA, Choi S, Jeon SM, Yu J. Silica nanoparticle stability in biological media revisited. Sci Rep. 2018 Jan 9;8(1):185.

195. Weissleder R. A clearer vision for in vivo imaging. Nat Biotechnol. 2001 Apr;19(4):316–7.

196. Ma X, Wu Y, Jin S, Tian Y, Zhang X, Zhao Y, et al. Gold nanoparticles induce autophagosome accumulation through size-dependent nanoparticle uptake and lysosome impairment. ACS Nano. 2011 Nov 22;5(11):8629–39.

197. Schütz I, Lopez-Hernandez T, Gao Q, Puchkov D, Jabs S, Nordmeyer D, et al. Lysosomal Dysfunction Caused by Cellular Accumulation of Silica Nanoparticles *. Journal of Biological Chemistry. 2016 Jul 1;291(27):14170–84.

198.   Nam SY, Ricles LM, Suggs LJ, Emelianov SY. In vivo Ultrasound and Photoacoustic Monitoring of Mesenchymal Stem Cells Labeled with Gold Nanotracers. Rameshwar P, editor. PLoS ONE. 2012 May 16;7(5):e37267.

199.   Ricles LM, Nam SY, Treviño EA, Emelianov SY, Suggs LJ. A dual gold nanoparticle system for mesenchymal stem cell tracking. J Mater Chem B. 2014 Nov 5;2(46):8220–30.

200.   Yu C, Chen Z, Li X, Bao H, Wang Y, Zhang B, et al. pH-Triggered Aggregation of Gold Nanoparticles for Enhanced Labeling and Long-Term CT Imaging Tracking of Stem Cells in Pulmonary Fibrosis Treatment. Small. 2021 Aug;17(33):2101861.

201.   Bao H, Xia Y, Yu C, Ning X, Liu X, Fu H, et al. CT/Bioluminescence Dual-Modal Imaging Tracking of Mesenchymal Stem Cells in Pulmonary Fibrosis. Small. 2019 Nov;15(46):1904314.

202.   Yu C, Bao H, Chen Z, Li X, Liu X, Wang W, et al. Enhanced and long-term CT imaging tracking of transplanted stem cells labeled with temperature-responsive gold nanoparticles. J Mater Chem B. 2021 Apr 1;9(12):2854–65.

203.   Ning X, Bao H, Liu X, Fu H, Wang W, Huang J, et al. Long-term in vivo CT tracking of mesenchymal stem cells labeled with Au@BSA@PLL nanotracers. Nanoscale. 2019 Nov 7;11(43):20932–41.

204.   Astolfo A, Arfelli F, Schültke E, James S, Mancini L, Menk RH. A detailed study of gold-nanoparticle loaded cells using X-ray based techniques for cell-tracking applications with single-cell sensitivity. Nanoscale. 2013 Mar 28;5(8):3337–45.

205.   Mok PL, Leow SN, Koh AEH, Mohd Nizam HH, Ding SLS, Luu C, et al. Micro-Computed Tomography Detection of Gold Nanoparticle-Labelled Mesenchymal Stem Cells in the Rat Subretinal Layer. Int J Mol Sci. 2017 Feb 8;18(2):E345.

206.   Zong C, Bronckaers A, Vande Velde G, Willems G, Cadenas de Llano-Pérula M. In Vivo Micro-Computerized Tomography Tracking of Human Periodontal Ligament Stem Cells Labeled with Gold Nanocomplexes. Adv Healthc Mater. 2022 Jan;11(1):e2101133.

207.   Huang J, Huang J, Ning X, Luo W, Chen M, Wang Z, et al. CT/NIRF dual-modal imaging tracking and therapeutic efficacy of transplanted mesenchymal stem cells labeled with Au nanoparticles in silica-induced pulmonary fibrosis. J Mater Chem B. 2020 Feb;8(8):1713–27.

208.   Menk RH, Schültke E, Hall C, Arfelli F, Astolfo A, Rigon L, et al. Gold nanoparticle labeling of cells is a sensitive method to investigate cell distribution and migration in animal models of human disease. Nanomedicine. 2011 Oct;7(5):647–54.

209.   Astolfo A, Schültke E, Menk RH, Kirch RD, Juurlink BHJ, Hall C, et al. In vivo visualization of gold-loaded cells in mice using x-ray computed tomography. Nanomedicine. 2013 Feb;9(2):284–92.

210.   Silva LHA, da Silva JR, Ferreira GA, Silva RC, Lima ECD, Azevedo RB, et al. Labeling mesenchymal cells with DMSA-coated gold and iron oxide nanoparticles: assessment of biocompatibility and potential applications. Journal of Nanobiotechnology. 2016 Jul 18;14(1):59.

211.   Das M, Yi DK, An SSA. Analyses of protein corona on bare and silica-coated gold nanorods against four mammalian cells. IJN. 2015 Feb 20;10(1):1521–45.

212.   Sakhtianchi R, Minchin RF, Lee KB, Alkilany AM, Serpooshan V, Mahmoudi M. Exocytosis of nanoparticles from cells: Role in cellular retention and toxicity. Advances in Colloid and Interface Science. 2013 Dec 1;201–202:18–29.

213.   Chithrani BD, Chan WCW. Elucidating the Mechanism of Cellular Uptake and Removal of Protein-Coated Gold Nanoparticles of Different Sizes and Shapes. Nano Lett. 2007 Jun 1;7(6):1542–50.

214.   Huang J, Bao H, Li X, Zhang Z. In vivo CT imaging tracking of stem cells labeled with Au nanoparticles. View. 2021 Jul;(20200119).

215.   Cartiera MS, Johnson KM, Rajendran V, Caplan MJ, Saltzman WM. The Uptake and Intracellular Fate of PLGA Nanoparticles in Epithelial Cells. Biomaterials. 2009 May;30(14):2790–8.

216.	Jiang W, Kim BYS, Rutka JT, Chan WCW. Nanoparticle-mediated cellular response is size-dependent. Nat Nanotechnol. 2008 Mar;3(3):145–50.

217.	Galper MW, Saung MT, Fuster V, Roessl E, Thran A, Proksa R, et al. Effect of computed tomography scanning parameters on gold nanoparticle and iodine contrast. Invest Radiol. 2012 Aug;47(8):475–81.

218.	Galper MW, Saung MT, Fuster V, Roessl E, Thran A, Proksa R, et al. Effect of computed tomography scanning parameters on gold nanoparticle and iodine contrast. Invest Radiol. 2012 Aug;47(8):475–81.

219.	Cormode DP, Naha PC, Fayad ZA. Nanoparticle Contrast Agents for Computed Tomography: A Focus on Micelles. Contrast Media Mol Imaging. 2014 Jan;9(1):37–52.

220.	Kolios G, Moodley Y. Introduction to Stem Cells and Regenerative Medicine. Respiration. 2013;85(1):3–10.

221.	Hoogduijn MJ, Lombardo E. Mesenchymal Stromal Cells Anno 2019: Dawn of the Therapeutic Era? Concise Review. STEM CELLS Translational Medicine. 2019;8(11):1126–34.

222.	Eggenhofer E, Benseler V, Kroemer A, Popp FC, Geissler EK, Schlitt HJ, et al. Mesenchymal stem cells are short-lived and do not migrate beyond the lungs after intravenous infusion. Front Immunol. 2012;3:297.

223.	Santeramo I, Herrera Perez Z, Illera A, Taylor A, Kenny S, Murray P, et al. Human Kidney-Derived Cells Ameliorate Acute Kidney Injury Without Engrafting into Renal Tissue. STEM CELLS Translational Medicine. 2017;6(5):1373–84.

224.	Moll G, Ankrum JA, Olson SD, Nolta JA. Improved MSC Minimal Criteria to Maximize Patient Safety: A Call to Embrace Tissue Factor and Hemocompatibility Assessment of MSC Products. Stem Cells Translational Medicine. 2022 Feb 8;szab005.

225.	Lukomska B, Stanaszek L, Zuba-Surma E, Legosz P, Sarzynska S, Drela K. Challenges and Controversies in Human Mesenchymal Stem Cell Therapy. Stem Cells International. 2019 Apr 9;2019:1–10.

226. Lee RH, Pulin AA, Seo MJ, Kota DJ, Ylostalo J, Larson BL, et al. Intravenous hMSCs improve myocardial infarction in mice because cells embolized in lung are activated to secrete the anti-inflammatory protein TSG-6. Cell Stem Cell. 2009 Jul 2;5(1):54–63.

227. Krueger TEG, Thorek DLJ, Denmeade SR, Isaacs JT, Brennen WN. Concise Review: Mesenchymal Stem Cell-Based Drug Delivery: The Good, the Bad, the Ugly, and the Promise. STEM CELLS Translational Medicine. 2018;7(9):651–63.

228. Molbay M, Kolabas ZI, Todorov MI, Ohn TL, Ertürk A. A guidebook for DISCO tissue clearing. Mol Syst Biol. 2021 Mar;17(3):e9807.

229. Zhao J, Lai HM, Qi Y, He D, Sun H. Current Status of Tissue Clearing and the Path Forward in Neuroscience. ACS Chem Neurosci. 2021 Jan 6;12(1):5–29.

230. Kolesová H, Olejníčková V, Kvasilová A, Gregorovičová M, Sedmera D. Tissue clearing and imaging methods for cardiovascular development. iScience. 2021 Apr 23;24(4):102387.

231. Weiss KR, Voigt FF, Shepherd DP, Huisken J. Tutorial: practical considerations for tissue clearing and imaging. Nat Protoc. 2021 Jun;16(6):2732–48.

232. Zhan Y, Wu H, Liu L, Lin J, Zhang S. Organic solvent-based tissue clearing techniques and their applications. J Biophotonics. 2021 Jun;14(6):e202000413.

233. Pan C, Schoppe O, Parra-Damas A, Cai R, Todorov MI, Gondi G, et al. Deep Learning Reveals Cancer Metastasis and Therapeutic Antibody Targeting in the Entire Body. Cell. 2019 Dec 12;179(7):1661-1676.e19.

234. Sun Q, Picascia T, Khan AUM, Brenna C, Heuveline V, Schmaus A, et al. Application of ethyl cinnamate based optical tissue clearing and expansion microscopy combined with retrograde perfusion for 3D lung imaging. Exp Lung Res. 2020 Dec;46(10):393–408.

235.   Honeycutt SE, O'Brien LL. Injection of Evans blue dye to fluorescently label and image intact vasculature. BioTechniques. 2021 Mar 1;70(3):181–5.

236.   Susaki EA, Tainaka K, Perrin D, Yukinaga H, Kuno A, Ueda HR. Advanced CUBIC protocols for whole-brain and whole-body clearing and imaging. Nat Protoc. 2015 Nov;10(11):1709–27.

237.   Masselink W, Reumann D, Murawala P, Pasierbek P, Taniguchi Y, Bonnay F, et al. Broad applicability of a streamlined ethyl cinnamate-based clearing procedure. Development. 2019 Feb 1;146(3):dev166884.

238.   Participation E. Animals (Scientific Procedures) Act 1986 [Internet]. Statute Law Database; [cited 2022 Jan 30]. Available from: https://www.legislation.gov.uk/ukpga/1986/14/contents

239.   Fiji: an open-source platform for biological-image analysis | Nature Methods [Internet]. [cited 2022 Jan 30]. Available from: https://www.nature.com/articles/nmeth.2019

240.   Kim JH, Jang MJ, Choi J, Lee E, Song K, Cho J, et al. Optimizing tissue-clearing conditions based on analysis of the critical factors affecting tissue-clearing procedures. Sci Rep. 2018 Dec;8(1):12815.

241.   Shaner 2005 Nature Methods - Choosing fluorescent proteins.pdf [Internet]. [cited 2022 Feb 23]. Available from: http://www.tsienlab.ucsd.edu/Publications/Shaner%202005%20Nature%20Methods%20-%20Choosing%20fluorescent%20proteins.pdf

242.   Kremers GJ, Gilbert SG, Cranfill PJ, Davidson MW, Piston DW. Fluorescent proteins at a glance. Journal of Cell Science. 2011 Jan 15;124(2):157–60.

243.   Ertürk A, Becker K, Jährling N, Mauch CP, Hojer CD, Egen JG, et al. Three-dimensional imaging of solvent-cleared organs using 3DISCO. Nat Protoc. 2012 Nov;7(11):1983–95.

244.   Glaser AK, Reder NP, Chen Y, Yin C, Wei L, Kang S, et al. Multi-immersion open-top light-sheet microscope for high-throughput imaging of cleared tissues. Nat Commun. 2019 Jul 4;10(1):2781.

245.	Olianti C, Giardini F, Lazzeri E, Costantini I, Silvestri L, Coppini R, et al. Optical clearing in cardiac imaging: A comparative study. Progress in Biophysics and Molecular Biology. 2022 Jan 1;168:10–7.

246.	Li Y, Xu J, Wan P, Yu T, Zhu D. Optimization of GFP Fluorescence Preservation by a Modified uDISCO Clearing Protocol. Front Neuroanat. 2018;12:67.

247.	Lai HM, Liu AKL, Ng HHM, Goldfinger MH, Chau TW, DeFelice J, et al. Next generation histology methods for three-dimensional imaging of fresh and archival human brain tissues. Nat Commun. 2018 Mar 14;9(1):1066.

248.	Zhu J, Yu T, Li Y, Xu J, Qi Y, Yao Y, et al. MACS: Rapid Aqueous Clearing System for 3D Mapping of Intact Organs. Advanced Science. 2020;7(8):1903185.

249.	Sharma A, Jaganathan BG. Stem Cell Therapy for Retinal Degeneration: The Evidence to Date. Biologics. 2021;15:299–306.

250.	Yun CW, Lee SH. Potential and Therapeutic Efficacy of Cell-based Therapy Using Mesenchymal Stem Cells for Acute/chronic Kidney Disease. Int J Mol Sci. 2019 Apr 1;20(7):E1619.

251.	Richardson SM, Kalamegam G, Pushparaj PN, Matta C, Memic A, Khademhosseini A, et al. Mesenchymal stem cells in regenerative medicine: Focus on articular cartilage and intervertebral disc regeneration. Methods. 2016 Apr 15;99:69–80.

252.	Eom YW, Yoon Y, Baik SK. Mesenchymal stem cell therapy for liver disease: current status and future perspectives. Curr Opin Gastroenterol. 2021 May 1;37(3):216–23.

253.	Iwasaki H, Akashi K. Myeloid lineage commitment from the hematopoietic stem cell. Immunity. 2007 Jun;26(6):726–40.

254.	H K, N M. Myeloid cells. The international journal of biochemistry & cell biology [Internet]. 2004 Aug [cited 2022 Jun 16];36(8). Available from: https://pubmed.ncbi.nlm.nih.gov/15147715/

255.   Prame Kumar K, Nicholls AJ, Wong CHY. Partners in crime: neutrophils and monocytes/macrophages in inflammation and disease. Cell Tissue Res. 2018 Mar;371(3):551–65.

256.   Joel MDM, Yuan J, Wang J, Yan Y, Qian H, Zhang X, et al. MSC: immunoregulatory effects, roles on neutrophils and evolving clinical potentials. Am J Transl Res. 2019 Jun 15;11(6):3890–904.

257.   Patel AA, Ginhoux F, Yona S. Monocytes, macrophages, dendritic cells and neutrophils: an update on lifespan kinetics in health and disease. Immunology. 2021 Jul;163(3):250–61.

258.   Papayannopoulos V. Neutrophil extracellular traps in immunity and disease. Nat Rev Immunol. 2018 Feb;18(2):134–47.

259.   Hall SRR, Tsoyi K, Ith B, Padera RF, Lederer JA, Wang Z, et al. Mesenchymal stromal cells improve survival during sepsis in the absence of heme oxygenase-1: the importance of neutrophils. Stem Cells. 2013 Feb;31(2):397–407.

260.   Yona S, Jung S. Monocytes: subsets, origins, fates and functions. Curr Opin Hematol. 2010 Jan;17(1):53–9.

261.   Arora S, Dev K, Agarwal B, Das P, Syed MA. Macrophages: Their role, activation and polarization in pulmonary diseases. Immunobiology. 2018 May;223(4–5):383–96.

262.   Hoogduijn MJ, Roemeling-van Rhijn M, Engela AU, Korevaar SS, Mensah FKF, Franquesa M, et al. Mesenchymal stem cells induce an inflammatory response after intravenous infusion. Stem Cells Dev. 2013 Nov 1;22(21):2825–35.

263.   Nakajima H, Uchida K, Guerrero AR, Watanabe S, Sugita D, Takeura N, et al. Transplantation of mesenchymal stem cells promotes an alternative pathway of macrophage activation and functional recovery after spinal cord injury. J Neurotrauma. 2012 May 20;29(8):1614–25.

264. Zheng G, Ge M, Qiu G, Shu Q, Xu J. Mesenchymal Stromal Cells Affect Disease Outcomes via Macrophage Polarization. Stem Cells Int. 2015;2015:989473.

265. Joshi N, Walter JM, Misharin AV. Alveolar Macrophages. Cellular Immunology. 2018 Aug 1;330:86–90.

266. Krasnodembskaya A, Morrison T, O'Kane C, McAuley D, Matthay M. Human mesenchymal stem cells (MSC) modulate alveolar macrophage polarization in vivo and in vitro. European Respiratory Journal. 44(Suppl 58).

267. Bedoret D, Wallemacq H, Marichal T, Desmet C, Quesada Calvo F, Henry E, et al. Lung interstitial macrophages alter dendritic cell functions to prevent airway allergy in mice. J Clin Invest. 2009 Dec;119(12):3723–38.

268. Gibbings SL, Thomas SM, Atif SM, McCubbrey AL, Desch AN, Danhorn T, et al. Three Unique Interstitial Macrophages in the Murine Lung at Steady State. Am J Respir Cell Mol Biol. 2017 Jul;57(1):66–76.

269. Schyns J, Bureau F, Marichal T. Lung Interstitial Macrophages: Past, Present, and Future. J Immunol Res. 2018 Apr 30;2018:5160794.

270. Leibacher J, Dauber K, Ehser S, Brixner V, Kollar K, Vogel A, et al. Human mesenchymal stromal cells undergo apoptosis and fragmentation after intravenous application in immune-competent mice. Cytotherapy. 2017 Jan;19(1):61–74.

271. Eggenhofer E, Steinmann JF, Renner P, Slowik P, Piso P, Geissler EK, et al. Mesenchymal stem cells together with mycophenolate mofetil inhibit antigen presenting cell and T cell infiltration into allogeneic heart grafts. Transpl Immunol. 2011 Apr 15;24(3):157–63.

272. Misharin AV, Morales-Nebreda L, Mutlu GM, Budinger GRS, Perlman H. Flow cytometric analysis of macrophages and dendritic cell subsets in the mouse lung. Am J Respir Cell Mol Biol. 2013 Oct;49(4):503–10.

273. Liegeois M, Legrand C, Desmet CJ, Marichal T, Bureau F. The interstitial macrophage: A long-neglected piece in the puzzle of lung immunity. Cellular Immunology. 2018 Aug 1;330:91–6.

274.	Akinrinmade OA, Chetty S, Daramola AK, Islam M ul, Thepen T, Barth S. CD64: An Attractive Immunotherapeutic Target for M1-type Macrophage Mediated Chronic Inflammatory Diseases. Biomedicines. 2017 Sep 12;5(3):56.

275.	Allden SJ, Toshner RJ, Byrne AJ, Lloyd CM, Maher T. Expression of CD71 on Alveolar Macrophages Reveals Distinct Cell Populations in Human Bronchoalveolar Lavage from Patients with Interstitial Lung Disease. In: D27 Macrophages: Resolvers, responders, or both? American Thoracic Society; 2016. p. A6605–A6605. (American Thoracic Society International Conference Abstracts).

276.	Allden SJ, Ogger PP, Ghai P, McErlean P, Hewitt R, Toshner R, et al. The Transferrin Receptor CD71 Delineates Functionally Distinct Airway Macrophage Subsets during Idiopathic Pulmonary Fibrosis. Am J Respir Crit Care Med. 2019 Jul 15;200(2):209–19.

277.	Zhang QQ, Hu XW, Liu YL, Ye ZJ, Gui YH, Zhou DL, et al. CD11b deficiency suppresses intestinal tumor growth by reducing myeloid cell recruitment. Sci Rep. 2015 Nov 3;5:15948.

278.	Reeba A. Omman, Ameet R. Kini. Acute leukemias [Internet]. [cited 2022 Jun 16]. Available from: https://reader.elsevier.com/reader/sd/pii/B9780323530453000404?token=0F 20FFE9FE82A4F4D3810DAD5AD75CE750FEA8ADA19F0B28758389791E 5CA153E202555CCCAD469876CC3FCF032F3A33&originRegion=eu-west-1&originCreation=20220616143702

279.	Aratani Y. Myeloperoxidase: Its role for host defense, inflammation, and neutrophil function. Arch Biochem Biophys. 2018 Feb 15;640:47–52.

280.	Bucher K, Schmitt F, Autenrieth SE, Dillmann I, Nürnberg B, Schenke-Layland K, et al. Fluorescent Ly6G antibodies determine macrophage phagocytosis of neutrophils and alter the retrieval of neutrophils in mice. J Leukoc Biol. 2015 Sep;98(3):365–72.

281.	Morales-Primo AU, Becker I, Zamora-Chimal J. Neutrophil extracellular trap-associated molecules: a review on their immunophysiological and

inflammatory roles. International Reviews of Immunology. 2022 Mar 4;41(2):253–74.

282. Milich LM, Ryan CB, Lee JK. The Origin, Fate, and Contribution of Macrophages to Spinal Cord Injury Pathology. Acta Neuropathol. 2019 May;137(5):785–97.

283. Zaynagetdinov R, Sherrill TP, Kendall PL, Segal BH, Weller KP, Tighe RM, et al. Identification of myeloid cell subsets in murine lungs using flow cytometry. Am J Respir Cell Mol Biol. 2013 Aug;49(2):180–9.

284. de Witte SFH, Merino AM, Franquesa M, Strini T, van Zoggel JAA, Korevaar SS, et al. Cytokine treatment optimises the immunotherapeutic effects of umbilical cord-derived MSC for treatment of inflammatory liver disease. Stem Cell Res Ther. 2017 Jun 8;8(1):140.

285. Silva LHA, Antunes MA, Dos Santos CC, Weiss DJ, Cruz FF, Rocco PRM. Strategies to improve the therapeutic effects of mesenchymal stromal cells in respiratory diseases. Stem Cell Res Ther. 2018 Feb 26;9:45.

286. Sart S, Ma T, Li Y. Preconditioning stem cells for in vivo delivery. Biores Open Access. 2014 Aug 1;3(4):137–49.

287. De Becker A, Riet IV. Homing and migration of mesenchymal stromal cells: How to improve the efficacy of cell therapy? World J Stem Cells. 2016 Mar 26;8(3):73–87.

288. Németh K, Leelahavanichkul A, Yuen PST, Mayer B, Parmelee A, Doi K, et al. Bone marrow stromal cells attenuate sepsis via prostaglandin E(2)-dependent reprogramming of host macrophages to increase their interleukin-10 production. Nat Med. 2009 Jan;15(1):42–9.

289. Teo GSL, Yang Z, Carman CV, Karp JM, Lin CP. Intravital Imaging of Mesenchymal Stem Cell Trafficking and Association With Platelets and Neutrophils. Stem Cells. 2015 Jan 1;33(1):265–77.

290. Li N, Hua J. Interactions between mesenchymal stem cells and the immune system. Cell Mol Life Sci. 2017 Jul;74(13):2345–60.

291. Jennings JH, Linderman DJ, Hu B, Sonstein J, Curtis JL. Monocytes Recruited to the Lungs of Mice during Immune Inflammation Ingest Apoptotic Cells Poorly. Am J Respir Cell Mol Biol. 2005 Feb;32(2):108–17.

292. Xia Z, Ye H, Choong C, Ferguson DJP, Platt N, Cui Z, et al. Macrophagic response to human mesenchymal stem cell and poly(epsilon-caprolactone) implantation in nonobese diabetic/severe combined immunodeficient mice. J Biomed Mater Res A. 2004 Dec 1;71(3):538–48.

293. Moll G, Jitschin R, von Bahr L, Rasmusson-Duprez I, Sundberg B, Lönnies L, et al. Mesenchymal stromal cells engage complement and complement receptor bearing innate effector cells to modulate immune responses. PLoS One. 2011;6(7):e21703.

294. Moll G, Ankrum JA, Kamhieh-Milz J, Bieback K, Ringdén O, Volk HD, et al. Intravascular Mesenchymal Stromal/Stem Cell Therapy Product Diversification: Time for New Clinical Guidelines. Trends in Molecular Medicine. 2019 Feb 1;25(2):149–63.

295. Soria-Juan B, Escacena N, Capilla-González V, Aguilera Y, Llanos L, Tejedo JR, et al. Cost-Effective, Safe, and Personalized Cell Therapy for Critical Limb Ischemia in Type 2 Diabetes Mellitus. Frontiers in Immunology [Internet]. 2019 [cited 2022 Jul 1];10. Available from: https://www.frontiersin.org/article/10.3389/fimmu.2019.01151

296. Zhang QZ, Su WR, Shi SH, Wilder-Smith P, Xiang AP, Wong A, et al. Human Gingiva-Derived Mesenchymal Stem Cells Elicit Polarization of M2 Macrophages and Enhance Cutaneous Wound Healing. Stem Cells. 2010 Oct;28(10):1856–68.

297. Silva M, Correia-Neves M. Neutrophils and Macrophages: the Main Partners of Phagocyte Cell Systems. Frontiers in Immunology. 2012;3.

298. Silva MT. Neutrophils and macrophages work in concert as inducers and effectors of adaptive immunity against extracellular and intracellular microbial pathogens. J Leukoc Biol. 2010 May;87(5):805–13.

299. Melief SM, Schrama E, Brugman MH, Tiemessen MM, Hoogduijn MJ, Fibbe WE, et al. Multipotent stromal cells induce human regulatory T cells

through a novel pathway involving skewing of monocytes toward anti-inflammatory macrophages. Stem Cells. 2013 Sep;31(9):1980–91.

300. Rasmusson I, Ringdén O, Sundberg B, Le Blanc K. Mesenchymal stem cells inhibit lymphocyte proliferation by mitogens and alloantigens by different mechanisms. Experimental Cell Research. 2005 Apr 15;305(1):33–41.

301. Planat-Benard V, Varin A, Casteilla L. MSCs and Inflammatory Cells Crosstalk in Regenerative Medicine: Concerted Actions for Optimized Resolution Driven by Energy Metabolism. Front Immunol. 2021 Apr 30;12:626755.

302. Zappia E, Casazza S, Pedemonte E, Benvenuto F, Bonanni I, Gerdoni E, et al. Mesenchymal stem cells ameliorate experimental autoimmune encephalomyelitis inducing T-cell anergy. Blood. 2005 Sep 1;106(5):1755–61.

303. Bruno S, Deregibus MC, Camussi G. The secretome of mesenchymal stromal cells: Role of extracellular vesicles in immunomodulation. Immunol Lett. 2015 Dec;168(2):154–8.

304. Vizoso FJ, Eiro N, Cid S, Schneider J, Perez-Fernandez R. Mesenchymal Stem Cell Secretome: Toward Cell-Free Therapeutic Strategies in Regenerative Medicine. Int J Mol Sci. 2017 Aug 25;18(9):1852.

305. Luk F, de Witte SFH, Korevaar SS, Roemeling-van Rhijn M, Franquesa M, Strini T, et al. Inactivated Mesenchymal Stem Cells Maintain Immunomodulatory Capacity. Stem Cells Dev. 2016 Sep 15;25(18):1342–54.

306. Weiss ARR, Lee O, Eggenhofer E, Geissler E, Korevaar SS, Soeder Y, et al. Differential effects of heat-inactivated, secretome-deficient MSC and metabolically active MSC in sepsis and allogenic heart transplantation. Stem Cells. 2020 Jun;38(6):797–807.

307. Song X, Xie S, Lu K, Wang C. Mesenchymal stem cells alleviate experimental asthma by inducing polarization of alveolar macrophages. Inflammation. 2015 Apr;38(2):485–92.

308.   Mathias LJ, Khong SML, Spyroglou L, Payne NL, Siatskas C, Thorburn AN, et al. Alveolar macrophages are critical for the inhibition of allergic asthma by mesenchymal stromal cells. J Immunol. 2013 Dec 15;191(12):5914–24.

309.   Peters-Golden M. The alveolar macrophage: the forgotten cell in asthma. Am J Respir Cell Mol Biol. 2004 Jul;31(1):3–7.

310.   Abreu SC, Rolandsson Enes S, Dearborn J, Goodwin M, Coffey A, Borg ZD, et al. Lung inflammatory environments differentially alter mesenchymal stromal cell behavior. Am J Physiol Lung Cell Mol Physiol. 2019 Dec 1;317(6):L823–31.

311.   Kean TJ, Lin P, Caplan AI, Dennis JE. MSCs: Delivery Routes and Engraftment, Cell-Targeting Strategies, and Immune Modulation. Stem Cells International. 2013 Aug 13;2013:e732742.

312.   In Vivo Micro-Computerized Tomography Tracking of Human Periodontal Ligament Stem Cells Labeled with Gold Nanocomplexes. [cited 2022 Jan 15]; Available from: https://onlinelibrary.wiley.com/doi/10.1002/adhm.202101133

313.   van Mastrigt E, Logie K, Ciet P, Reiss IKM, Duijts L, Pijnenburg MW, et al. Lung CT imaging in patients with bronchopulmonary dysplasia: A systematic review. Pediatr Pulmonol. 2016 Sep;51(9):975–86.

314.   Meir R, Betzer O, Motiei M, Kronfeld N, Brodie C, Popovtzer R. Design principles for noninvasive, longitudinal and quantitative cell tracking with nanoparticle-based CT imaging. Nanomedicine. 2017 Feb;13(2):421–9.

315.   Betzer O, Meir R, Motiei M, Yadid G, Popovtzer R. Gold nanoparticle-cell labeling methodology for tracking stem cells within the brain. In: Nanoscale Imaging, Sensing, and Actuation for Biomedical Applications XIV. SPIE; 2017. p. 189–97.

316.   Meir R, Betzer O, Barnoy E, Motiei M, Popovtzer R. Gold nanoparticles for non-invasive cell tracking with CT imaging. In: Nanoscale Imaging, Sensing, and Actuation for Biomedical Applications XV. SPIE; 2018. p. 155–63.

317.   Betzer O, Shwartz A, Motiei M, Kazimirsky G, Gispan I, Damti E, et al. Nanoparticle-based CT imaging technique for longitudinal and quantitative stem cell tracking within the brain: application in neuropsychiatric disorders. ACS Nano. 2014 Sep 23;8(9):9274–85.

318.   Shilo M, Reuveni T, Motiei M, Popovtzer R. Nanoparticles as computed tomography contrast agents: current status and future perspectives. Nanomedicine (Lond). 2012 Feb;7(2):257–69.

319.   Shwartz A, Betzer O, Kronfeld N, Kazimirsky G, Cazacu S, Finniss S, et al. Therapeutic Effect of Astroglia-like Mesenchymal Stem Cells Expressing Glutamate Transporter in a Genetic Rat Model of Depression. Theranostics. 2017;7(10):2690–703.

320.   Bouché M, Hsu JC, Dong YC, Kim J, Taing K, Cormode DP. Recent Advances in Molecular Imaging with Gold Nanoparticles. Bioconjug Chem. 2020 Feb 19;31(2):303–14.

321.   Kumar S, Liney G, Rai R, Holloway L, Moses D, Vinod SK. Magnetic resonance imaging in lung: a review of its potential for radiotherapy. Br J Radiol. 2016 Apr;89(1060):20150431.

322.   Liu Q, Feng Z, Liu WV, Fu W, He L, Cheng X, et al. Assessment of Solid Pulmonary Nodules or Masses Using Zero Echo Time MR Lung Imaging: A Prospective Head-to-Head Comparison With CT. Frontiers in Oncology [Internet]. 2022 [cited 2022 Oct 24];12. Available from: https://www.frontiersin.org/articles/10.3389/fonc.2022.812014

323.   Jt R, X Y, S G, T M. Tracking mesenchymal stem cells using magnetic resonance imaging. Brain circulation [Internet]. 2016 Sep [cited 2022 Oct 24];2(3). Available from: https://pubmed.ncbi.nlm.nih.gov/30276283/

324.   Sehl OC, Gevaert JJ, Melo KP, Knier NN, Foster PJ. A Perspective on Cell Tracking with Magnetic Particle Imaging. Tomography. 2020 Dec;6(4):315–24.

325.   Zheng B, von See MP, Yu E, Gunel B, Lu K, Vazin T, et al. Quantitative Magnetic Particle Imaging Monitors the Transplantation, Biodistribution, and Clearance of Stem Cells In Vivo. Theranostics. 2016 Jan 1;6(3):291–301.

326. Booth MJ, Wilson T. Refractive-index-mismatch induced aberrations in single-photon and two-photon microscopy and the use of aberration correction. J Biomed Opt. 2001 Jul;6(3):266–72.

327. Breslin WL, Strohacker K, Carpenter KC, Haviland DL, McFarlin BK. Mouse blood monocytes: Standardizing their identification and analysis using CD115. Journal of Immunological Methods. 2013 Apr 30;390(1):1–8.

328. Chávez-Galán L, Olleros ML, Vesin D, Garcia I. Much More than M1 and M2 Macrophages, There are also CD169+ and TCR+ Macrophages. Frontiers in Immunology. 2015;6.

Appendix: Supporting manuscripts

New Results

🔔 Follow this preprint

Computed tomography lacks sensitivity to image gold labelled mesenchymal stromal cells in vivo as evidenced by multispectral optoacoustic tomography

Alejandra Hernandez Pichardo, James Littlewood, Arthur Taylor, Bettina Wilm, Raphaël Lévy, Patricia Murray

This article is a preprint and has not been certified by peer review [what does this mean?].

💬 0 | ☑ 0 | 👥 0 | ⚙ 0 | 🖵 0 | 🎬 0 | 🐦 7

| **Abstract** | Full Text | Info/History | Metrics | | 🗋 Preview PDF |

Abstract

Elucidating the mechanisms of action and long-term safety of cell therapies is necessary for their clinical translation. Non-invasive imaging technologies such as bioluminescence imaging (BLI), computed tomography (CT) and multispectral optoacoustic tomography (MSOT) have been proposed as tools for longitudinal cell monitoring but their performances have not been compared. Here, we evaluate combinations of these modalities to track the in vivo distribution of gold-labelled mesenchymal stromal cells (MSCs). We found that injected MSCs labelled with gold nanoparticles and expressing the reporter gene firefly luciferase could be detected with BLI and MSOT but not CT. We conclude that the MSCs did not carry enough contrast agent to be tracked by CT, demonstrating that CT tracking of gold-labelled cells is not a practical approach as high amounts of gold, which might impair cell viability, are necessary.

Competing Interest Statement

James Littlewood works at iThera Medical GmBh.

New Results

Comparison between optical tissue clearing methods for detecting administered mesenchymal stromal cells in mouse lungs

Alejandra Hernandez Pichardo, Francesco Amadeo, Bettina Wilm, Raphaël Lévy, Lorenzo Ressel, Patricia Murray, Violaine Sée

doi: https://doi.org/10.1101/2022.07.23.501233

This article is a preprint and has not been certified by peer review [what does this mean?].

💬 0 | ☑ 0 | 👥 0 | 🎛 0 | 🖥 0 | ▦ 0 | 🐦 8

Abstract   Full Text   Info/History   Metrics   📄 Preview PDF

Abstract

Optical tissue clearing of lung tissue enables the intact lung to be imaged using fluorescence microscopy. Several clearing protocols have been developed in recent years, including the Clear, Unobstructed Brain/Body Imaging Cocktails and Computational analysis (CUBIC), stabilised 3D imaging of solvent-cleared organs (s-DISCO) and Ethyl cinnamate (ECi) methods. Here we compared these protocols with the aim of determining the biodistribution of mesenchymal stroma cells (MSCs) and understanding how they interact with host cells in the mouse lung. First, we evaluated how each method affected the size, morphology, and transparency of the lungs. Then, we compared the preservation of the fluorescence of the protein tdTomato expressed by the MSCs, and of the organic dye Evans Blue which labels the vasculature. In addition, we tested the compatibility of the methods with immunofluorescence staining. We found that CUBIC clearing is the only method that enables direct imaging of fluorescently labelled MSCs in the lungs thereby allowing the study of the MSC interaction with endothelial and immune cells when combined with immunofluorescence staining. Overall, 3D imaging of CUBIC cleared lungs confirmed that injected MSCs are initially retained in the pulmonary microvasculature, and that most cells are eliminated from the lungs within the first 24 h.

Summary statement We present a tissue clearing approach to visualize exogenous MSCs in the mouse lung and study their effects in the host.

Intravenous administration of human umbilical cord mesenchymal stromal cells leads to an inflammatory response in the lung

Alejandra Hernandez Pichardo, Bettina Wilm, Neill Liptrott, Patricia Murray

**Abstract**   Info/History   Metrics   🗋 Preview PDF

Abstract

Mesenchymal stromal cells (MSCs) administered intravenously (IV) have shown efficacy in pre-clinical models of various diseases. This is despite the cells not reaching the site of injury due to entrapment in the lungs. The ability of MSCs to modulate immune responses has been proposed as one of the mechanisms by which these cells provide therapeutic benefits, irrespective of whether they are sourced from bone marrow, adipose tissue or umbilical cord. To better understand how MSCs affect innate immune cell populations in the lung, we evaluated the percentage, distribution and phenotype of neutrophils, monocytes and macrophages by flow cytometry and histological analyses after delivering human umbilical cord-derived MSCs (hUC-MSCs) IV into immunocompetent mice. After 2 h, we observed a sharp increase in neutrophils, and pro-inflammatory monocytes and macrophages. Moreover, these immune cells localised in the vicinity of the MSCs suggesting an active role in their clearance. By 24 h, we detected an increase in anti-inflammatory monocytes and macrophages. These results suggest that the IV injection of hUC-MSCs leads to an initial inflammatory phase in the lung shortly after injection, followed by a resolution phase 24 h later.
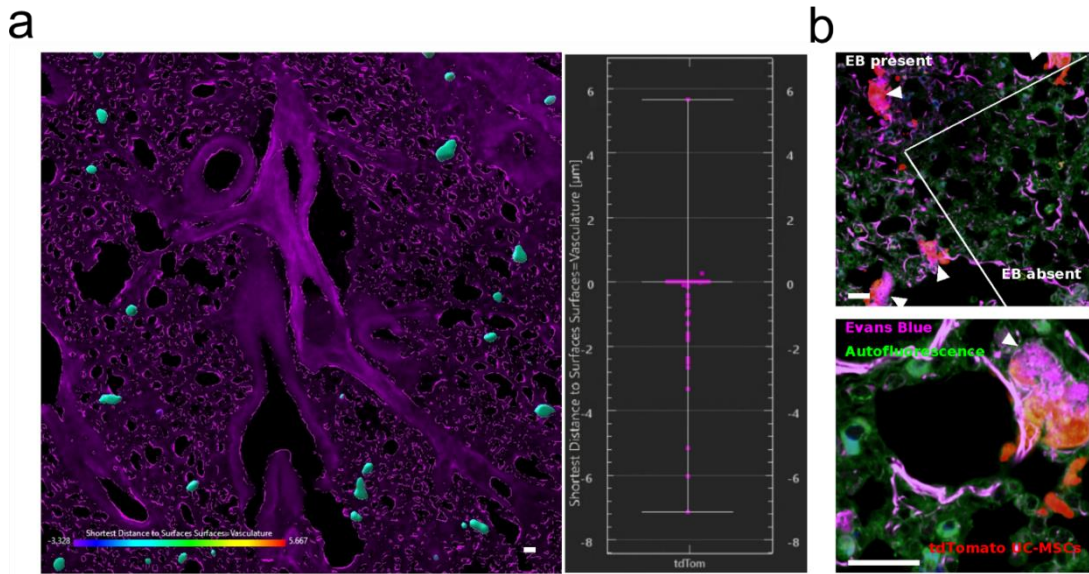
Supplementary information
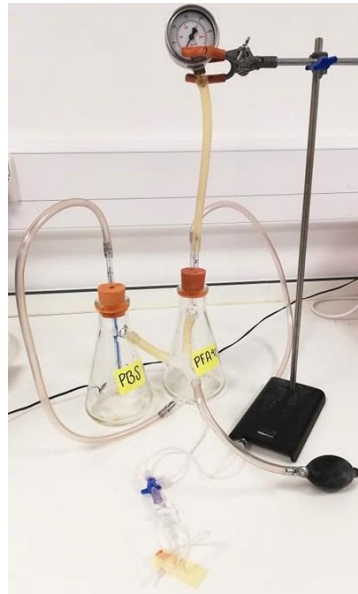
Supplementary figure 1. Perfusion pump. Two Erlenmeyer flasks, filled with either PBS or 4% PFA, are joined through tubes connected to their sidearms, which are connected to a manual bulb that helps pressurize the system. A pressure gauge is connected to one of the bottles to monitor and maintain pressure. Pipettes extend through rubber stoppers and down into the fluid in each flask. The pressure flowing through the sidearm pumps the liquid from each bottle into these pipettes and out of the flasks, where a stopcock allows fluid to flow from one flask at a time.
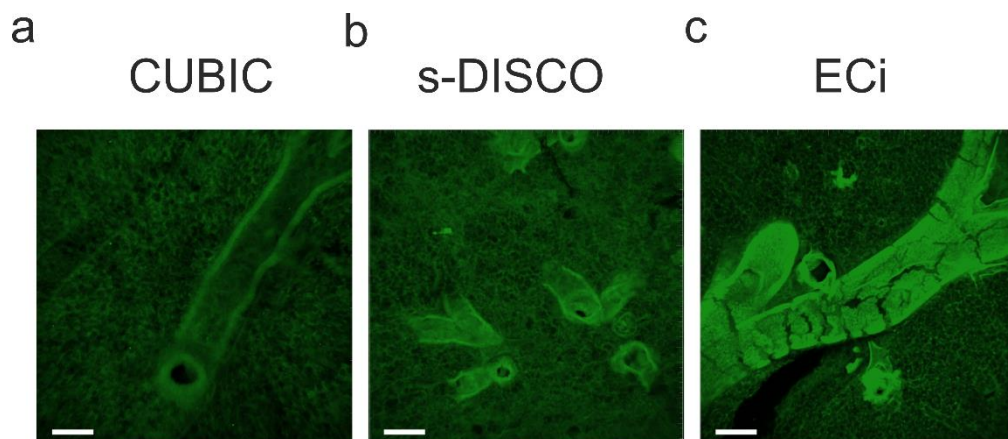

Supplementary figure 2. Lung morphology after optical tissue clearing. a) CUBIC cleared lung. b) s-DISCO cleared lung. c) ECi cleared lung. Scale bar = 150 μm. MIPs before image reconstruction were obtained by confocal imaging on a Leica DMi8 with Andor Dragonfly spinning disk, coupled to an EMCCD camera using a 10x/0.45 air objective. Z-stacks were captured using the 488 nm laser line and 525/50 emission filter.
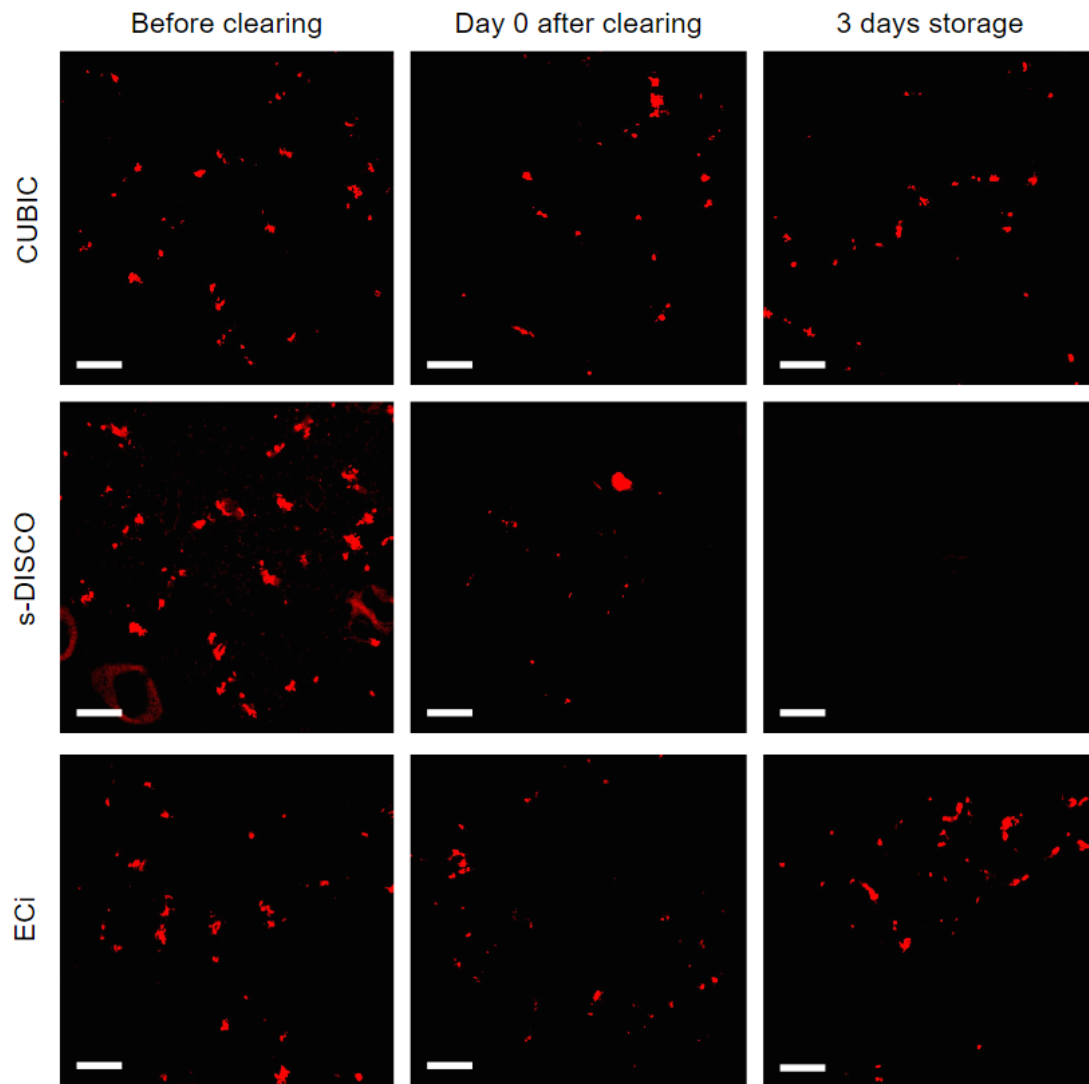
Supplementary figure 3. Fluorescence preservation of tdTomato (red) after clearing 100 μm thick lung sections. Impact of CUBIC, s-DISCO and ECi clearing on the fluorescence of tdTomato before, immediately after, and 3 days after of storage in RI solution. Images were acquired by confocal microscopy using a 10x/0.45 air objective. Z-stacks were captured using the 561 nm laser line and 600/50 nm emission filter.

Supplementary figure 4. Evans blue vascular staining. a) Lung 30 µm cryosections. IMARIS 3D reconstruction and shortest distance calculation analysis. Distance analysis performed between the tdTomato UC-MSCs (cyan) and the vasculature (magenta). n = 9. b) tdTomato UC-MSCs obstructing EB flow through vasculature. Arrowheads indicate areas of EB accumulation. Scale bar 25 µm.
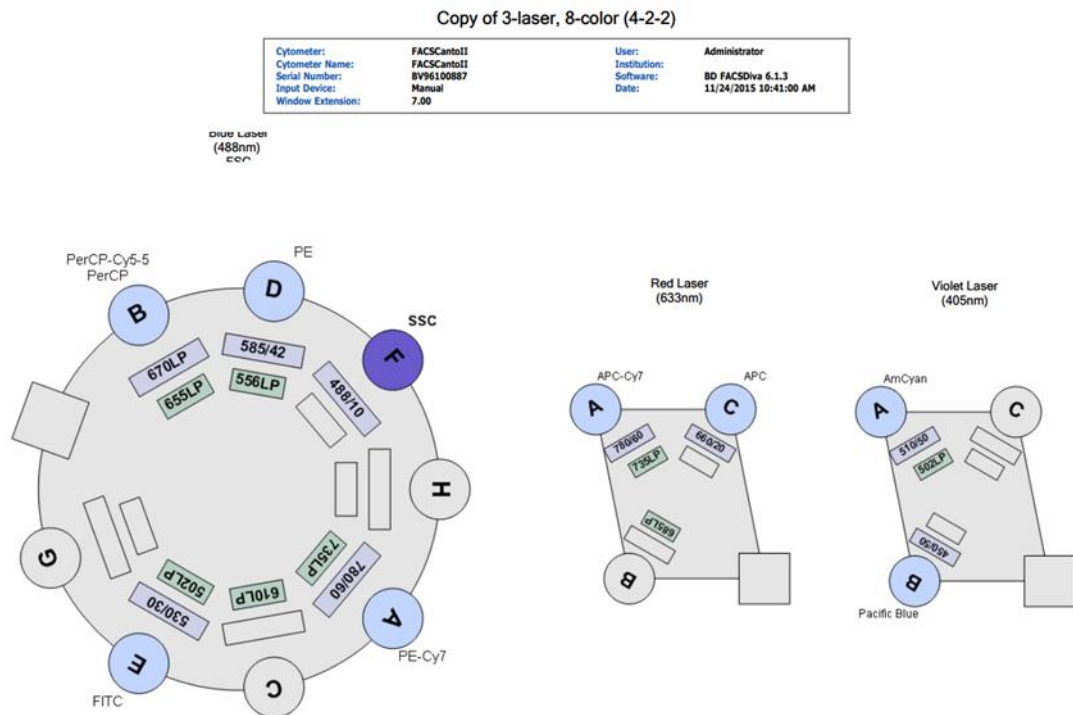
Supplementary Figure 5. CANTO II configuration.

Supplementary methods

Solvent based optical tissue clearing of 100 μm lung sections.

Supplementary table 1. Solvent based optical tissue clearing of 100 μm lung sections.

	100 μm sections	
	s-DISCO	ECi
1-propanol 50%	3 min	3 min
1-propanol 80%	3 min	3 min
1-propanol 100%	3 x 3 min	3 x 3 min
DCM	1 min	-
DBE w/ 0.4% propyl gallate	storage	-
ECi	-	storage

Supplementary movies

Supplementary Movie 1. CUBIC lung vasculature. CD34 stained endothelium (white) of lungs collected 2 h after receiving tdTomato hUC-MSCs (red). Tissue autofluorescence (green).

CUBIC lung vasculature 2h after IV hUCMSCs.mp4

Supplementary movie 2. CUBIC lung vasculature. CD34 stained endothelium (white) of lungs collected 24 h after receiving tdTomato hUC-MSCs (red). Tissue autofluorescence (green).

CUBIC lung vasculature 24h after IV hUCMSCs.mp4